Jonas Rudshaug

Modeling of glass exposed to extreme loadings

NTNU
Norwegian University of
Science and Technology

Jonas Rudshaug

Modeling of glass exposed to extreme loadings

Thesis for the Degree of Philosophiae Doctor

Trondheim, November 2023

Norwegian University of Science and Technology
Faculty of Engineering
Department of Structural Engineering

NTNU

Norwegian University of
Science and Technology

Preface

This thesis is submitted in partial fulfilment of the degree *Philosophiae Doctor* (PhD) at the Norwegian University of Science and Technology (NTNU). The presented research was carried out at the Structural Impact Laboratory (SIMLab) at the NTNU in the Department of Structural Engineering. The work started in August 2019, and my main supervisor has been Professor Tore Børvik with Professor Odd Sture Hopperstad as co-supervisor.

The work was a part of the Protective Structures group lead by Professor Tore Børvik at the Centre for Advanced Structural Analysis (CASA), Centre for Research-based Innovation (CRI) established by the Research Council of Norway. The funding for the work was provided by CASA and the Faculty of Engineering at NTNU.

Acknowledgements

Looking back at the last four years, I feel privileged and proud. I have been given space, time and support to learn and to walk my own path, forming the PhD in my own way. I have been encouraged to take responsibility, to fail, and to learn from my mistakes. I have been trusted to represent the group, on partner visits, on international conferences, and on partner seminars. Most importantly, I have been surrounded by a fantastic group of colleagues. All these factors have been invaluable to me.

I want to express gratitude to my fantastic supervisors Professor Tore Børvik and Professor Odd Sture Hopperstad. You have patiently listened to all my ideas and jokes, and corrected my funny typos, while providing world-class guidance. I have really enjoyed our conversations, thank you. I want to thank Dr. Torodd Berstad for remarkable assistance and guidance through the LS-DYNA user interface jungle. I have enjoyed our discussions and I am deeply impressed by your endless knowledge.

For providing me with a great starting point and for being a great conversation partner, I want to acknowledge Dr. Karoline Osnes Aasen. I am grateful to BMW for the interest in my work and for providing all the windshields I have tested. The effort made by Dr. Sebastian Kreissl and Dr. Jonas D'Haen has been appreciated. My gratitude also goes to Mr. Trond Auestad and Mr. Tore Wisth for great assistance during my experimental campaigns, also to Mr. Einer Herrem, Mr. Jørgen Rødal Høstmark and Mr. Knut Sørenes Kloster for the assistance in the lab.

These four years would not have been the same without my great colleagues at SIMLab. I have really enjoyed our many discussions. Unfortunately, there are too many of you for me to mention you all by name, but you know who you are. A special thanks goes to Ruben Løland Sælen for always participating passionately in discussions regardless of the topic, and to Sigurd Aune for enduring my many rapid comments and providing well considered responses. In addition, I want to thank the great people at the Norwegian Defence Estate Agency and Multiconsult for welcoming me and providing me with an office space for the final year of the PhD.

A huge thanks goes to my family, for providing constant support and encouragement through my long stay in Trondheim. Finally, my deepest gratitude goes to my partner, Stine, for always finding a way to make me smile.

Summary

The interest in the load bearing capacity of glass is gradually increasing as a consequence of increased demand for transparency in buildings and vehicles and more strict safety requirements. Due to the stochastic and violent behavior of glass fracture, experimental studies on glass require many repetitions, drastically increasing the experimental cost and environmental impact. For this reason, there is a need for accurate numerical tools that can incorporate the stochastic and violent nature of glass fracture.

With that in mind, this thesis aims to increase the understanding of the mechanical behavior of glass through experimental studies and development of numerical models. The work includes an experimental study on three types of windshields using a new experimental setup that facilitates detailed extraction of important data, such as loading and deformation histories and crack propagation data. The acquired experimental database from the windshield tests was used to verify the performance of the Glass Strength Prediction Model (GSPM) for complex geometries. Furthermore, the GSPM was improved to account for sub-critical crack growth (SCG) and implemented into the commercial finite element (FE) code LS-DYNA, where it works as a fracture initiation trigger for the existing glass material model MAT_280. In relation to the crack propagation behavior of glass, an experimental setup for quasi-statically loaded L-shaped glass specimen was developed to document the crack propagation behavior in terms of propagation path and speed as well as load level. A phase-field approach to fracture was implemented into shell and solid user elements in LS-DYNA with a new crack driving force to simulate the experimental behavior. Furthermore, in collaboration with the Department of Physics at NTNU, a method for characterizing the glass surface flaws using Fourier ptychographic microscopy (FPM) is developed.

The experimental study on windshields revealed a stochastic and size-dependent component strength with varying resulting crack patterns. In addition, circumferential cracks were found to have higher average crack speeds than radial cracks. With the introduction of SCG into the GSPM, the model was shown capable of predicting both the rate- and size-dependent behavior of glass fracture. The GSPM predicted accurate fracture initiation locations on windshields close to the experimental results, and it was found that the maximum flaw depth and the depth-to-half-length ratio of the flaw were the most influential input parameters. The experiments on L-shaped glass specimens showed a positive correlation between the initial crack propagation speed and the critical load level. In addition, a correlation between the crack propagation path and the critical load level was found. An exponential decay was observed in the crack propagation speed with time. With the new crack driving force, the implemented fracture phase-field model proved capable of capturing the initial crack propagation speed for the lowest and highest critical load levels seen in the experiments. However, the crack propagation speed dropped too quickly compared to the experiments, potentially leading to deviations from the experiments in the final part of the predicted crack paths.

Overall, this work has pushed the field of glass modeling one step further, with the introduction of a solver integrated version of the GSPM which can trigger other existing fracture models. In this way, the bar is lowered for incorporating the stochastic behavior of glass fracture in modern design processes where FE simulations are involved. Furthermore, the new crack driving force for the phase-field approach to fracture proved it possible to predict the initial crack propagation speeds for varying critical load levels. Hopefully, these findings will inspire new and extended research in the field of glass modeling.

Table of Contents

Abbreviations

3D-DIC 3D-Digital Image Correlation. 13, 15, 17

AE acoustic emission. 13

CAD computer-aided design. 15, 16

CASA Centre for Advanced Structural Analysis. iii

CDF cumulative distribution function. 41

CRI Centre for Research-based Innovation. iii

DGS Digital Gradient Sensing. 64, 65, 76, 103

DIC Digital Image Correlation. 17, 18, 32, 34

FE finite element. vii, viii, 4–6, 15, 28, 37–39, 46, 49, 50, 60, 61, 79, 83, 97–99, 103

FPM Fourier ptychographic microscopy. vii, 103

GSPM Glass Strength Prediction Model. vii, viii, 6, 35, 37–41, 43, 45–48, 50–57, 59–61, 101–103

HIC Head Injury Criterion. 1

LEFM linear elastic fracture mechanics. 4, 37

NTNU Norwegian University of Science and Technology. iii, vii, 6, 17, 69

PDF probability distribution function. 4, 36, 37, 41

PETSc Portable, Extensible Toolkit for Scientific Computation. 83

PMMA Polymethyl methacrylate. 64

PVB polyvinyl butyral. 1, 5, 11, 12, 14, 15, 21, 28, 102

SCG sub-critical crack growth. vii, 4, 6, 35–37, 43–45, 47, 53, 60, 61, 101

SENS single edge notch shear. 87, 88, 97, 98

SENT single edge notch tension. 87, 88, 97, 98

SIMLab Structural Impact Laboratory. iii

SUV sports utility vehicle. 13, 15, 16, 18, 21–24, 31–34, A-1

WHO World Health Organization. 1

XFEM Extended Finite Element Method. 103

1 Introduction

1.1 Background and motivation

We hear about traffic accidents on a daily basis. According to the World Health Organization (WHO) [1], 1.35 million die in traffic accidents annually. Around 26 % of these victims are pedestrians and cyclists. In addition to deaths, road traffic injuries are now the leading cause of death for children and young adults aged 5–29 years. More than half of all road fatalities involve vulnerable road users [2]. In pedestrian-vehicle crashes, moderate injuries usually occur in the lower extremity and head of the pedestrian [3, 4]. If we consider the serious injuries, 80 % of them are head injuries.

If the pedestrian is taller than a certain hight, depending on the shape of the vehicle, it is likely that the head will impact the windshield of the car. Head impact on windshields causes many of the serious head injuries. The severity of the pedestrian head injuries is highly dependent on the mechanical properties of the windshield. Ideally, the windshield should be flexible enough to minimize the head accelerations. To measure the severity of an impact to the head, a Head Injury Criterion (HIC) is used. Depending on the HIC-value, the severity of the head injury is decided. Today, the windshields of new cars are tested and scored using the head injury criterion in standardized tests. To receive a good score, the HIC-values must be below a certain threshold, indicating a less serious head injury.

These strict requirements to the windshield performance increase the need of accurate numerical models capturing the correct windshield behavior. Windshields are a type laminated safety glass that typically consist of two curved glass layers and a polyvinyl butyral (PVB) interlayer. The combination of glass and PVB provides beneficial properties in terms of injury reduction during a crash situation, burglary protection and protection against wind-borne debris. A single glass layer is a weakest link structure, meaning that any crack leads to total failure because the structure does not provide alternative load paths in the event of local failures [5]. Laminated glass, on the other hand, is a fail-safe structure, because the PVB interlayer keeps the glass layers tied together after initial failure of the glass [6]. In the case of windshield fracture, the PVB interlayer will keep the glass fragments together. As the glass layers break, the windshield essentially goes from acting as a laminated composite to a glass-reinforced polymer. The structural behavior of the laminated glass can be subdivided into the following five phases as presented by Larcher et al. [7, 8] in Figure 1.1:

1. Linear, elastic behavior of the glass layers

2. One of the glass layer breaks, while the other layer is still intact

3. The other glass layer fails and the polymer interlayer behaves elastically

4. The interlayer deforms inelastically while keeping the glass fragments together

5. The interlayer fails by either reaching its failure strain or being cut by the broken glass
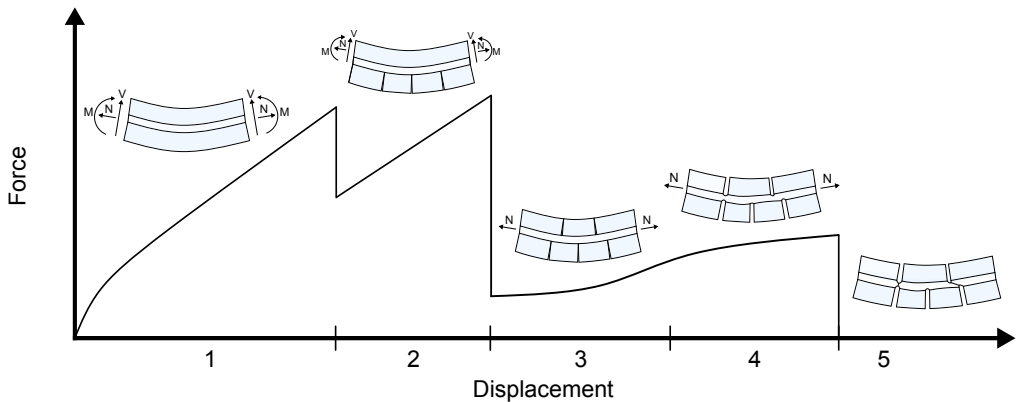

Figure 1.1: The failure phases of laminated glass, adapted from Larcher [8].

Soda-lime-silica float glass, often denoted soda-lime glass, is the most common glass type used for structural purposes [9]. The glass is produced through a float process, where the components presented in Table 1.1 are heated to a temperature of $1500\,°C$, transforming them into a liquid state. Then, the molten glass is carefully poured onto a liquid tin bath, ensuring that the glass solidifies with a uniform thickness in a controlled manner. To relieve internal stresses, the glass temperature is gradually reduced until it solidifies, attaining an amorphous (non-crystalline) state [9].

Table 1.1: The chemical composition of soda-lime-silica glass [9].

Component	Silica sand	Lime	Soda	Magnesia	Alumina	Others
Chemical notation	SiO_2	CaO	Na_2O	MgO	Al_2O_3	—
Mass percentage [%]	69–74	5–14	10–16	0–6	0–3	0–5

To produce curved and laminated safety glass, such as windshields, the glass layers are shaped as a matching group through heating to a temperature of around $620\,°C$ [10]. At this temperature, the curved laminate shape is achieved through either gravity "sagging" or pressbending of the glass layers. The glass layers are cooled to room temperature before they are sandwiched with the polymer interlayer. The bonding of the glass layers to the interlayer is a two-step process [10]:

1. Air trapped in the windshield is removed through a mechanical or vacuum squeezing process

2. The windshield is heated to $140\,°C$ within an autoclave under a pressure of 10 to $15\,kg/cm^2$

The challenge with glass as a structural component is that the surfaces are covered with microscopical flaws. The strength of glass is governed by the distribution of these flaws, making the glass strength a stochastic property. The stochastic nature of glass fracture is rooted in the spatial distribution, size and shape of the microscopical surface flaws, which combined with the surface stress field determine the fracture strength [5]. As the surface flaw characteristics differ for every glass specimen, many experimental iterations are needed to map the fracture strength distribution for one test case. This is both costly and impractical. Because glass failure is governed by the surface flaw distributions, the strength is also related to the glass geometry. Larger glass components are weaker than smaller components because of a higher occurrence of flaws and an increased probability of critical flaws [11, 12]. The strength is also proven to be dependent on the loading duration and loading type [13, 14].

Back in 1921, Griffith [15] proposed a connection between the fracture stress and the size of the microscopical surface flaws present on glass surfaces. Griffith formulated a fracture theory stating that for a flaw to become unstable, and fracture to initiate, the potential energy reduction that results from an increment of crack growth has to overcome the surface energy of the material. Griffith proved his theory by correctly predicting the relationship between the fracture strength and the flaw size in glass specimens. Irwin [16] built on Griffith's theory by introducing a measure of the potential energy available for a crack growth increment, called the of energy release rate, $\mathcal{G}$, given by

$$\mathcal{G} = -\frac{d\Pi}{dA} \tag{1.1}$$

where Π is the potential energy of an elastic body and dA is the crack growth area. Later, Irwin [17] introduced the stress intensity factor, which describes the stresses and displacements near the crack-tip by a single constant. Depending on the crack loading mode, the expressions for the stress intensity factor vary. In the field of fracture mechanics, it is common to divide the crack loading modes into three distinct modes, i.e., mode I, II and III [18]. In mode I loading, often referred to as the opening mode, the principal load is applied normal to the crack plane and tends to open the crack. Mode II corresponds to in-plane shear loading and tends to slide the crack faces with respect to each other. Mode III loading is an out-of-plane shear loading. The mentioned loading modes can be combined to describe all kinds of complex loading modes, often referred to as mixed-mode loading. For mode I loading, the stress intensity factor, K_I, is given by

$$K_I = Y\,(a, c, \phi)\,\sigma_n \sqrt{\pi a} \tag{1.2}$$

where Y is a geometrical crack shape factor which is dependent on the flaw depth, a, the flaw half-length, c, and the parametric angle, ϕ, while σ_n is the external applied stress normal to the crack.

The microscopical surface flaws present on the glass surface, typically referred to as Griffith flaws [19–23], reduce the fracture strength of glass by several orders of magnitude. In theory, without the surface flaws, the fracture strength of glass is in the order of 10 GPa [24, 25]. In practice the fracture strength is in the order of 100 MPa. Glass fracture initiates in the microscopical surface flaws which may grow under loading. If the stress intensity, K_I, is sufficiently high and above a threshold value, K_{th}, but lower than the critical stress intensity, K_{IC}, the flaw may grow sub-critically. This phenomenon is often called sub-critical crack growth (SCG), but also known as stress corrosion or static fatigue. The rate of the sub-critical crack growth (SCG) is highly dependent on a combination of environmental factors, such as humidity and temperature, and the stress intensity [23, 26–33]. When the flaw grows sub-critically, the flaw depth and length increase, resulting in an increased stress intensity.

Eventually, with sufficient loading, the stress intensity will become critical, i.e., $K_I \geq K_{IC}$. At this point, the flaw exhibits unstable crack growth and failure is initiated. The resulting crack propagation is violent, with crack speeds reaching up to ~1500–1600 m/s [34, 35]. There are several important challenges regarding dynamic fracture characterization of soda-lime glass [36, 37]. First, the opening displacement at the crack tip is small, typically less than 100 nm [36]. Second, the crack growth process is highly transient, with crack speeds reaching up to ~1500–1600 m/s after a few microseconds [36, 38]. Third, the crack propagation typically involves branching. The crack propagation properties are affected by many aspects, including loading conditions, temperature, humidity, chemical composition, production method, and the presence of surface defects or impurities.

In the automotive industry, finite element (FE) simulations are typically used in the design process. Today, most commercial FE codes handle glass strength in a deterministic manner. This type of approach does not consider the varying fracture strength of glass. Yankelevsky [39] proposed an approach for predicting the fracture strength of glass plates. The proposed model is based on the fact that the probabilistic fracture behavior of glass originates from varying surface flaw distributions, or flaw maps, of glass plates. To imitate this behavior, the model produces a set of virtual flaw maps with varying flaw shape, size and location. The fracture strength is found by combining the information from the flaw maps and linear elastic fracture mechanics (LEFM) theory. However, the model does not take SCG into account. Later, other models predicting failure in glass based on flaw maps have been proposed [40–42]. The model of Yankelevsky was further developed by Osnes et al. [14, 43] into a post-processor for FE simulations.

The mentioned glass strength prediction models focus on finding the probability of failure in terms of fracture initiation, and do not consider the post-failure stage. In extreme load cases, like real car crashes or the NCAP-evaluation tests [44], both the pre- and the post-failure stages need to be considered. Brokmann [33] developed a model based on SCG and initial flaw sizes estimated from fracture stresses fitted to a Weibull probability distribution function (PDF). The model is integrated into an FE code as a material model, making the model more user friendly.

Modeling brittle fracture in an FE framework has proven to be a challenging task. In particular, the problem of how to represent the sharp crack discontinuity in an FE continuum has caught the

attention of many researchers. Techniques such as element erosion and node-splitting to drive cracking based on a local criterion are commonly used [45]. These techniques are typically prone to pathological mesh dependence, as the FE discretization determines the crack path resulting in the minimum potential energy. To mitigate the pathological mesh dependence, several non-local fracture formulations such as eigenfracture [46–50] and fracture phase-field [51–63] have been suggested.

To properly model the structural behavior of glass, both the stochastic fracture strength and the violent cracking behavior must be addressed. The lack of accurate numerical models that encorporate this behavior leads to more physical testing, which is both expensive and time consuming. For this reason, there is a need for numerical methods that can predict the fracture initiation and crack propagation in soda-lime glass.

1.2   Research Question and Objective

The main research question of this PhD thesis is:

How to predict fracture initiation and crack propagation in soda-lime glass?

The research question is twofold, where the first part is aimed at the probabilistic nature of glass, while the second part refers to the violent cracking of the material. Based on this, the main objective of the thesis is to *develop methods to capture fracture initiation and crack propagation of soda-lime glass in numerical simulations*. The aim is to increase the understanding of the mechanical behavior of glass through experimental studies and development of numerical models.

1.3   Scope

There are many aspects to consider when developing methods to capture fracture initiation and crack propagation of soda-lime glass in numerical simulations. Motivated by the challenges faced by the automotive industry and to maintain a focus on the stated objective, the thesis scope was restricted as follows:

- The experimental and numerical work was limited to studies on monolithic and single-layered laminated annealed soda-lime float glass specimens.

- The polymer interlayer of the laminated glass specimens was PVB. Characterization of the polymer interlayer was not within the scope of this thesis.

- Only plates and curved sheets are considered.
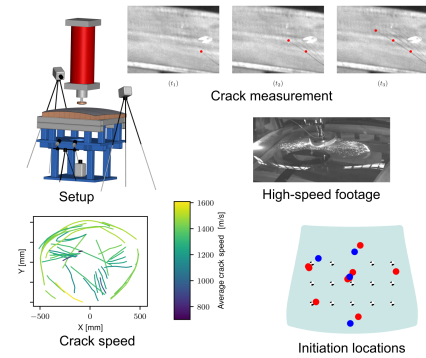
1.4   Contributions

To answer the presented research question, the thesis work is divided into two main parts, one focusing on fracture initiation where the focus is to improve the Glass Strength Prediction Model (GSPM) [14, 43] and one emphasizing crack propagation where the aim is to capture crack propagation paths and speeds found experimentally. To improve the GSPM, experiments on windshields were conducted and handling of the phenomena of SCG was included. To model crack propagation in glass, experiments on L-shaped glass specimens were conducted and used to validate the implementation of a fracture phase-field model with three tension-compression splits and a new crack driving force. Furthermore, with aim to characterize the surface flaws in glass, a cooperation with the Department of Physics at Norwegian University of Science and Technology (NTNU) was established to develop a methodology for investigation and characterization of the flaws [64]. The main contributions of the thesis are illustrated in Figure 1.2 and elaborated below:

1. Generation of a detailed database from three experimental test series on windshields using a proposed reliable experimental setup for quasi-static testing on windshield that allows for detailed extraction of important data, such as loading and deformation histories and crack propagation data. The test series consisted of windshields of varying geometry and production method.

2. Implementation and validation of an improved version of the GSPM including the phenomenon of SCG, capable of handling rate effects. The new version of the GSPM is implemented as a material model in the commercial FE code LS-DYNA, triggering fracture initiation of the existing glass material model MAT_280.

3. Generation of a database of 20 experiments on quasi-statically loaded L-shaped glass specimens using a proposed reliable experimental setup. The proposed setup allows for detailed extraction of the crack propagation path and speed for varying critical load levels.

4. Implementation and validation of fracture phase-field models for shell and solid elements in LS-DYNA with three tension-compression splits and a new crack driving force allowing the user to control the fracture initiation. Among the validations are known numerical experiments and the experiments on L-shaped specimens performed in Part 3.
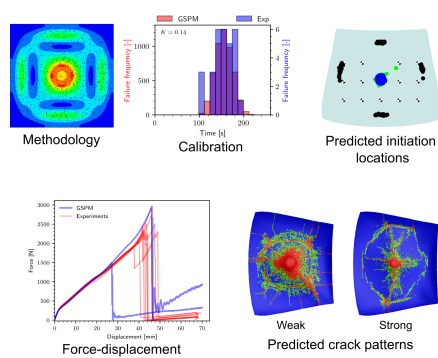
Figure 1.2: Overview of the main contributions from this thesis.

1.5 Journal article contributions

The research and results from the thesis have been submitted for possible publication in different scientific journals. These journal articles constitute the foundation of this work. The main journal articles of this thesis are listed below and will be referred to as Papers I, II, III and IV.

    I Rudshaug J., Hopperstad O. S., Børvik T., "Capturing fracture initiation and crack propagation of car windshields", Accepted for publication in Engineering Fracture Mechanics.

  II Rudshaug J., Aasen K. O., Hopperstad O. S., Børvik T., "A physically based strength prediction model for glass", Under review.

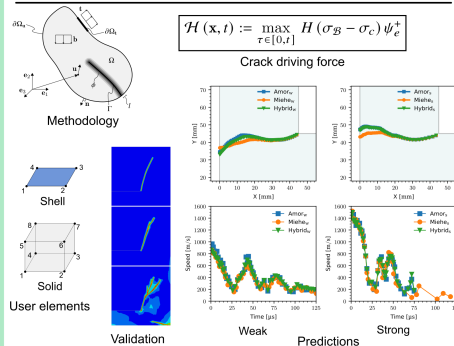 III Rudshaug J., Hopperstad O. S., Børvik T., "Effect of load level on cracking of L-shaped soda-lime glass specimens", Under review.

 IV Rudshaug J., Børvik T., Hopperstad O. S., "Modeling brittle crack propagation for varying critical load levels: A dynamic phase-field approach", Under review.

1.6 Conference contributions

The work has resulted in presentations at two international conferences:

- Rudshaug J., Hopperstad O. S., Børvik T. (2022), "Modeling of crack propagation in glass", Presented at the 11th European Solid Mechanics Conference, 4-8 July, Galway, Ireland.

- Rudshaug J., Hopperstad O. S., Børvik T. (2023), "Capturing fracture initiation and crack propagation of windshields", Presented at the 20th International Conference on Experimental Mechanics, 2-7 July, Porto, Portugal.

1.7 Other contributions

In a collaboration with the Department of Physics at NTNU, a method for characterizing the glass surface flaws was developed, presented in the letter below.

- Tekseth K. R. B., Rudshaug J., Mayani M. G., Akram M. N., Børvik T., Breiby D. W., "Mapping surface flaws on float glass through Fourier ptychographic quantitative phase imaging", Under review.

1.8   Outline of the Thesis

The thesis is divided into two main parts, one focusing on fracture initiation, and one focusing on crack propagation. Each part includes separate experimental and numerical parts as presented in Figure 1.2. The thesis follows the structure below:

- Fracture initiation

  I Experiments on Windshields, Chapter 2

  II Glass Strength Prediction Model (GSPM), Chapter 3

- Crack propagation

  III Experiments on L-shaped specimens, Chapter 4

  IV Phase-field approach to fracture, Chapter 5

Chapters 2 to 5 are based on Papers I-IV and presented as independent studies with individual introductions, discussions and conclusions. Chapter 6 presents the main conclusions from the thesis work and suggestions for further work.

2 Experiments on windshields

This chapter is based on Paper I, "Capturing fracture initiation and crack propagation of car windshields". The chapter presents the generation of a detailed database from three experimental test series on windshields of varying geometry and production method. A reliable experimental setup for quasi-static testing on windshield is presented. The setup allows for detailed extraction of important data, such as loading and deformation histories and crack propagation data.

2.1 Introduction

There is a pressing need for accurate numerical models in the automotive industry to reduce the number of physical experiments during the development of new cars. Some car components, like the windshield, exhibit a stochastic behavior that increases the number of experiments necessary to validate the car design. This stochastic behavior is difficult to capture both experimentally and numerically, and the development of accurate numerical models that predict the stochastic behavior relies on more detailed experimental data.

Windshields are a type laminated safety glass that typically consist of two curved glass layers and a polyvinyl butyral (PVB) interlayer. The combination of glass and PVB provides beneficial properties in terms of injury reduction during a crash situation, burglary protection and protection against wind-borne debris. A single glass layer is a weakest link structure, meaning that any crack leads to total failure because the structure does not provide alternative load paths in the event of local failures [5]. Laminated glass, on the other hand, is a fail-safe structure, because the PVB interlayer keeps the glass layers tied together after initial failure of the glass [6]. In the case of windshield fracture, the PVB interlayer will keep the glass fragments together. As the glass layers break, the windshield essentially goes from acting as a laminated composite to a glass-reinforced polymer. The structural behavior of the laminated glass can be subdivided into the following five phases as presented by Larcher et al. [7, 8] in Figure 2.1:

1. Linear, elastic behavior of the glass layers

2. One of the glass layer breaks, while the other layer is still intact

3. The other glass layer fails and the polymer interlayer behaves elastically

4. The interlayer deforms inelastically while keeping the glass fragments together

5. The interlayer fails by either reaching its failure strain or being cut by the broken glass
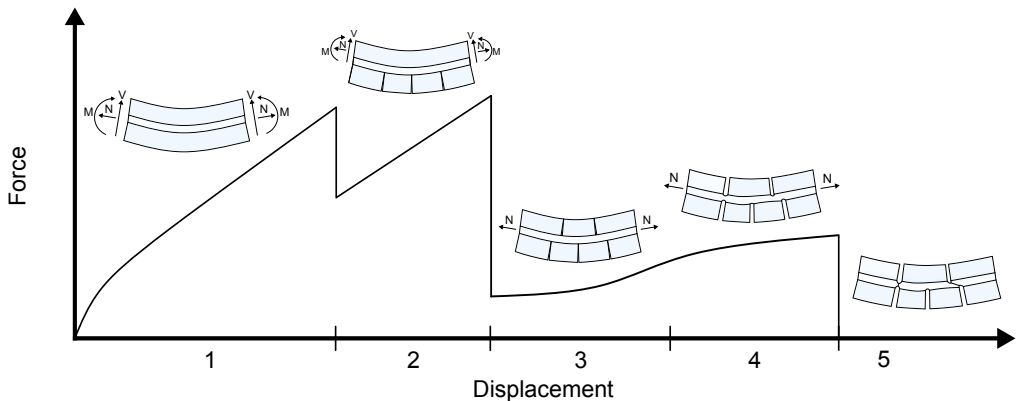
Figure 2.1: The failure phases of laminated glass, adapted from Larcher [8].

The challenge with glass is that the surfaces are covered with microscopical flaws. The strength of glass is governed by the distribution of these flaws, making the glass strength a stochastic property. Failure initiates for a critical combination of surface flaw distribution and surface stress field [5]. Because glass failure is governed by the surface flaw distributions, the strength is also related to the glass geometry. Larger glass components are weaker than smaller components because of a higher occurrence of flaws and an increased probability of critical flaws [11, 12]. The strength is also proven to be dependent on the loading duration and loading type [13, 14].

To provide clarity, we use a general definition for the layers and sides of the windshields. The definitions are inspired by Zhao et al. [65] and Brokmann et al. [66], who used them for automotive windshields, and Winkelmann [67], who used them for insulated glass units. The definitions of the layers and sides are presented in Figure 2.2. The outer surface (Side 1) is visible for a pedestrian, while the inner surface (Side 4) is facing the driver. Sides 2 and 3 are the surfaces on which the outer and inner glass layer are bonded to the PVB interlayer.
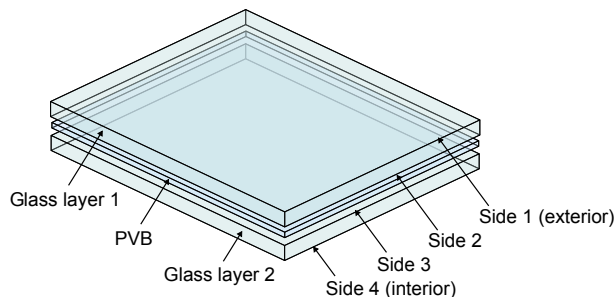

Figure 2.2: Definition of the layers of laminated glass for automotive windshields adopted from [66].

An important part of experimental work on laminated glass is related to the acquisition of relevant data. To facilitate the validation of numerical models, it is important to gather data on the applied loading as well as the windshield component behavior. Typically, in rapid load cases like head impact test series [68] the acceleration of the head is measured. For quasi-static load cases, the force and displacement histories of the impactor are measured. To obtain data on the component behavior, 3D-Digital Image Correlation (3D-DIC) methods are typically used [14]. To account for the stochastic nature of glass, fracture initiation data is also of significant interest, both in terms of initiation location and loading state. There are several ways of measuring the fracture initiation locations. One method is called acoustic emission (AE) localization, which is based on measuring the acoustic waves passing through the observed medium at material failure. By using for instance the time difference of arrival, one can calculate the location of the signal source, and thus the fracture initiation point [66, 69, 70]. Another option is to use fractography methods to locate the fracture initiation point after the experiment is finished [71]. A third option is to use high-speed cameras to estimate the fracture initiation locations. With this method, the image coordinates must be related to the spatial coordinates of the component and the fracture initiation point must be visible. A benefit of using high-speed cameras is that other valuable data like crack propagation and speed can be gathered simultaneously with the same equipment.

Many experimental studies have been performed on multiple types of laminated glass components exposed to a variety of loading conditions. These include drop tower experiments [14, 72, 73], blast loading experiments [43, 45, 74–77] and ballistic impact experiments [45, 78–84] on flat laminated glass plates, bird strike impact on aircraft windshields [85, 86], and impact loadings on car windshields [33, 87–96]. Segura Santillana et al. [92] performed a total of 90 head impact experiments on windshields covering 16 impact points. Alter et al. [95] conducted eight head impact experiments with a head velocity of $10\,\mathrm{m/s}$ using four different configurations, where three of the tests were on the center of the convex side of the windshield, three were on the center of the concave side, and one was on an eccentric position on the convex side with a windshield thickness of $2\,\mathrm{mm} \times 1.8\,\mathrm{mm}$. In addition, they performed one test on the center of the convex side of a windshield with a thickness of $2\,\mathrm{mm} \times 2.1\,\mathrm{mm}$. They reported large butterfly-like fracture patterns for the convex-side tests, and smaller circular patterns for the concave-side tests. In addition, they reported that glass layer two failed first in the event of a pedestrian head impact on glass layer one, while glass layer one failed secondary. Yu et al. [96] performed five head impact test at five different target points using the same initial velocity and reported similar observations as Alter et al. [95] regarding the temporal failure order of the glass layers. Brokmann et al. [66] conducted 20 quasi-static tests on windshields loaded by a head impactor. They determined the failure initiation locations by AE localization, and used fracture mirrors to determine the failure stresses. Furthermore, they estimated the critical flaw sizes based on the failure stresses. Manthei et al. [69] and Alter et al. [70] also used AE localization to determine failure initiation locations.

In this study, we aim to develop, apply, and evaluate an experimental setup for car windshields subjected to quasi-static loading with controlled boundary conditions. The experimental procedure is performed for three types of windshields: one from a coupe car, tested ten times, one from a sports utility vehicle (SUV), tested ten times, and one from an SUV concept car, tested eleven

times. With the experimental setup, we provide statistics on the strength of windshields through fracture initiation distributions and loading information. First principal stress levels at fracture are estimated by combining experimental data and numerical simulations. Using synchronized high-speed cameras, we provide valuable information about the failure behavior in terms of crack patterns and estimations of crack propagation velocities.

2.2 Experimental program

In this study, we aim to develop an experimental setup for windshields exposed to quasi-static loading which can provide data on fracture initiation locations, crack propagation path and speed, impact force history and windshield displacement field.

The involved materials and equipment used in this experimental work are presented below.

2.2.1 Materials

The windshields consist of two curved glass layers and a PVB interlayer ordered as illustrated in Figure 2.2. They were supported by customized frames made of oak which were milled to match the windshield curvatures. To load the windshields we used a flattened impactor also made of oak. We applied oak because of its strength and machinability [97].

The glass layers of the windshields are made of annealed soda-lime-silica glass. Glass is a brittle and transparent material, which behaves elastically to the point of failure. Theoretically, the strength of glass is in the order of 10^5 bar (or 10 GPa) [24, 25]. In practice the strength is several orders of magnitude lower, which arises from the stress-raising microscopic flaws on the glass surface, typically referred to as Griffith flaws [15, 19–23]. Failure initiates in these microscopical surface flaws, which grow under loading until the stress intensity becomes critical. At this point, the flaw exhibits unstable crack growth and failure is initiated. The crack speeds in glass can reach up to ~1500 m/s [34]. Since the failure mechanism is governed by microscopical surface flaws, glass exhibits a stochastic fracture behavior. The stochastic nature of glass is rooted in the distribution and shape of the microscopical surface flaws. As the surface flaw characteristics differ for each glass specimen, many experimental iterations are needed to map the strength distribution for one test case. According to Yankelevsky [39], up to 5000 iterations may be necessary. This is both costly and impractical.

PVB is the most common interlayer in safety glass and windshields, valued for its adhesion properties to glass as well as its ability to isolate sound and absorb both UV-light and energy [98]. The mechanical behavior is highly non-linear and strain-rate dependent, and it is highly affected by its environment, such as exposure to UV-light, temperature and humidity.

2.2.2 Specimens

The study consisted of three test series of windshields with varying geometries. The test matrix in Table 2.1 contains information about the windshield type, number of specimens, size, layer thickness, development stage and production year.

Table 2.1: Test matrix presenting the tested windshield types with information about quantity, size, layer thickness, development stage and production year.

Type	#	Size [m^2]	Layer thick. [mm] Layer 1 | PVB | Layer 2	Dev. stage	Prod. year
Coupe car	10	1.13	2.1 | 0.76 | 1.6	Production	2021
SUV	10	1.62	1.8 | 0.76 | 1.8	Production	2022
SUV concept	11	1.77	2.1 | 0.76 | 1.6	Concept	2017

The involved windshields cover different aspects in terms of size and production quality. The SUV and SUV concept windshields are large windshields, typically found in SUVs. The SUV concept windshields are produced at an early development stage, while the SUV windshields are produced after the final development stage. Since the production tolerances decrease as the development process evolves, we had greater deviations between the windshield hardware and the computer-aided design (CAD) geometry for the SUV concept windshields. For this particular reason, we scanned four of the SUV concept windshields with a Handyscan 700 laser scanner [99] to extract the hardware geometry for that specific test series. The laser scans were used to construct an average geometry to serve as a basis for the design of the wooden frame and finite element (FE) models. The SUV and coupe car hardware geometries did not deviate from the respective CAD geometries. The SUV windshields (1.62 m^2) were a bit smaller than the SUV concept windshields (1.77 m^2). The coupe car windshields were much smaller (1.13 m^2).

2.2.3 Experimental setup

The experimental setup is displayed in Figure 2.3 (a), and consists of an oak frame on top of a steel support structure, the windshield placed on the oak frame, an oak impactor mounted on a stiff press with a load cell, two cameras used for 3D-DIC and three high-speed cameras.
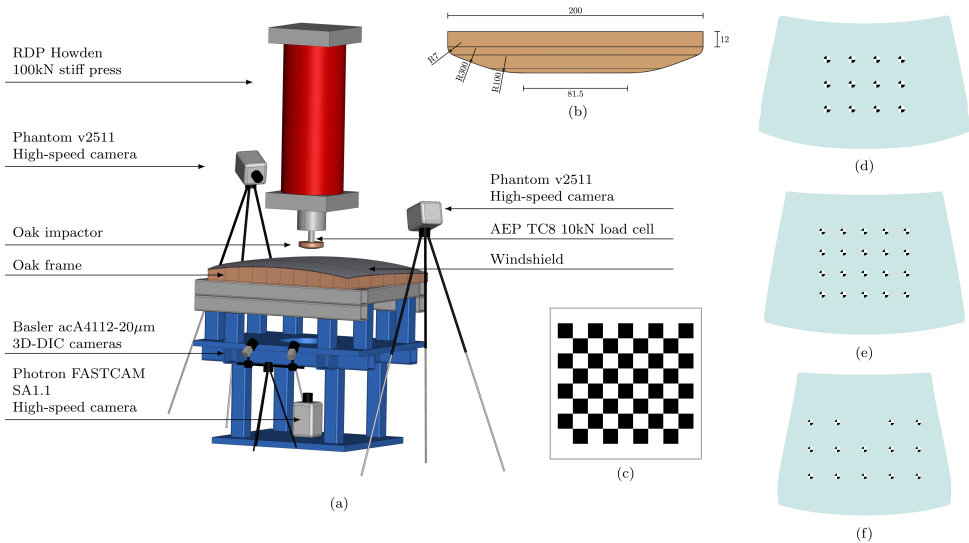
Figure 2.3: Illustration of the experimental setup: (a) an overview, (b) the oak impactor, (c) the camera calibration pattern, the placement of the target stickers for (d) the coupe car, (e) the SUV, and (f) the SUV concept windshield.

For each of the windshield types in Table 2.1, we produced a wooden frame made of English Oak. The frames were designed based on the CAD geometries of the coupe car and SUV windshields, and an averaged laser scanned geometry for the SUV concept windshields. A frame thickness of 140 mm was chosen to suppress stress concentrations near the windshield edges and thus prevent fracture initiation at the edges and to ensure steady boundary conditions. Some snapshots of the milling process are shown in Figure 2.4. After the frame was milled, it was mounted on a 10 mm thick steel plate which was cut based on the frame geometry. The steel plate added extra stiffness to the frame. Finally, the frame steel plate was spot welded to the testing rig.
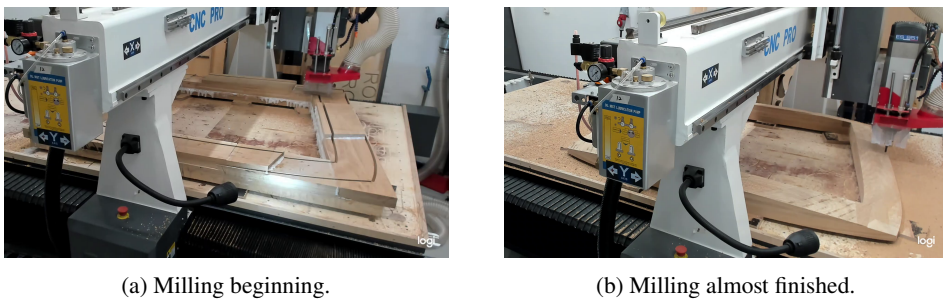

(a) Milling beginning.

(b) Milling almost finished.

Figure 2.4: Oak frame milling process.

We used the same geometry of the impactor as Osnes et al. [14]. The wooden impactor was also made of English Oak and used in all the experiments. The diameter of the impactor is 200 mm and is presented in Figure 2.3 (b). The flat geometry was chosen to reduce the stress concentrations near the impactor. This allows for a larger area of probable fracture initiation sites, which again enables the experimental setup to display the probabilistic nature of glass.

Several cameras were used to monitor the component displacement and capture the crack propagation pattern at failure. Two synchronized Basler acA4112-20 µm Digital Image Correlation (DIC) cameras were placed facing the bottom of the windshield as shown in Figure 2.3 (a). The high-speed cameras were used to capture fracture initiation locations and crack propagation patterns. To ensure that the whole windshield surface was covered, the two synchronized Phantom v2511 high-speed cameras [100] were placed at the diagonal line overseeing the top of the windshield, while the Photron FASTCAM SA1.1 high-speed camera [101] was placed underneath the windshield and impactor, see Figure 2.3 (a). Since the images were stored in endless loops in the high-speed cameras, storing the last couple of seconds of recording, the cameras were manually triggered at fracture initiation.

To extract displacement data from the tests we made use of 3D-DIC point tracking. We marked specified points, i.e., optical targets, with target stickers on the bottom side (Side 4) of the windshields. To ensure consistent placement of the target stickers, we produced a rubber mat for each windshield type with holes in specified locations. The target stickers were placed in symmetric grid patterns to facilitate validation of the symmetry of the displacement field. Figure 2.3 (d, e, f) shows the target stickers location on the respective windshields. The DIC cameras were calibrated using a 9×8 checkerboard calibration target shown in Figure 2.3 (c). Each checkerboard square is $4\,cm \times 4\,cm$. The total dimensions of the calibration plate is $40\,cm \times 40\,cm$.

The DIC analysis was performed with an in-house DIC software developed in Python [102] using features in OpenCV [103] and Deep Learning features in PyTorch [104]. To calibrate the DIC cameras, we took approximately one hundred synchronized photos with the calibration target placed in varying positions and angles. The automated calibration procedure locates the checkerboard for each photo and use the checkerboard coordinates to map the image coordinates to spatial coordinates. The optical targets were found with help from a trained neural network, and sorted and ordered row-wise by a K-means clustering procedure. Later, we tracked the displacement of the optical targets with tracking procedures found in OpenCV.

The experiments were conducted using a RDP Howden 100 kN stiff press at the Structural Engineering Laboratory at the Norwegian University of Science and Technology (NTNU). We used an AEP TC8 10 kN load cell to ensure accurate force measurements. All the experiments were performed indoors at a room temperature of 23 °C and a relative humidity of 38 % rh. To ensure reproducible results, we followed a strict testing routine described in Box 2.1.

1. **Prepare glass specimens**
    (a) Lift the windshield from the storage container using suction cups
    (b) Inspect component for damage and imperfections
    (c) Clean the windshield
    (d) Apply optical target stickers
2. **Prepare test set-up**
    (a) Place the windshield on the wooden frame
    (b) Ensure that the specimen is centered under the impactor
3. **Testing**
    (a) Apply a total displacement of 40 mm, 60 mm and 70 mm at a velocity of 13 mm/min for the coupe, SUV and SUV concept car, respectively
4. **Track data**
    (a) Track load and displacement from load cell
    (b) Capture DIC images from the Basler cameras with a frame rate of 1 fps
    (c) Capture high-speed images from the Phantom cameras at a frame rate of 33 000 fps for the coupe car and SUV, and 25 000 fps for the SUV concept car
    (d) Capture high-speed images from the Photron camera at a frame rate of 5000 fps
5. **After testing**
    (a) Locate and register potential fracture initiation locations
    (b) Clean and vacuum the set-up for glass fragments
    (c) Clean impactor for potential glass fragments

Box 2.1: Windshield testing procedure.

2.2.4 Post-processing tool for crack initiation and crack propagation

To facilitate extraction of crack initiation and crack propagation data we developed an in-house post-processing tool based on pose estimation from a known 3D model [105]. In short, pose estimation involves computing the real-world position and orientation of the camera based on known 3D features and their projections onto the image plane. The pose estimation process is illustrated in Figure 2.5. Let $\mathcal{F}_c$ be the camera frame and $^c\mathbf{T}_w$ the transformation from $\mathcal{F}_c$ to the real-world frame, $\mathcal{F}_w$. The homogeneous transformation matrix, $^c\mathbf{T}_w$, is defined as

$$^c\mathbf{T}_w = \begin{pmatrix} ^c\mathbf{R}_w & ^c\mathbf{t}_w \\ \mathbf{0}_{3\times 1} & 1 \end{pmatrix} \tag{2.1}$$

where $^c\mathbf{R}_w$ and $^c\mathbf{t}_w$ are the rotation matrix and translation vector defining the real-world camera orientation and position.
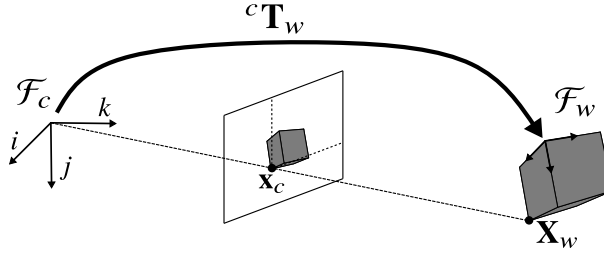
Figure 2.5: Illustration of a rigid transformation ${}^{c}\mathbf{T}_{w}$ between the world frame $\mathcal{F}_{w}$ and the camera frame $\mathcal{F}_{c}$ and the framed perspective image projection. $\mathbf{X}_{w}$ is a real-world point and $\mathbf{x}_{c}$ is the perspective projection of $\mathbf{X}_{w}$.

The perspective projection $\mathbf{x}_{c} = (x, y, 1)^{\intercal}$ of a point $\mathbf{X}_{w} = (X_{w}, Y_{w}, Z_{w})^{\intercal}$ is given by

$$\mathbf{x}_{c} = \mathbf{\Pi}^{c}\mathbf{T}_{w}\mathbf{X}_{w} \tag{2.2}$$

The corresponding perspective image projection $\bar{\mathbf{x}}_{c} = (u, v, 1)^{\intercal}$ is given by

$$\bar{\mathbf{x}}_{c} = \mathbf{K}\mathbf{x}_{c} \tag{2.3}$$

where $\mathbf{K}$ is the camera intrinsic matrix, defined by

$$\mathbf{K} = \begin{pmatrix} p_x & 0 & u_0 \\ 0 & p_y & v_0 \\ 0 & 0 & 1 \end{pmatrix} \tag{2.4}$$

where $(u_0, v_0, 1)^{\intercal}$ are the principal point coordinates defining the intersection of the optical axes and the image plane, $p_{x/y}$ are the ratios between the focal length of the lens f and the size of the pixel $l_{x/y}$, i.e., $p_{x/y} = f/l_{x/y}$. $\mathbf{\Pi}$ is the projection matrix, given by

$$\mathbf{\Pi} = \begin{pmatrix} 1 & 0 & 0 & 0 \\ 0 & 1 & 0 & 0 \\ 0 & 0 & 1 & 0 \end{pmatrix} \tag{2.5}$$

To estimate the real-world position and orientation of the camera and construct the transformation matrix, ${}^{c}\mathbf{T}_{w}$, we used the open-source pose estimation routines available in OpenCV [106]. The optical target stickers were used as the target 3D features for the pose estimation procedure. Figure 2.6 presents an example of a pose estimation for the first coupe car test.
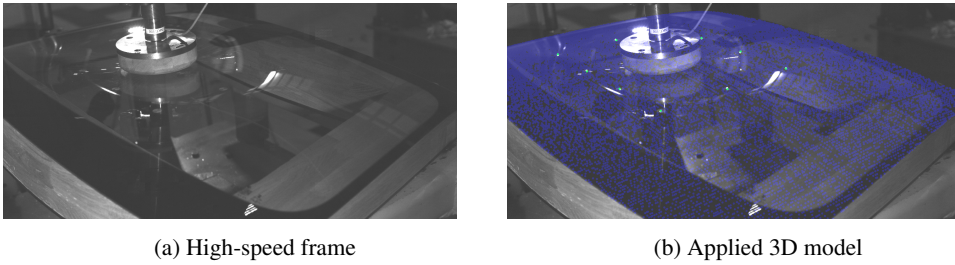
(a) High-speed frame

(b) Applied 3D model

Figure 2.6: Example of a pose estimation on the first coupe car test. The high-speed image frame (a) and the applied 3D geometry (blue dots) from the pose estimation (b). The known optical target sticker locations (white dots) and the re-projected optical sticker locations (green dots) were used to estimate and validate the pose estimation procedure.

After mapping the 3D model of the windshields to the high-speed camera footage, we obtained the real-world coordinates from the image coordinates. The fracture initiation locations and crack propagation data were gathered in a manual procedure where the crack tip was identified through visual inspection and given a 3D coordinate and time stamp. Figure 2.7 presents an example of a crack measurement, where the crack tip is registered for each image frame. By assuming zero curvature in-between the estimated incremental crack tip points, we estimated the crack propagation path and average speed. We define the average crack speed as the crack path length relative to the growth time.
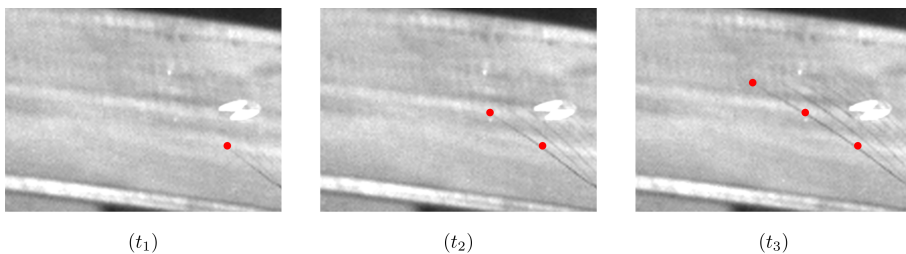

(t_1)

(t_2)

(t_3)

Figure 2.7: Example of a crack measurement. The crack tip coordinate is registered frame by frame as long as the crack tip is visible. Here, the procedure is shown for three image frames (t_1, t_2 and t_3).

2.3   Experimental results

The force versus displacement results and the fracture initiation locations for all the conducted tests are presented in Figure 2.8. In addition, the fracture initiation location data are compiled in Tables A.1 to A.3 in Appendix A.1. The fracture initiation locations were registered using the in-house post processing tool described in Section 2.2.4 for crack initiation and crack propagation. We note that the stiffness response before fracture is repeatable within each test series. For the coupe car, the component strength, here defined as the ultimate load bearing capacity until both glass layers fail, varies between ~1500 N and ~4500 N and we experience component failure in two distinct steps. We were not able to determine at which glass layer fracture initiates, however, it is clear that fracture first initiates under the impactor for one of the glass panes. Then, the other glass pane carries the load for a period of time until fracture also initiates in that glass pane. After both glass panes fail, we see that the load carrying capacity is low. At this point, the load is carried solely by the resulting glass-reinforced polymer interlayer. This two-stage failure behavior is clearly visible in Figure 2.8 (a) and fits well with the first two phases described by Larcher et al. [7, 8], see Figure 2.1. Most of the fracture initiation points in Figure 2.8 (d) for the coupe car are located near the loading point under the impactor. We see that the initiation location distributions of the first and second fracture occurrences are very similar. In addition, we have two initiation points that deviate from the others, located on the lower right hand side and to the left of the center. For the SUV, the component strength varies between ~1550 N and ~2300 N. As for the coupe car we also experience component failure in two distinct steps, which is clearly visible in Figure 2.8 (b). We see a different fracture initiation location distribution in Figure 2.8 (e) for the SUV compared to the coupe car. All the first fracture occurrences are closely gathered in the center, while the second fracture occurrences are located near the boundaries. For the SUV concept windshields the component strength varies between ~1600 N and ~2900 N. Also here we see that the component failure evolves in stages, where one glass layer fractures before the other. However, this behavior is less visible in Figure 2.8 (c) for components where the separate stages occurred with close proximity. This happens as a consequence of the low loading velocity, which leads to small differences in displacement of events occurring in close temporal proximity. Regarding the fracture initiation locations in Figure 2.8 (f), we see more spread distributions of the first and second fracture occurrences. Here, we can separate the initiation locations into two groups, one located in the center, and one located near the boundaries.

From Figure 2.9 we see the deformation history of some chosen target stickers for a representative instance of each of the three test series. For all three test series, the deformation fields are symmetric about the YZ-plane at X equal to zero. Note that the corner points for the coupe car exhibit significantly less displacement than what is the case for the SUV and the SUV concept windshields. A force level drop is visible for all the windshield types. This drop occurs due to failure of the windshield glass layers. For some of the target stickers, we note that the displacement decreases during this force level drop. The decrease in target sticker displacement is linked to a snap-back of the windshield when the windshield glass layers fail. The resulting windshield functions more like a PVB plate reinforced with glass fragments, which is much more flexible than the undamaged windshield, and thus the reinforced PVB plate is able to wrap around the

impactor, making some of the target sticker points move upwards.

Figure 2.10 displays the crack propagation pattern for SUV concept windshield number three. The time-lapse on the left hand side was taken by Camera 1, while the time-lapse on the right hand side was taken by Camera 2. The crack propagation pattern captured by Camera 1 evolves into two petal-like shapes towards the sides of the windshield, initiating from underneath the impactor. When studying the same crack propagation pattern from the angle of Camera 2, we observe a different type of shape, where fracture initiates underneath the impactor and propagates with one petal-like shape towards the bottom center of the windshield. The visual difference can be explained by how the cracks were oriented in relation to the light source and the camera. The cracks we see were oriented such that the light from the lightning sources reflected on the crack surface and hit the camera. For this reason, it was hard to capture the entire crack propagation process.

In Figure 2.11, we present the final fracture patterns of the ten coupe car windshield tests. The crack patterns consist of radial cracks with origin underneath the impactor and circumferential cracks at the border of the radial cracks. For tests 1, 5 and 8, we had circular shaped circumferential cracks, while they were elliptically shaped for the remaining tests. We note a substantial variation in the size of the crack patterns, from the crack pattern of test 5 which is nearly equal to the impactor size, to the crack pattern of test 9 that covers almost the entire windshield surface.

Figure 2.12 and Figure 2.13 display the crack propagation data gathered using the in-house post-processing tool. Figure 2.12 shows the measured average crack speed distributions for the three test series. We note that the speed levels are similar for all the test series, even though the load level at failure is different. The estimated crack speeds display a spread spanning from ~700 m/s up to ~1600 m/s. Figure 2.13 shows the crack patterns with corresponding average crack speed, which indicates that the circumferential cracks were much faster than the radial ones.
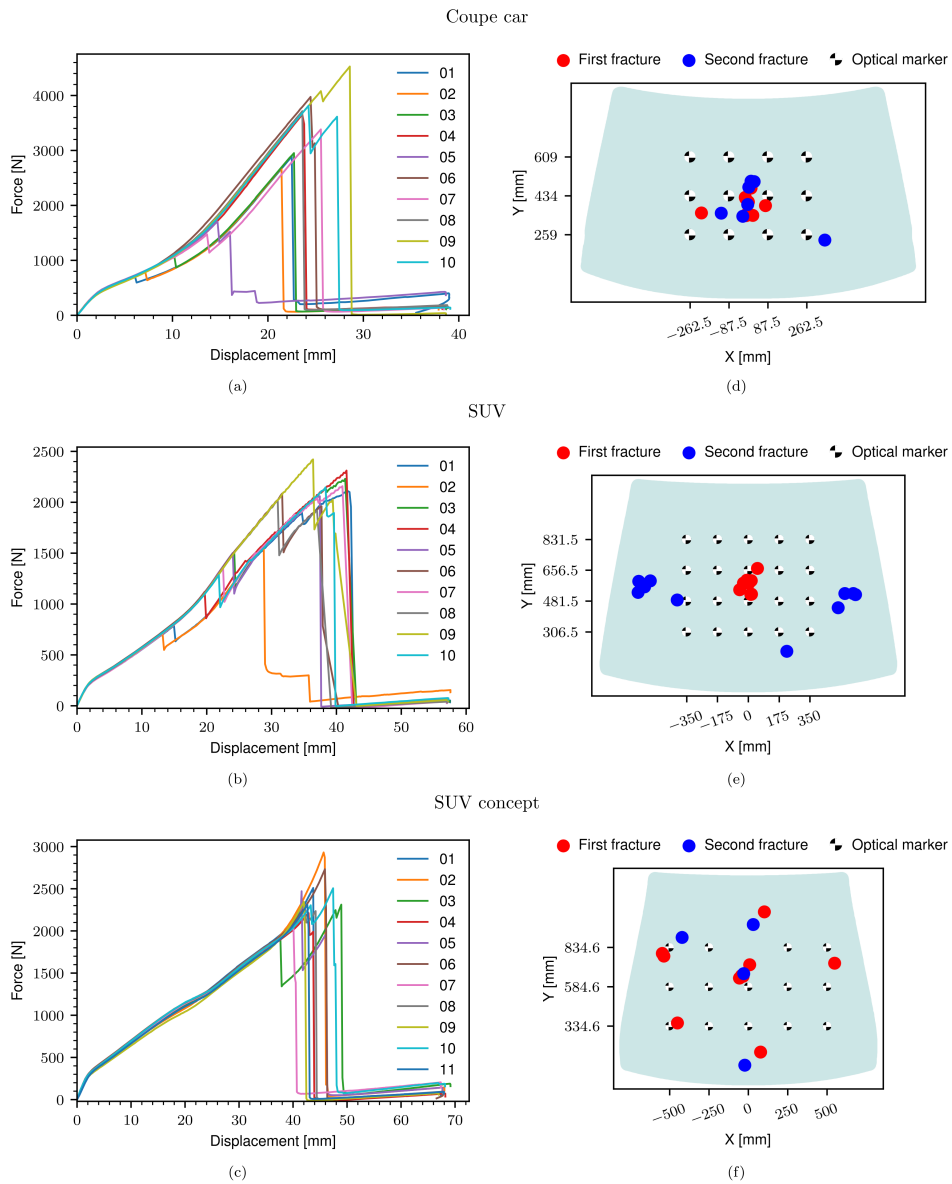
Figure 2.8: Force-displacement curves (a, c, e) and the fracture initiation locations (b, d, f) for the three windshield test series. The coupe car results are displayed on the top row (a,c), the SUV on the mid row (b, d), and the SUV concept on the bottom row (c, f).

Coupe car

(a)

(d)

SUV

(b)
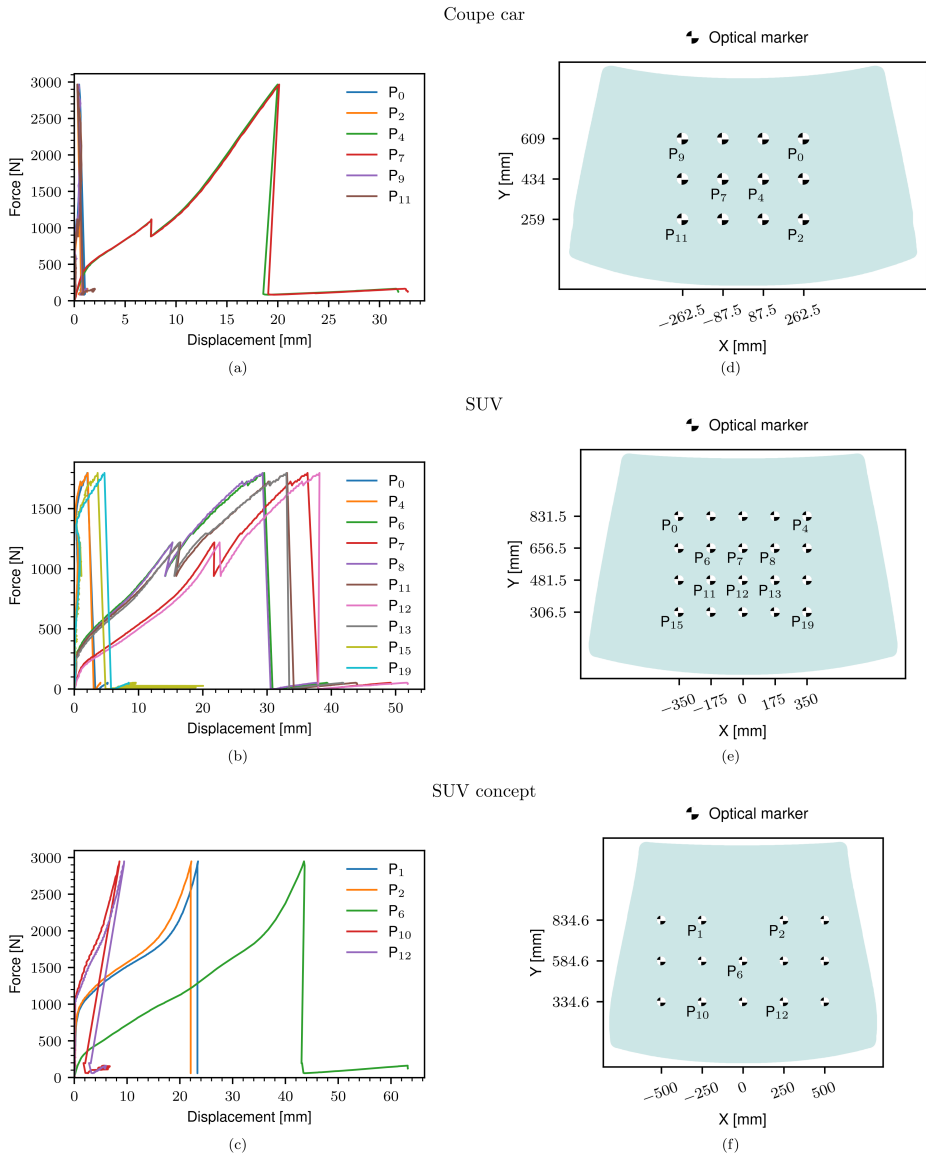
(e)

SUV concept

(c)

(f)

Figure 2.9: Force versus target sticker displacement for a selected test instance of each test series (a, b, c) and the location of the tracked target stickers (d, e, f). The coupe car results are displayed on the top row (a,c), the SUV on the mid row (b, d), and the SUV concept on the bottom row (c, f).

$t = 0\,\mathrm{\mu s}$

$t = 0\,\mathrm{\mu s}$

$t = 60.6\,\mathrm{\mu s}$

$t = 60.6\,\mathrm{\mu s}$

$t = 121.2\,\mathrm{\mu s}$

$t = 121.2\,\mathrm{\mu s}$

$t = 272.7\,\mathrm{\mu s}$

$t = 272.7\,\mathrm{\mu s}$
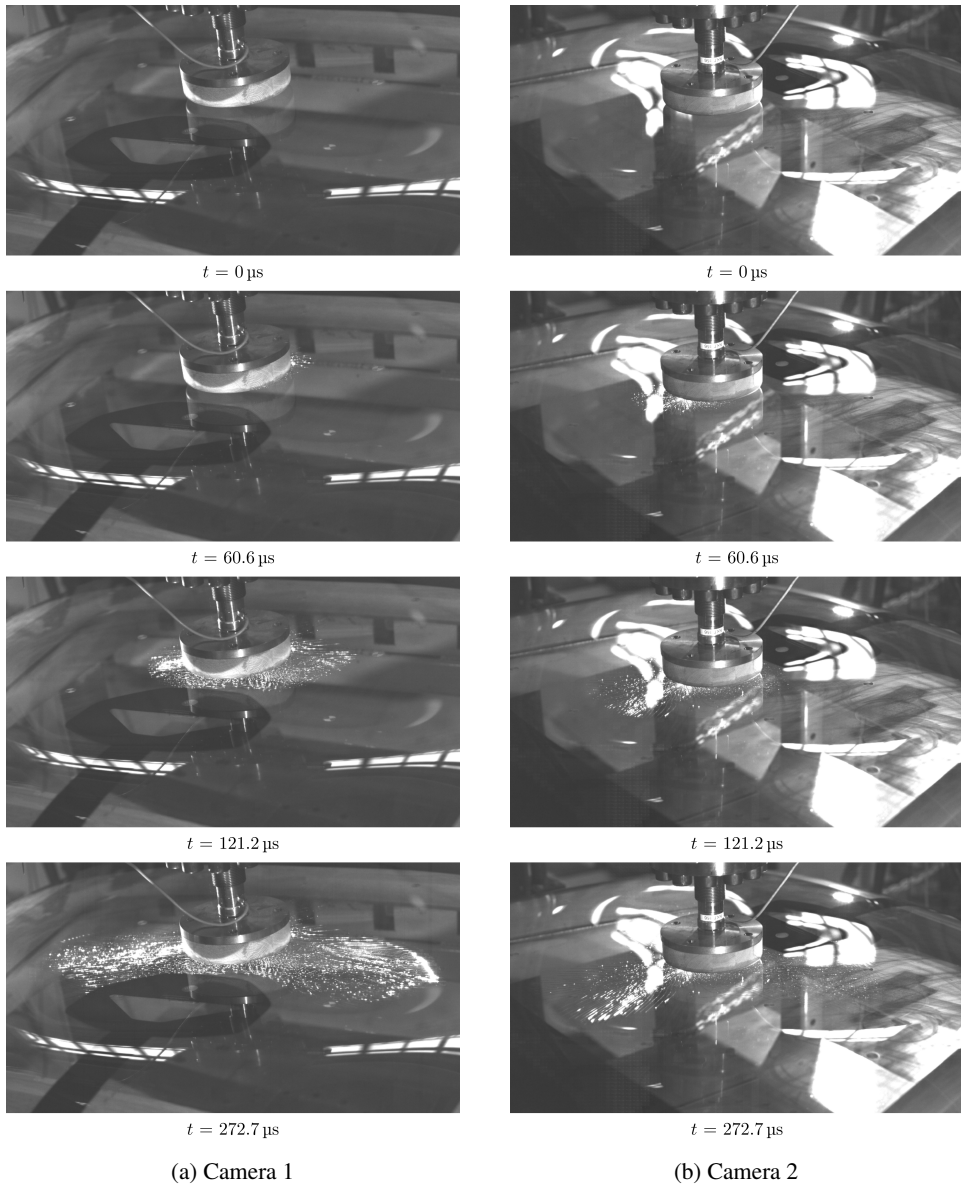
(a) Camera 1

(b) Camera 2

Figure 2.10: Crack propagation pattern from both the upper high-speed cameras for SUV concept windshield number three. The time-lapse on the left hand side was taken by camera 1, while the time-lapse on the right hand side was taken by camera 2.

(1)

(2)

(3)

(4)

(5)

(6)

(7)

(8)

(9)

(10)
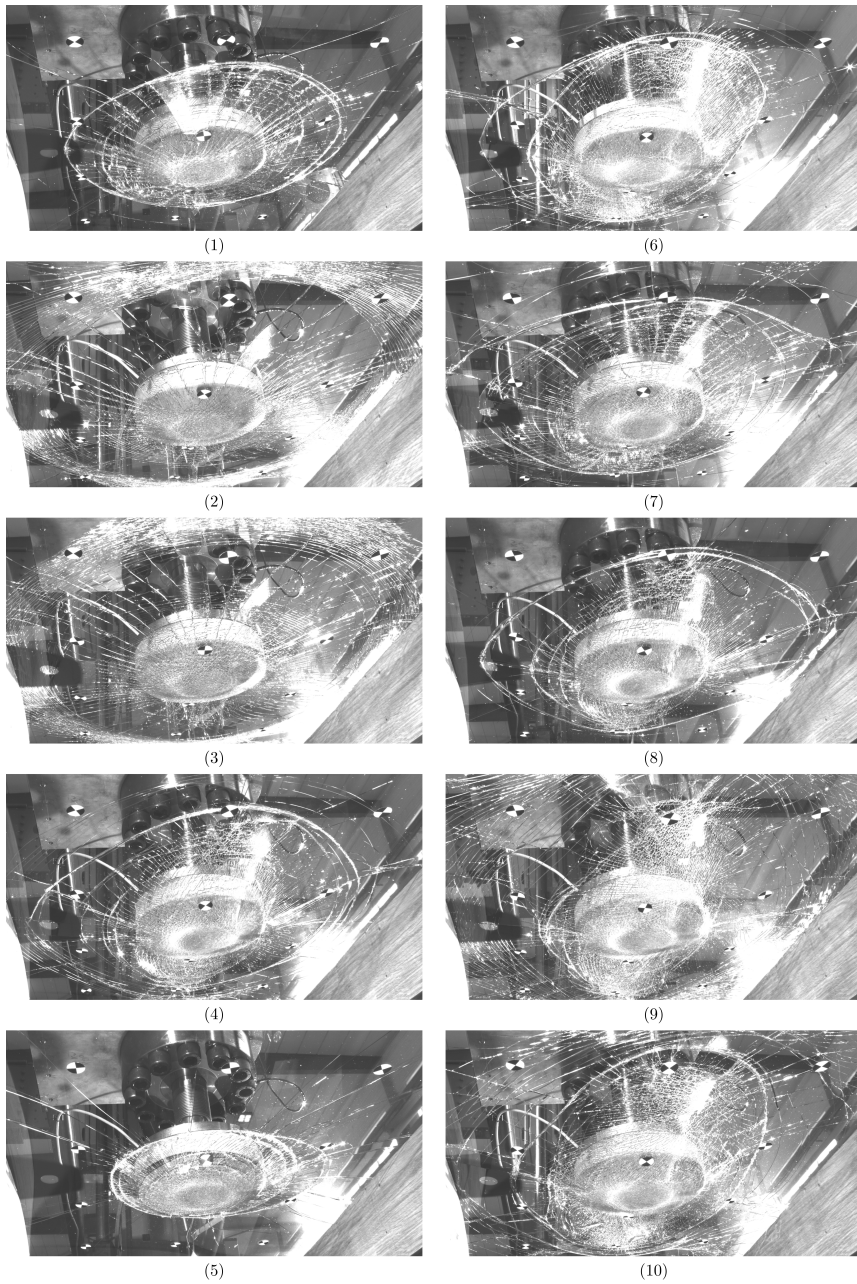
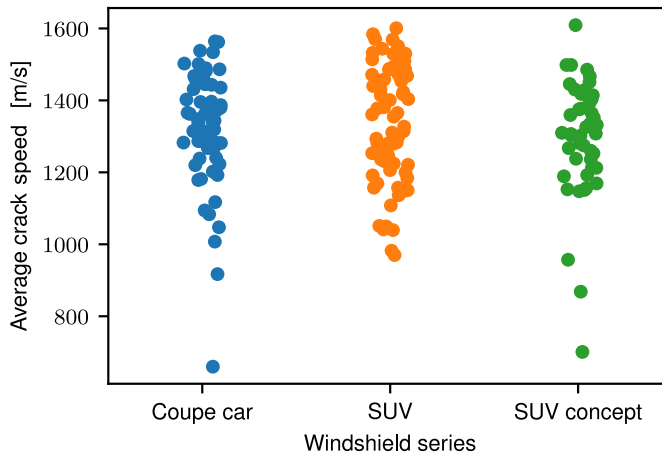Figure 2.11: Crack patterns for the coupe car labeled by test number.

Figure 2.12: Distribution of average crack speed for the measured crack paths for each test series.
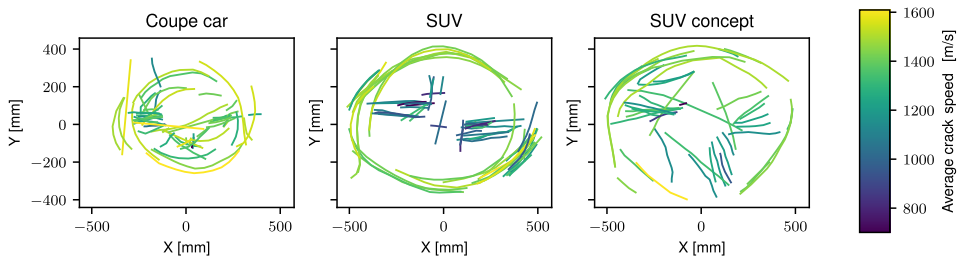

Figure 2.13: Measured crack paths colored based on average crack speed for each test series.

2.4 Numerical simulations

We performed damage-free FE simulations in LS-DYNA using the implicit solver to obtain approximated windshield stress fields during moments of interest in the experiments. The windshield was modeled using the same modeling technique presented in Alter et al. [95] and Brokmann et al. [66], which is also commonly used in the automotive industry. The technique involves modeling the windshield as a coincident shell-solid-shell where the shells and solid share nodes. We maintained the physical geometry by shifting the reference surface of the glass layer shell elements by half of the layer thickness and merge them with the upper and lower surface of the PVB layer, as illustrated in Figure 2.14. An average element length of 7 mm was used.
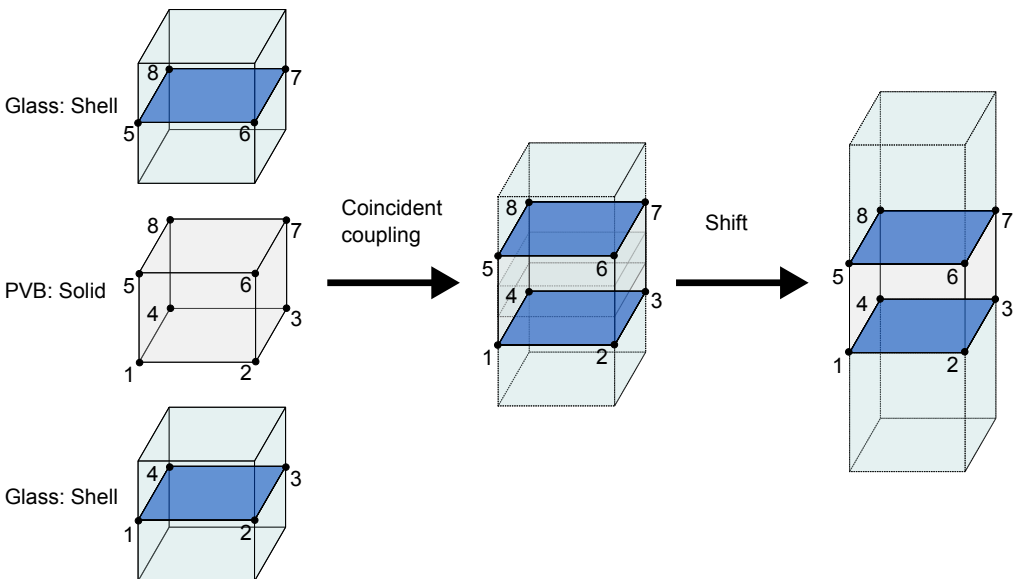

Figure 2.14: Coincident coupling of the windshield layers with shell elements for the glass layers and solid elements for the PVB layer. First presented by Alter et al. [95].

Both glass layers were modeled as linear elastic, with a Young's modulus of 70 GPa and a Poisson ratio of 0.23. The PVB was modeled using the Blatz-Ko rubber model, where the constant shear parameter was fitted through reverse engineering, starting at a suitable value for the present test velocity and room temperature [107, 108]. We selected this simple representation of the PVB to ensure that the windshield stiffness from the experiments was reproduced numerically. For the coupe car, a constant shear modulus of 1.4 GPa was chosen. For the other car types, 0.75 GPa was used. The glass layers were modeled with fully integrated, four-node shell elements and five integration points through the shell thickness. To have accurate stress values on the glass layer surfaces, we used the Gauss-Lobatto integration algorithm. This integration algorithm comes with the advantage of having integration points directly on both the shell element surfaces. Therefore, no stress extrapolation to the element surface where the microscopical flaws were located was

necessary. The PVB interlayer was modeled using selectively reduced solid elements with eight integration points. The material model for the oak impactor and oak frame was simplified as linear elastic with a Young's modulus of 10.4 GPa. Both the impactor and the frame consisted of solid elements with one integration point. The contact between the impactor and windshield, as well as the contact between the windshield and frame, were both modeled using the Mortar contact formulation.

Figure 2.15 shows the measured force-displacement curves from experiments in comparison to the simulation. Since the experiments were performed by prescribing the impactor displacement, we modeled the loading similarly in the simulations, using a prescribed displacement for the impactor. Accordingly, we ensured that the measured displacements were equal for the experiments and the simulations. The force levels were measured by a load cell on which the impactor was mounted in experiments. In the simulations, we defined the force level as the contact force between the windshield and impactor. We limited the numerical investigations to examine the pre-failure behavior in this study, therefore we stopped the force-displacement curves shorty after the maximum failure displacement for each test series.

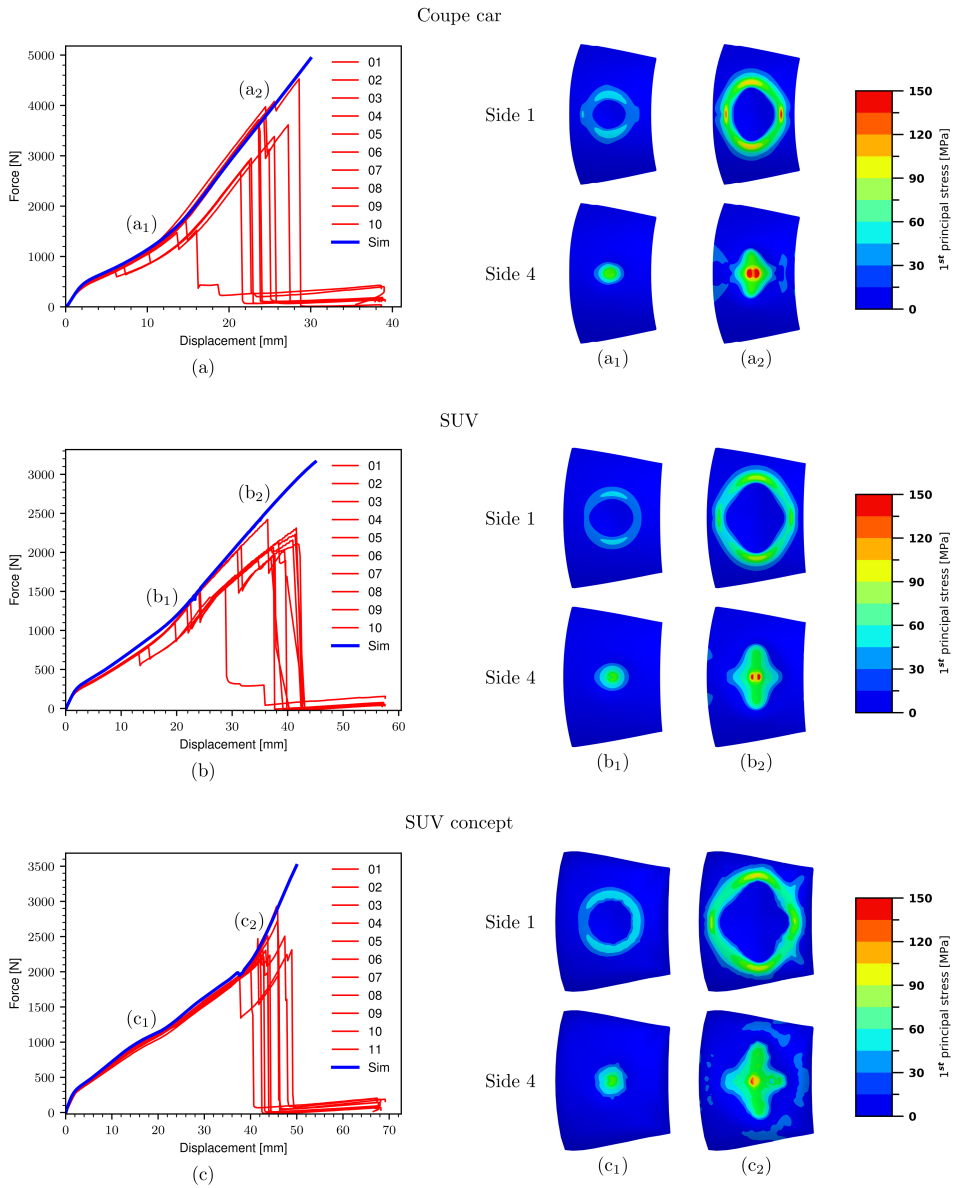Figure 2.15: Comparison of force-displacement curves from the numerical simulations and experiments for each of the windshield types (a, b, c). The major principal stress field for Side 1 (upper) and Side 4 (lower) of the windshield extracted at typical times of first fracture (a_1, a_2, b_1, b_2, c_1, c_2). Side 2 and Side 3 display similar stress fields as Side 4 and Side 1 respectively, but at lower magnitudes.

Figure 2.15 illustrates how the major principal stress field evolved during the simulation of the experiment. For each of the three test series, the stress field is displayed for Side 1 and Side 4 at an early and later stage during the experiment. The most intense areas of the Side 1 stress field displayed a circular form at an offset from the impactor early in the experiment and grew towards the boundaries to a more intense and elliptic shape. The most intense areas of the Side 4 stress field evolved from underneath the impactor and grew towards the boundaries forming petals with increased loading. These transformations in the stress field shapes stem from a combination of the windshield geometries and the influence from the boundary conditions. The Side 4 stress fields display higher peaks than those on Side 1.

The numerically estimated major principal stresses at failure are presented in Appendix A.1, see Tables A.1 to A.3. We estimated the failure stresses by using the experimental impactor displacement level at fracture combined with the fracture initiation location estimated from the high-speed camera footage. The coordinate system is the same as what is used in Figure 2.8 for the fracture initiation locations. When retrieving the major principal stress values, we chose the elements from glass layer 1 and 2, see Figure 2.2, that were closest to the measured fracture initiation location. We retrieved the stress at both layer surfaces. Based on the retrieved values, we can easily eliminate the sides with negative stress values as candidates for the side of the fracture origins. However, in most of the cases, we can not be certain of which side the fracture originated because the major principal stress values did not differ significantly. If we for instance consider test number 08 in the SUV test series, the retrieved major principal stress for Side 4 is 146.8 MPa, while it is 131.8 MPa for Side 2. To evaluate on which side the fracture initiated we need information about the surface flaws present in one or both of the sides. If there was only a surface flaw in one of the sides, then that side would be the critical one. Otherwise, if there were surface flaws on both sides, we would have to consider a combination of the stress level and surface flaw characteristics to decide on which side the fracture initiated. To simplify things, we assume that the fracture initiated on the side with the highest major principal stress value. With that assumption, we found that the major principal stress at fracture initiation varies from 38.8 MPa for test 01 to 178.6 MPa for test 09 in the SUV test series. Figure 2.16 displays the distribution of the estimated major principal stress values at first fracture for each of the windshield types and the test series performed by Brokmann et al. [66]. The SUV test series shows the greatest scatter, while the SUV concept exhibits the lowest scatter. The outlier in the SUV concept car distribution, indicated by a circle, is the fracture initiation for test 02, which was the strongest specimen for the windshield type.
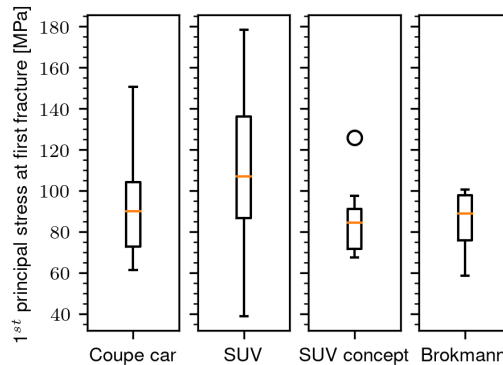
Figure 2.16: The estimated major principal stress distributions at first fracture for each of the windshield types and the test series performed by Brokmann et al. [66].

2.5 Discussion

All three windshield test series displayed a stochastic failure behavior, while maintaining a repeatable stiffness before failure, see Figure 2.8. This indicates that the experimental setup performs as designed. Additionally, the stochastic failure behavior underlines the importance surface flaws have on the performance of the windshield as a component.

From Figure 2.8 we also see that the fracture initiation locations of the coupe car were centered for both the first and second fracture. For the larger SUV windshields, the first fracture initiations were centered, while the initiations for the second fracture were located closer to the boundaries. For the largest SUV concept windshields, the fracture initiation locations were spread for both the first and second fracture. These trends may be related to size effects, where the larger windshields result in larger areas of approximately constant stress fields. These larger constant stress fields increase the probability of triggering unstable crack growth of microscopical surface flaws. The large constant stress field enables fracture initiation in a larger area, as seen in the largest SUV concept windshields. Figure 2.15 displays the simulated stress fields for the three test series at the typical time of first fracture. The highest magnitude of the stress fields for the coupe car and SUV are concentrated around the center. This is also true for the SUV concept car. However, we note that there is a large area of constant stress magnitude of a level similar to the stress level at fracture. This area is significantly larger for the SUV concept car then for the coupe car and SUV windshields. The stress fields support the claim that the experienced spread in fracture initiation locations is more likely for larger windshields.

The DIC data displayed in Figure 2.9 confirms that the experimental setup was symmetric about the YZ-plane at X equal to zero, see Figure 2.8 (d-f). This feature is valuable in terms of validation of repeatability, where we ensured that all test iterations had the same deformation history. Thus, we isolated features related to the stochastic fracture strength of glass.

Both the production stage windshields exhibited a clear two-stage failure behavior where fracture first initiated in one of the glass panes under the impactor, and then the other glass pane failed at a later stage away from the impactor. This behavior was not seen in the SUV concept windshield test series. For that particular test series both glass panes commonly failed in a closer temporal proximity, typically near the point of an increased stiffness were the convexly deformed part of the windshield hit the wooden frame. The difference in failure behavior may have two explanations:

1. The production methods differed, which lead to deviations between the CAD geometry and the hardware for the prototype stage SUV concept windshields. These deviations were not observed for the production stage coupe car and SUV windshields. The fact that the SUV concept windshields deformed all the way until the convexly deformed part of the windshield was in contact with the wooden frame may imply that the surface flaws were small or that the heat treatment introduced more compressive initial stresses. If we consider the major principal stress values at first fracture in Figure 2.16, the latter option is more likely.

2. The sizes of all three windshield types differ. The SUV concept windshield is the largest, which allows for more deformation before critical stress intensities are reached.

The crack propagation patterns vary based on the fracture initiation point. For fracture initiation points near the center of the windshield, we typically saw a radial crack pattern with a center in the initiation point. When fracture initiates near the boundaries, a circular crack pattern was seen. The severity of the crack propagation is closely linked to the strain energy stored in the windshield at the point of fracture. High energy fracture initiations result in large and dense crack patterns whereas low energy fracture initiations result in smaller and less dense crack patterns. If we compare the Side 1 stress fields for the coupe car in Figure 2.15 (a_1 and a_2) to the crack patterns in Figure 2.11, we see a clear similarity between the circular cracks and the intense circular shapes forming in the stress field. Thus, it is fair to assume that the intense circular shapes of the stress field are a contributing factor to the shape of the circular cracks. The visibility of the crack propagation was sensitive to the camera lighting conditions, making cracks oriented at an angle that reflected light into the camera lens visible. This camera lighting sensitivity made it difficult to capture the crack propagation within the entire component.

We found no correlations between the measured average crack speeds and the load level at fracture. However, we note that the cracks in a circular pattern typically propagated at higher average speed levels than the cracks that propagated in a radial pattern. This behavior may be caused by a higher level of stored strain energy in the areas of the circular crack propagation, resulting in more driving force for the crack growth. When comparing the crack propagation paths in Figure 2.13 with the stress fields in Figure 2.15, we see a clear correlation. For the Side 1 stress field we have circular shapes of nearly constant high magnitude stresses for all windshield types. These circular shapes overlap with the fastest crack propagation paths, and support the claim that these cracks were driven by the circular high magnitude strain energy fields. The highest Side 4 stress field magnitudes overlap with parts of the radial cracks. Due to the performance restrictions of the Photron high-speed camera located underneath the windshield in terms of filming frequency, we

were only able to capture fracture initiation locations and not crack propagation data underneath the impactor. For this reason, we only have partial crack propagation paths for the radial cracks. For the partial radial cracks we see lower average propagation speeds, which also could be linked to an decreasing amount of stored strain energy when the crack propagates away from the center location.

The numerical simulations captured the stiffness evolution of the experimental test series. The estimated major principal stress values at first fracture for the coupe car and SUV display a bigger scatter than what was seen for the SUV concept car and in the quasi-static windshield impact test series performed by Brokmann et al. [66]. This may be related to the variation in force level at fracture. For both the SUV concept test series and the test series performed by Brokmann et al. [66] we observe a smaller scatter in terms of force level at first fracture then for the coupe car and SUV test series. Interestingly, the difference in windshield geometry does not seem to affect the spatial distribution of the major principal stress at fracture. However, both the lowest and the highest critical stress values were located underneath the impactor. This is reasonable, since the area near the impactor is the most stress intensive area of the windshield throughout the experiment, making the probability of obtaining critical stress intensities higher than what is the case for the areas closer to the boundaries.

2.6 Conclusion

In this work, we presented a reliable method for conducting repeatable quasi-static tests on doubly curved windshields. Our approach considers the stochastic nature of glass and aims to gather crucial data for developing accurate numerical models. We collected impactor force and displacement data from the testing machine, target point displacements from 3D-DIC, and fracture initiation locations and crack propagation data from high-speed camera images. To estimate fracture initiation locations and crack propagation, we developed a Python-based post-processing tool that utilizes pose estimation to map image coordinates to spatial coordinates. We conducted tests on three windshield types: one from a coupe car (tested ten times), one from an SUV (tested ten times), and one from an SUV concept car (tested eleven times). Based on our study, we have drawn the following key conclusions:

- High-speed cameras are suitable for capturing the fracture initiations and crack propagations in windshields, but sensitive to lightning conditions.

- The windshield component strength seems to be size dependent.

- The crack propagation pattern exhibits a stochastic behavior.

- We found no correlation between the average crack speed and the load level at fracture.

- The average crack speed is higher for the circumferential cracks than for the radial cracks.

3 Glass Strength Prediction Model

This chapter is based on Paper II, "A physically based strength prediction model for glass". The chapter presents the implementation and validation of an improved version of the Glass Strength Prediction Model (GSPM) including the phenomenon of sub-critical crack growth (SCG), capable of handling rate effects. The new version of the GSPM is implemented as a material model in the commercial FE code LS-DYNA, triggering fracture initiation of the existing glass material model MAT_280.

3.1 Introduction

The strength of glass, which is a brittle amorphous material [5], has been a subject of great interest for a long time. Glass is popular due to its excellent transparent qualities, and is increasingly used in modern architecture and the automotive industry. Back in 1921, Griffith [15] proposed a connection between the fracture stress and the size of the microscopical surface flaws present on glass surfaces. Griffith formulated a fracture theory stating that for a flaw to become unstable, and fracture to initiate, the potential energy reduction that results from an increment of crack growth has to overcome the surface energy of the material. Griffith proved his theory by correctly predicting the relationship between the fracture strength and the flaw size in glass specimens. Irwin [16] built on Griffith's theory by introducing a measure of the potential energy available for a crack growth increment, called the of energy release rate, $\mathcal{G}$, given by

$$\mathcal{G} = -\frac{d\Pi}{dA} \tag{3.1}$$

where Π is the potential energy of an elastic body and dA is the crack growth area. Later, Irwin [17] introduced the stress intensity factor, which describes the stresses and displacements near the crack-tip by a single constant. Depending on the crack loading mode, the expressions for the stress intensity factor vary. In the field of fracture mechanics, it is common to divide the crack loading modes into three distinct modes, i.e., mode I, II and III [18]. In mode I loading, often referred to as the opening mode, the principal load is applied normal to the crack plane and tends to open the crack. Mode II corresponds to in-plane shear loading and tends to slide the crack faces with respect to each other. Mode III loading is an out-of-plane shear loading. The mentioned loading modes can be combined to describe all kinds of complex loading modes, often referred to as mixed-mode loading. For mode I loading, the stress intensity factor, K_I, is given by

$$K_I = Y(a, c, \phi)\,\sigma_n\sqrt{\pi a} \tag{3.2}$$

where Y is a geometrical crack shape factor which is dependent on the flaw depth, a, the flaw half-length, c, and the parametric angle, ϕ, while σ_n is the external applied stress normal to the crack.

The microscopical surface flaws present on the glass surface, typically referred to as Griffith flaws [19–23], reduce the fracture strength of glass by several orders of magnitude. In theory, without the surface flaws, the fracture strength of glass is in the order of 10 GPa [24, 25]. In practice the fracture strength is in the order of 100 MPa. Glass fracture initiates in the microscopical surface flaws which may grow under loading. If the stress intensity, K_I, is sufficiently high and above a threshold value, K_{th}, but lower than the critical stress intensity, K_{IC}, the flaw may grow sub-critically. This phenomenon is often called sub-critical crack growth (SCG), but also known as stress corrosion or static fatigue. The rate of the SCG is highly dependent on a combination of environmental factors, such as humidity and temperature, and the stress intensity [23, 26–33]. When the flaw grows sub-critically, the flaw depth, a, and the length $2c$, increase, resulting in an increased stress intensity.

At some point, with sufficient loading, the stress intensity will become critical, i.e., $K_I \geq K_{IC}$. At this point, the flaw exhibits unstable crack growth and failure is initiated. The resulting crack propagation is violent, with crack speeds reaching up to $\sim$1500–1600 m/s [34, 35]. Since the failure mechanism is governed by the microscopical surface flaws, glass exhibits a stochastic fracture behavior. The stochastic nature of glass fracture is rooted in the spatial distribution, size and shape of the microscopical surface flaws, which combined with the surface stress field determine the fracture strength. As the surface flaw characteristics differ for every glass specimen, many experimental iterations are needed to map the fracture strength distribution for one test case. This is both costly and impractical. Moreover, glass is becoming increasingly important as a load-bearing structural component in modern structures. In the automotive industry, large glass components such as windshields and sky roofs have a direct effect on the car performance in accidents or crashes. Without accurate numerical models that are able to capture the stochastic nature of glass, the typical option is to perform extensive testing. In other words, there is a pressing need for numerical models that can predict the structural strength of glass specimens.

There exist several models with the aim of predicting the fracture strength of glass. The load duration theory [109, 110] was presented by Brown in 1970, and was used to estimate the time-to-failure for loaded rectangular glass plates. In 1980, Beason [111, 112] proposed the glass failure prediction model, which aimed to predict the failure strength of glass plates independent on the plate aspect ratio, surface area and load duration. The glass failure prediction model was later incorporated in the glass thickness selection procedure in ASTM E 1300–94 [113–115]. Evans and Wiederhorn [116] presented a crack growth model for the lifetime prediction of ceramic components after proof testing based on empirical formulations. Fischer-Cripps and Collins [117] proposed a modified crack growth model. Overend et al. [118] proposed a general crack growth model, extending the modified crack growth model and compared the model performance to existing models. Later, Overend and Zammit [20] presented a computer algorithm for the general crack growth model. Common for all the above mentioned methods is a foundation based on SCG and fracture strength based on the Weibull probability distribution function (PDF) [119].

The presented models have been heavily discussed with respect to assumptions, usability and limitations [9, 39, 120, 121]. Haldimann [9] reviewed many glass design methods and proposed a more general model called the lifetime prediction model.

Yankelevsky [39] proposed a different approach for predicting the fracture strength of glass plates. The proposed model is based on the fact that the probabilistic fracture behavior of glass originates from varying surface flaw distributions, or flaw maps, of glass plates. To imitate this behavior, the model produces a set of virtual flaw maps with varying flaw shape, size and location. The fracture strength is found by combining the information from the flaw maps and linear elastic fracture mechanics (LEFM) theory. However, the model does not take SCG into account. Yankelevsky et al. [122, 123] validated the proposed strength prediction model to four-point bending experiments. Later, other models predicting failure in glass based on flaw maps have been proposed [40–42]. The model of Yankelevsky was further developed by Osnes et al. [14, 43] into a post-processor for finite element (FE) simulations.

The mentioned glass strength prediction models focus on finding the probability of failure, in terms of fracture initiation, and do not consider the post-failure stage. In extreme load cases, like real car crashes or the NCAP-evaluation tests [44], both the pre- and the post-failure stages need to be considered. Brokmann [33] developed a model based on SCG and initial flaw sizes estimated from fracture stresses fitted to a Weibull PDF. The model is integrated into an finite element (FE) code as a material model, making the model more user friendly. In this study, we propose a new Glass Strength Prediction Model (GSPM) that builds on the foundation laid by Yankelevsky [39] and Osnes et al. [14, 43], and aim to further develop and improve the GSPM by including SCG and propose a new way of representing the surface flaws. In addition, we incorporate the GSPM in a material model of an FE code, improving the usability and practicality of the model.

3.2   Glass Strength Prediction Model (GSPM)

In short, the GSPM combines linear elastic fracture mechanics (LEFM) and SCG in a Monte Carlo simulation to predict and potentially initiate failure in a virtual glass experiment performed in an FE simulation. The key feature of the GSPM is a generated representative sample of artificial flaw maps on the glass plate surfaces, which lays the foundation for the fracture strength predictions. The generated flaw maps each contain a number of flaws based on the selected flaw density, with a defined shape, depth, orientation and location. Based on the surrounding environment and loading history, the model keeps track of the predicted growth of each flaw originating from mode I loading and predicts when and where failure occurs for each flaw map in the generated representative sample. We neglect possible contributions from mode II and III loading.

The model implementation is based on an explicit FE framework, where glass plates are modeled using shell elements. To ensure generality and robustness, we implemented the model in a modular manner, facilitating integration and coupling with available damage models in FE solvers for future modeling of the post-failure behavior. Figure 3.1 presents the overall functionality of the GSPM, with model inputs and outputs. As inputs, the specimen geometry and stress history are retrieved from an FE simulation, while the flaw distribution and surrounding environment are

defined through the model input parameters.

Figure 3.1: The overall inputs and outputs of the GSPM. The model needs information about the specimen geometry, stress history, flaw distribution and the surrounding environment, and predicts the fracture distribution in terms of fracture time, location and stress.

3.2.1   Versions

The GSPM is implemented in two different versions, one material model version suited for coupling with available damage models existing in e.g., commercial FE solvers and one external post-processing version, aimed at different applications. The two versions are described below.

Material model version
The material model version of the GSPM is implemented in Fortran and suitable for coupling with damage models in FE codes. By integrating the model directly with an FE solver, the model can calculate the failure distribution during the FE simulation and work as a trigger for damage initiation. The model is designed to facilitate easy coupling with existing damage models for glass, allowing flexible customization of glass material modeling. In the material model version, the model extracts stress history and geometry data directly from the FE simulation.

The purpose of the material model version of the GSPM is to allow the user to take the stochastic nature of glass into account during FE simulations without the need to run multiple simulations. During the FE simulation, the GSPM generates a failure distribution based on the representative sample of artificial flaw maps, naturally sorted from weakest to strongest. With this property, the user can select which flaw map to use to initiate failure, and thus the strength of the glass specimen. The model predicts a scatter in the fracture initiation location and time up until triggered failure initiation, which provides an idea of the repeatability of the studied case. A small scatter implies a repeatable strength for the given load case and geometry in question. The predicted fracture initiation can be used to trigger damage models at a physically based time and location. This flexible way of including the stochastic nature of failure initiation in numerical simulations of glass plates makes it applicable in numerous design applications.

Post-processing model version
The post-processing version of the GSPM is implemented in two programming languages, Fortran and Python. The Fortran implementation is compiled and thus faster than the Python implementation. On the other hand, the Python implementation is more portable to use and integrate in other Python-based scripts. To make strength predictions, the model uses stress history and geometry data exported from an FE simulation in which the glass has purely elastic behavior. Depending on the desired temporal prediction accuracy, the user provides a sufficient amount of

stress field increments from the FE simulation.

The post-processing version of the GSPM is implemented as an independent program. Given the stress history from a damage free FE simulation as input, the version outputs a complete fracture strength distribution of the first fracture initiation. The post-processing version facilitates calibration and sensitivity analysis of the input parameters. By coupling the resulting probability distribution of the fracture strength with corresponding experimental data, the user may find suitable flaw map parameters for their glass plate specimens. The decoupling from the FE simulation makes the post-processing version significantly faster than the material model version as the complete stress history is already available. The computational speedup achieved from the decoupling makes the version favorable in cases where some input parameters are uncertain and calibration is needed or only the first fracture initiation is of interest.

3.2.2 Flaw generation and distribution

To represent the flaw distribution found on the surfaces of a glass plate specimen, we have based the flaw generation procedure on the float glass production line. In a typical float glass production line, glass melt is poured onto a large tin bath, forming a so-called jumbo glass plate, with typical dimensions of $3.12\,\text{m} \times 6\,\text{m}$ [9]. During the solidification of the glass melt, small microscopical flaws, invisible to the naked eye, are created on the glass surface. A consequence of the production process is that the two glass plate surfaces are not identical. The tin side has been found to be marginally weaker that the air side [9, 124]. However, as a simplification, both glass surfaces are assumed to have equal flaw distributions. After solidification and cooling, the jumbo glass plate is cut into smaller glass specimens. In the GSPM, this process is emulated by first creating a jumbo glass plate of a user specified area, A_{jumbo}. Second, we generate N_0 flaws on each of the jumbo glass plate surfaces based on shape, size, and orientation distributions. Third, we cut the jumbo glass plate into smaller glass specimens of areas $A_{specimen}$, as illustrated in Figure 3.2. The parameters governing the flaw distribution are presented in Table 3.1 (parameters 1–3). The number of virtual jumbo glass plate flaw maps, M_{jumbo}, is given by

$$M_{jumbo} = \left\lceil M_{it} \frac{A_{specimen}}{A_{jumbo}} \right\rceil \tag{3.3}$$

where $\lceil x \rceil$ is the ceiling function and M_{it} is the number of glass specimen flaw map iterations. The number of flaws per jumbo glass plate, N_0, is given by

$$N_0 = \rho_{flaw} A_{jumbo} \tag{3.4}$$

where ρ_{flaw} is the surface flaw density.

We assume that the flaws are non-interacting and uniformly distributed over the glass surface. In addition, we assume that the distance between the flaws is much larger than the dimensions of single flaws. To fulfill the assumptions that the flaws are uniformly distributed on the glass surfaces, we draw the location of each flaw based on a unique random selection of the elements hosting flaws of the glass plate mesh from the FE simulation. In other words, for each virtual flaw

map on the glass plate surfaces, we perform a random selection of elements that contain a flaw. The random selection is done using Floyd's algorithm for sampling without replacement [125]. By assuming that the element size is uniform, the drawn positions are distributed uniformly on the glass surface.
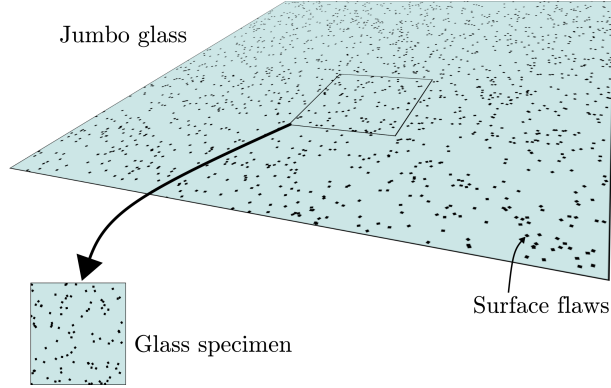

Figure 3.2: Illustration of the flaw generation and distribution procedure in the GSPM.

Flaw depth

Similar to Yankelevsky [39], we assume that there is a single flaw of the largest depth in the jumbo glass plate, and an increasing number of flaws for decreasing flaw depths. The depth distribution is presented in Figure 3.3 and given by

$$\frac{N_i}{N_0} = \exp\left(-\frac{a_i - a_{\min}}{\eta}\right) \tag{3.5}$$

where a_i is the depth of flaw i, $a_{\min}$ is the minimum flaw depth of the flaw distribution, N_0 is the total number of flaws on the jumbo glass plate surface, N_i is the number of flaws that have depths larger or equal to a_i, and η is a distribution parameter given by

$$\eta = \frac{a_{\max} - a_{\min}}{\ln(N_0)} \tag{3.6}$$

where $a_{\max}$ is the maximum flaw depth of the flaw distribution. The flaw depth distribution in Equation (3.5) is generated by isolating a_i, resulting in

$$a_i = \eta\left(\ln(N_0) - \ln(N_i)\right) + a_{\min} \tag{3.7}$$

where N_i is given by

$$N_i = (N_0 - 1)\, x_i + 1, \quad x_i \sim U\left([0, 1]\right) \tag{3.8}$$

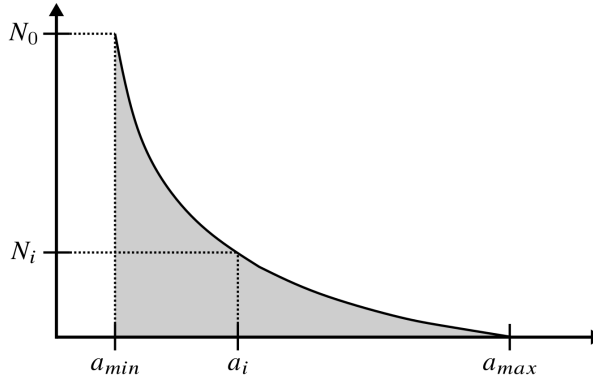where x_i is drawn N_0 times from a uniform distribution.

Figure 3.3: The assumed flaw depth distribution, where $a_{\min}$ is the minimum and $a_{\max}$ is the maximum flaw depth, N_0 is the total number of flaws on the jumbo glass plate surface, a_i is the depth of flaw i and N_i is the number of flaws that have depths larger or equal to a_i.

Flaw shape

To calculate the stress intensity factor for mode I loading, K_I, at each flaw on the glass surface, we need information about the shape and orientation of the flaw. In the GSPM, all flaws are idealized as semi-elliptic, see Figure 3.4, although in reality they may be shaped differently. To allow for depth (a) and length ($2c$) variations within the assumed semi-elliptic shape, we model the depth-to-half-length ratio, a/c, distribution with a generic two-sided truncated normal distribution [126]. The PDF for the truncated normal distribution, f_t, is given in by

$$f_t\,(x;\mu,\sigma,a,b) = \frac{1}{\sigma}\,\frac{f_n\left(\frac{x-\mu}{\sigma}\right)}{F_n\left(\frac{b-\mu}{\sigma}\right) - F_n\left(\frac{a-\mu}{\sigma}\right)} \tag{3.9}$$

where x is the stochastic variable, μ is the mean value, σ is the standard deviation, a and b are the minimum and maximum value of x, f_n is the PDF and F_n is the cumulative distribution function (CDF) of the standard normal distribution. The half-length of flaw i is given by

$$c_i = \frac{a_i}{(a/c)_i} \tag{3.10}$$

where $(a/c)_i$ is the depth-to-half-length ratio for flaw i drawn from the two-sided truncated normal distribution. The input parameters presented in Table 3.1 (parameters 4–9) govern the generated flaw shape distributions.
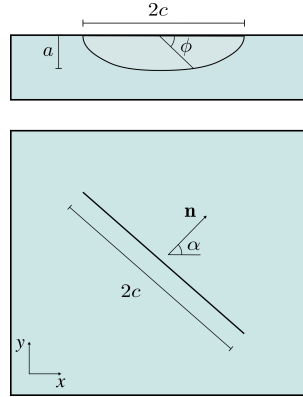
Figure 3.4: The assumed semi-elliptic flaw shape where a is the depth, c is the half-length, ϕ is the parametric angle of the ellipse and α is the in-plane angle between the flaw normal vector, **n**, and the x-axis, defining the orientation of the flaw.

Flaw orientation

We assume that the surface flaws do not favor any orientation. Consequently, every individual flaw is given an orientation through a random angle α, see Figure 3.4, between 0 and π, defining the in-plane angle between the flaw normal vector, **n**, and the x-axis. The external applied stress normal to a flaw, denoted σ_n, is given by

$$\sigma_n = \frac{\sigma_x + \sigma_y}{2} + \frac{\sigma_x - \sigma_y}{2} \cos\left(2\alpha\right) + \tau_{xy} \sin\left(2\alpha\right) \tag{3.11}$$

where σ_x and σ_y are the in-plane normal stresses in the x and y direction, respectively, and τ_{xy} is the in-plane shear stress.

3.2.3 Sub-critical crack growth (SCG)

Glass surface flaws are known to grow sub-critically under certain conditions. The crack growth speed of the surface flaws can be divided into four regions dependent on the stress intensity for mode I loading, K_I [23, 31–33]. The regions are presented in Figure 3.5 with the following description of the different regions:

1. $K_I < K_{th}$. No crack growth in this region.

2. $K_{th} < K_I < K_{I,2}$. Crack growth is driven by a combination of stress state and humidity. The crack growth speed in this region can be described using a power law:

$$v = \frac{\mathrm{d}a}{\mathrm{d}t} = v_0 \left(\frac{K_I}{K_{IC}}\right)^n \tag{3.12}$$

3. $K_{I,2} < K_I < K_{IC}$. Crack growth speed is almost independent of the stress intensity.

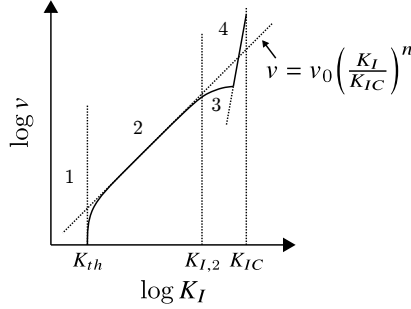4. $K_I > K_{IC}$. The crack growth becomes unstable.

Figure 3.5: The relationship between crack growth speed, v, and stress intensity for mode I loading, K_I.

In Figure 3.5, K_I is the mode I stress intensity, K_{th} is the stress intensity threshold for SCG, $K_{I,2}$ is the stress intensity at the transition between region 2 and 3 and K_{IC} is the critical stress intensity. In the GSPM, the SCG is modeled to follow a linearized version of the evolution in Figure 3.5, marked with dotted lines, where the crack grows sub-critically for stress intensities between K_{th} and K_{IC}. The calculation of the geometric factor in Equation (3.2), Y, and the SCG is done using the empirical equations for tension from Newman and Raju [127], given by

$$K_I = \sigma_n \sqrt{\pi \frac{a}{Q\,(a,c)}} F\,(a,c,\phi) = Y\,(a,c,\phi)\,\sigma_n \sqrt{\pi a} \tag{3.13}$$

$$Y\,(a,c,\phi) = \frac{F\,(a,c,\phi)}{\sqrt{Q\,(a,c)}} \tag{3.14}$$

where $0 < a/c \leq 1$, $0 \leq \phi \leq \pi$, F is the stress-intensity boundary-correction factor and Q is the shape factor for an elliptic crack. The sub-critical growth of the flaw depth is calculated by integrating Equation (3.12) with $\phi = \pi/2$ using the forward-Euler method. The same calculation is done for the half-length, however, with $\phi = 0$. The input parameters influencing the SCG behavior are presented in Table 3.1 (parameters 10–13). The stress intensity threshold, K_{th}, and the critical stress intensity, K_{IC}, define the region for SCG. The SCG rate is governed by the terminal crack growth speed, v_0, and the exponent, n. These parameters vary dependent on the surrounding cracking environment.

3.2.4 Procedure

The strength prediction procedure of the GSPM is presented schematically in Figures 3.6 and 3.7. Below follows a step-wise walk-through of the procedure:

1. At the start of the simulation, we generate and distribute flaw maps for M_{it} unique artificial glass plate specimens, see Figure 3.6. These flaw maps serve as a representative sample for glass plate specimens of the same kind.

2. We enter a prediction loop, see Figure 3.7, where the presented procedure is repeated for each stress frame until the failure criterion is met:

   (a) Calculate the current time step based on the simulation time step and potential time scaling, retrieve the current stress field and initiate the flaw map counter, $m = 1$.

   (b) Apply surface flaw map m to the current stress field.

   (c-e) Loop through every flaw in the intact artificial glass samples, calculate the stress intensity for mode I loading, K_I, and perform one of the following actions:

   - $K_I < K_{th}$
     The flaw remains unchanged.

   - $K_{th} < K_I < K_{IC}$
     The flaw grows sub-critically. We update the flaw depth and length based on SCG theory.

   - $K_I > K_{IC}$
     The flaw grows over-critically and at this point we predict that failure has occurred for the artificial glass sample. We save the failure information and remove the glass sample from the collection of intact samples. If multiple flaws are critical at the same time step, the flaw failing first is considered the most critical, which is decided based on the linearly approximated time at failure, t_f, given by

   $$t_f = t_{i-1} + \frac{K_{IC} - K_{I,i-1}}{K_{I,i} - K_{I,i-1}} (t_i - t_{i-1}) \tag{3.15}$$

   where the indices $i - 1$ and i represent the previous and current time step.

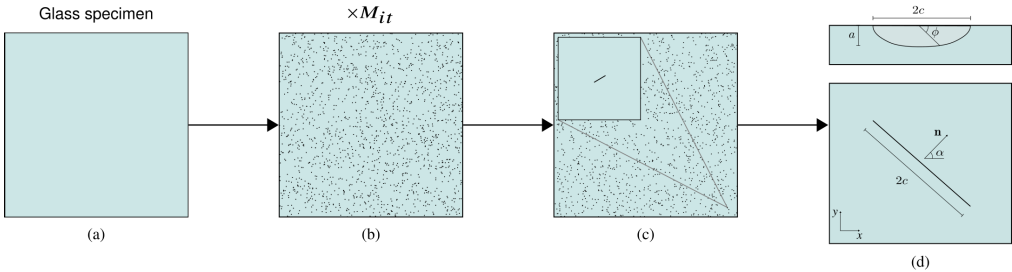   If $m < M_{it}$, increment the flaw map counter and go to (b), else, finish time step.

Figure 3.6: Illustration of flaw map generation: start with the glass specimen geometry (a) and generate M_{it} flaw maps (b) where each flaw has a depth, a, length, $2c$ and orientation, α, (c-d).
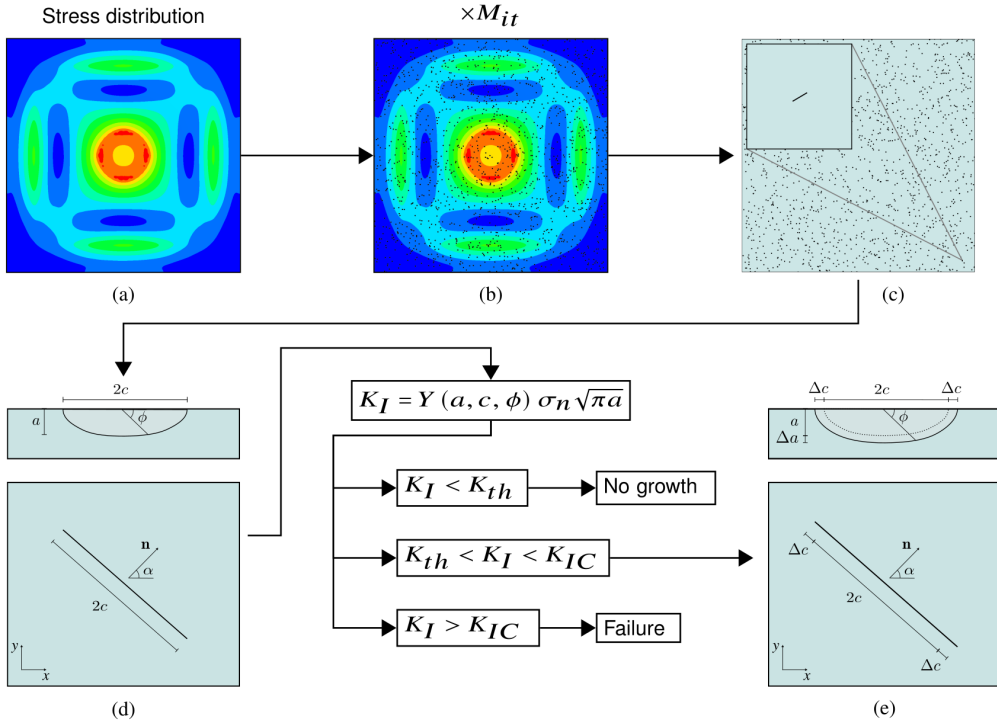
Figure 3.7: Schematic illustration of the prediction loop for a stress frame: starting with the stress distribution (a), each of the M_{it} virtual flaw maps are mapped onto the stress distribution (b), where each flaw is investigated for potential SCG or failure (c-e).

3.2.5 Other

To account for time scaling and noise in the numerical simulations, we have included options for scaling the time step and to exponentially average the stress intensity factor in the following manner

$$\bar{K}_{I,i} = \alpha_{\exp} K_{I,i} + \left(1 - \alpha_{\exp}\right) \bar{K}_{I,i-1} \tag{3.16}$$

where $\bar{K}_{I,i}$ and $\bar{K}_{I,i-1}$ are the average stress intensity factors for the current and previous time step, respectively, $K_{I,i}$ is the stress intensity factor for the current time step and $\alpha_{\exp}$ is the exponent for the moving exponential averaging. The GSPM input parameters in Equation (3.16) are listed in Table 3.1 (parameters 14–15).

3.2.6 Material model

The material model version of the GSPM includes two additional input parameters, presented in Table 3.1 (parameters 16–17). In this version, the GSPM can be used to trigger other damage models used to describe crack propagation at fracture initiation for a user-defined glass fracture strength. The glass strength is set using the parameter P_f, which is the percentile value of the

fracture strength distribution where failure is initiated, defined by

$$P_f = P\left(t \leq t_f\right), \quad 0 \leq P_f \leq 1 \tag{3.17}$$

where P is the probability function and t_f is the time at failure. By selecting a glass strength using the failure percentile parameter, P_f, the glass plates included in the model will initiate failure at a time and location representative for the selected strength. Figure 3.8 illustrates the difference in workflow between the material model and the post-processing version. Explicit FE simulations usually involve many increments. For this reason, we added an option to control the GSPM update frequency using the parameter n_{inc}, an option which allows the user to reduce the computational time. The parameter must be used with caution, since it affects the accuracy of the prediction. The choice of the parameter value is dependent on the particular load case.
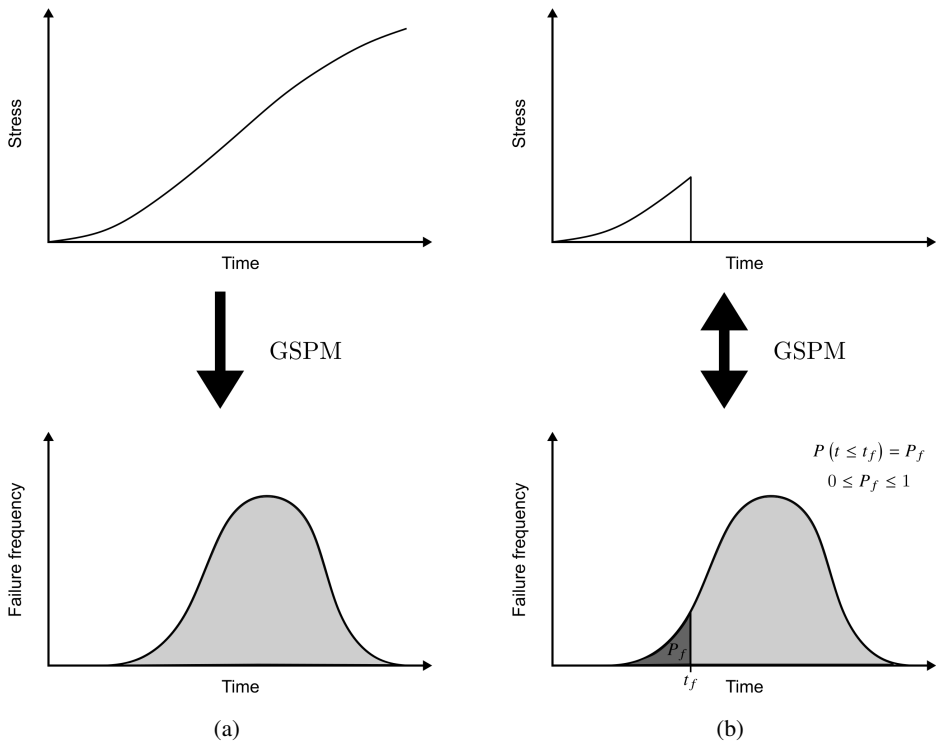

Figure 3.8: Illustration of the workflow of the post-processing version (a) and material model (b). For the post-processing version (a), GSPM outputs a failure distribution based on the exported stress history of a damage free FE simulation. For the material model version (b), GSPM calculates the failure distribution during the FE simulation and triggers failure when the user specified failure percentile is reached.

Table 3.1: The GSPM input parameters related to the flaw distribution (1–3), flaw shape (4–9) and SCG (10–13). Time scaling and noise handling parameters (14–15) and material model version parameters (16–17) are also presented.

Number	Symbol	Description	Unit
1	M_{it}	Number of glass specimen flaw map iterations	[-]
2	A_{jumbo}	Area of a jumbo glass plate	[m^2]
3	ρ_{flaw}	Flaw density	[flaw/cm^2]
4	$a_{\min}$	Minimum flaw depth	[µm]
5	$a_{\max}$	Maximum flaw depth	[µm]
6	$(a/c)_{mean}$	Flaw depth-to-half-length ratio, mean value	[-]
7	$(a/c)_{std}$	Flaw depth-to half-length ratio, standard deviation	[-]
8	$(a/c)_{\min}$	Flaw depth-to-half-length ratio, minimum value	[-]
9	$(a/c)_{\max}$	Flaw depth-to-half-length ratio, maximum value	[-]
10	K_{IC}	Critical stress intensity	[MPa$\sqrt{mm}$]
11	K_{th}	Stress intensity threshold for SCG	[MPa$\sqrt{mm}$]
12	v_0	Terminal SCG speed	[mm/s]
13	n	SCG exponent	[-]
14	t_{scale}	Time scaling factor	[-]
15	$\alpha_{\exp}$	Exponent for moving exponential averaging	[-]
16	n_{inc}	Number of increments to skip per GSPM increment	[-]
17	P_f	Failure percentile	[-]

3.3 Calibration

For calibration of GSPM input parameters, we apply the post-processing version of the GSPM. The version contains 13 input parameters governing the glass specimen flaw distribution and SCG behavior, see Table 3.1 (parameter 1–13). These parameters may vary depending on factors such as the chemical composition, the production method of the glass and the surrounding environment. For this reason, there does not exist a universal set of parameters. To facilitate calibration of the GSPM input parameters, we present a generic and robust methodology for calibration based on experimental test series on glass. In addition, we perform sensitivity studies for different load cases and discuss how the different input parameters affect the glass specimen strength.

3.3.1 Calibration procedure

Since the output of the GSPM is a fracture strength distribution, we have to apply a statistical methodology to verify the prediction accuracy. As an overall goal, we want to find input parameters that result in accurate strength predictions for a variety of loading conditions. Here, we propose an optimization routine that is based on comparing the time at failure of the experimental test series to GSPM predictions using the Kolmogorov-Smirnov test for goodness of fit [128]. The Kolmogorov-Smirnov test for goodness of fit is a non-parametric test of the equality of two samples.

The Kolmogorov-Smirnov statistic, K, reflects the normalized measured distance between the sample distributions, resulting in an equality score spanning from 0 to 1 where the sample distributions are identical for $K = 0$ and there is no similarity between them for $K = 1$.

The proposed calibration procedure is iterative, where each iteration follows the steps below, illustrated in Figure 3.9:

1. Specify a set of input parameters, $\mathbf{x}$, and run the GSPM post-processing model on the simulated experiments, see Figure 3.9 (a)

2. Calculate an equality score, K, based on the GSPM predictions and the experimental data, see Figure 3.9 (b), using a non-parametric Kolmogorov-Smirnov test for goodness of fit, see Figure 3.9 (c)
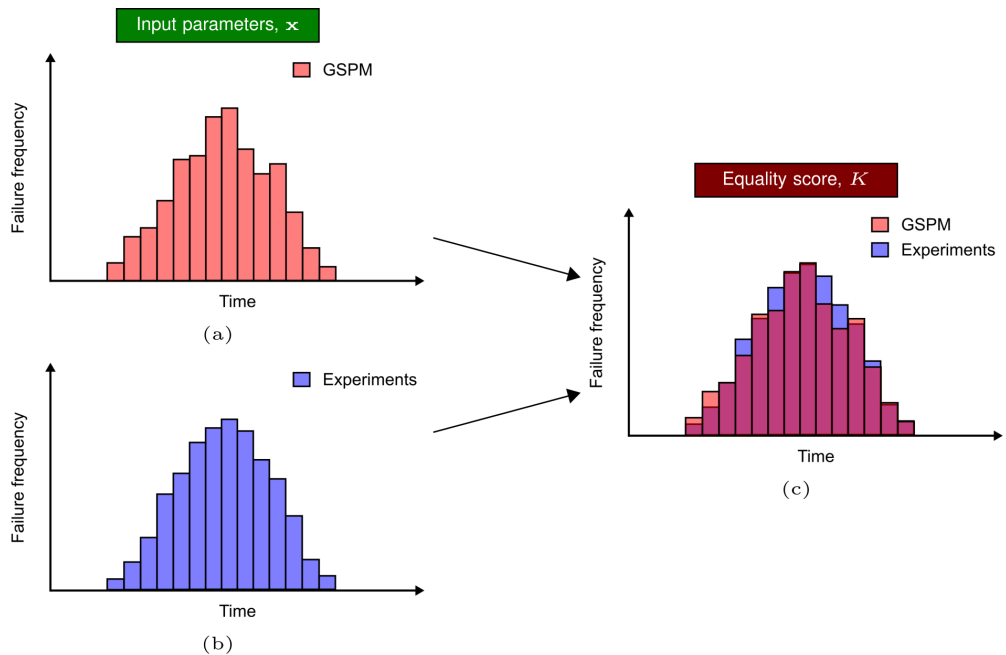

Figure 3.9: Illustration of an iteration for one test series in the proposed calibration procedure for GSPM. From a set of input parameters, $\mathbf{x}$, GSPM predicts a strength distribution (a) which is evaluated against the experimental strength (b), resulting in a equality score, K, (c). In this example, K would be close to zero.

Based on the calibration iteration steps presented in Figure 3.9, we may express the equality score, $K = K(\mathbf{x})$, as a function of the model input parameters, $\mathbf{x}$. The overall goal with the model calibration is to find a set of parameters that results in the best possible match with the experimental data. In other words, we want to minimize the sum of the equality scores, K. The

minimization problem is defined by

$$\underset{\mathbf{x}}{\text{minimize}} \quad \sum_{n=1}^{N_e} w_n \cdot K_n \left(\mathbf{x} \right) \tag{3.18}$$

subject to:

$$\min x_j \leq x_j \leq \max x_j \quad \forall j = 1, \ldots, N_p$$

where N_e is the number of experimental test series, w_n is the weighting and K_n is the equality score of the experimental test series n, $\mathbf{x}$ is the set of N_p input parameters to be calibrated and x_j is the jth input parameter. The procedure is implemented in Python and coupled to the SciPy optimization library [129].

3.3.2 Calibration examples

To calibrate the model for a variety of load cases, we made use of the experimental work on monolithic glass plates performed by Osnes et al. [14, 130], Rudshaug and Evensen [131] and Harneshaug and Ose [132]. We refer to the referenced sources for presentation of the experimental work and FE modeling details. The experimental work stems from glass plates from two glass suppliers. From supplier 1, we have quasi-static four-point bending tests of three specimen sizes, low-velocity impact tests of four different impact velocities, blast loading tests for three different blast pressures and quasi-static water pressure tests. From supplier 2, we have a large number of quasi-static punch tests for three loading rates. The test series are summarized in Table 3.2 for supplier 1 and Table 3.3 for supplier 2.

Table 3.2: Experimental test series used in the calibration process for glass plates from glass supplier 1.

Load case	Test series name	Number of tests
Quasi-static four-point bending [130]	Small	20
	Medium	21
	Large	30
Low-velocity impact [130, 132]	2.3 m/s	1
	2.4 m/s	3
	4.1 m/s	1
	4.2 m/s	3
Blast loading [130]	~50 kPa	2
	~60 kPa	8
	~70 kPa	2
Quasi-static water pressure [130]	—	11

Table 3.3: Experimental test series used in the calibration process for glass plates from glass supplier 2.

Load case	Test series name	Number of tests
Quasi-static punch [14, 131]	3 mm/min	30
	100 mm/min	30
	300 mm/min	30

All the test series in Tables 3.2 and 3.3 were modeled numerically using FE analysis with a damage-free linear elastic representation of the glass plates. Before applying the GSPM, we ensured that the stiffness response of each FE model matched the experimental test series before fracture. This is important to ensure that the simulated stress histories used by the GSPM were accurate. As shown in Table 3.1, the model has a high number of input parameters. Depending on the load case, geometry and resulting stress field evolution, the effect of the different parameters may vary. In these calibration examples, we made the following choices:

- We fixed the number of flaw map iterations, M_{it}, to 5000.

- The jumbo glass dimensions are set to $3.21\,\text{m} \times 6\,\text{m}$, resulting in a jumbo glass area, A_{jumbo}, of $19.2\,\text{m}^2$.

- All cracks have a constant depth-to-half-length ratio (a/c), reducing the four shape related input parameters $((a/c)_{mean}, (a/c)_{std}, (a/c)_{\min}$ and $(a/c)_{\max})$ to only one parameter.

- The critical stress intensity, K_{IC}, is fixed to $23.7\,\text{MPa}\sqrt{\text{mm}}$ [14, 43].

As a result, the following group of input parameters, $\mathbf{x}$, must be calibrated: ρ_{flaw}, $a_{\min}$, $a_{\max}$, a/c, K_{th}, v_0 and n. The results of the calibrations are presented in Figures 3.10 and 3.11 with corresponding calibrated input parameters in Tables 3.4 and 3.5 for the supplier 1 and 2 experiments, respectively. From both Figures 3.10 and 3.11 we find that the GSPM is able to accurately reproduce the experimental behavior for all load cases, spanning from quasi-static to rapid loading rates and from local to global loading scenarios. We note that the equality score, K, is high for the test series with few experimental iterations, which is natural due to the small amount of data points. The calibrated input parameters imply that the glass plates from supplier 2 are of higher quality than the plates from supplier 1 based on the calibrated maximum flaw depth, $a_{\max}$. It is worth noting that the predicted percentage of failed plates in the blast load cases were $3.76\,\%$, $19.94\,\%$ and $53.18\,\%$ for incident pressures of $\sim 50\,\text{kPa}$, $\sim 60\,\text{kPa}$ and $\sim 70\,\text{kPa}$, respectively. In other words, the majority of the virtual glass plated did not fail for the two lowest incident pressures. For the other load cases, all the virtual glass plates failed.

Table 3.4: The resulting calibrated input parameters for the glass plates from supplier 1.

ρ_{flaw} [flaws/cm^2]	$a_{\min}$ [µm]	$a_{\max}$ [µm]	(a/c) [-]	K_{th} [MPa$\sqrt{\text{mm}}$]	v_0 [mm/s]	n [-]
0.5	0.1	25	0.2	5.0	1	15

Table 3.5: The resulting calibrated input parameters for the glass plates from supplier 2.

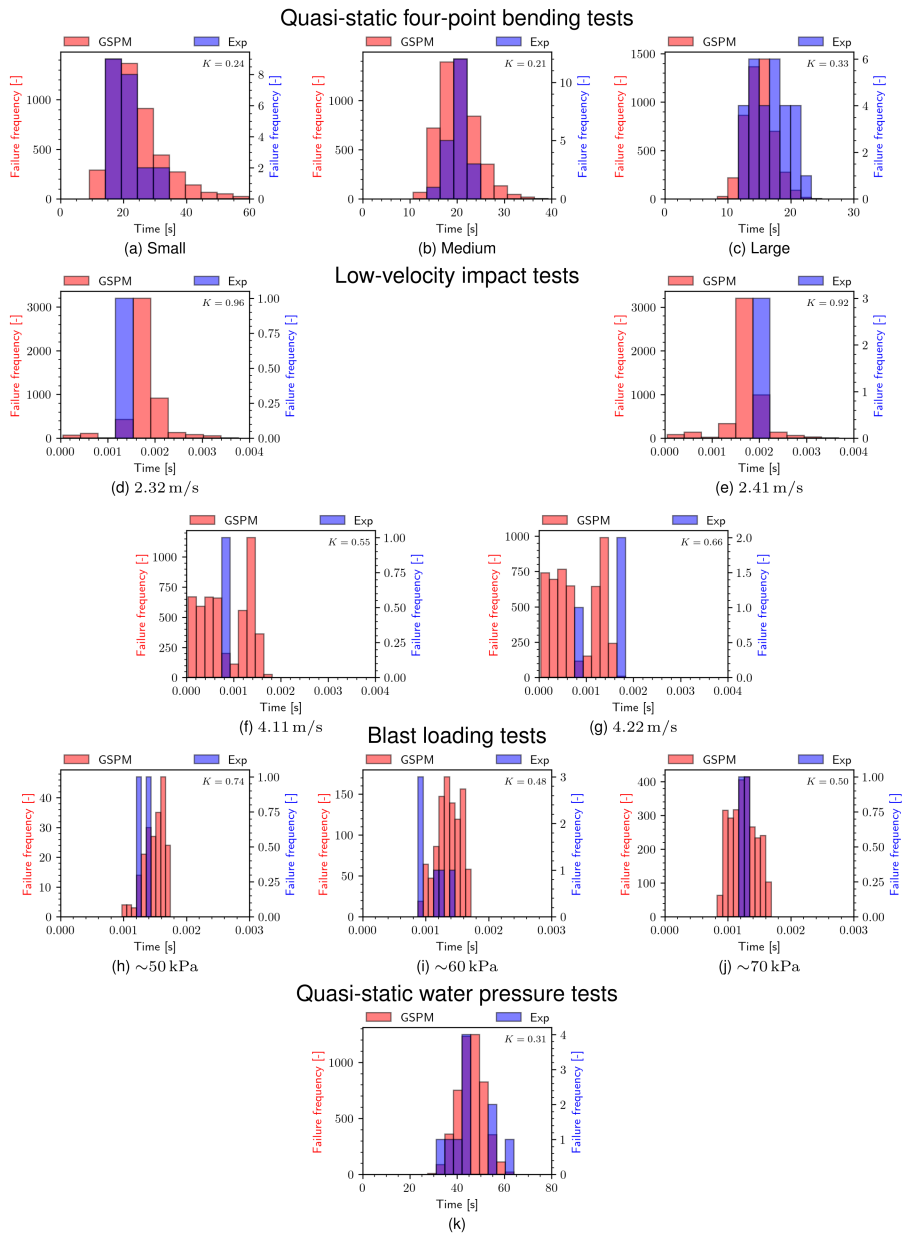| ρ_{flaw} [flaws/cm^2]	$a_{\min}$ [µm]	$a_{\max}$ [µm]	(a/c) [-]	K_{th} [MPa$\sqrt{\text{mm}}$]	v_0 [mm/s]	n [-]
0.5	0.1	15	1.0	5.0	1	20

Figure 3.10: Results of the GSPM calibration for the glass plates from supplier 1. The resulting GSPM predictions (in red) compared to the experimental strength results (in blue) are presented for the quasi-static four-point bending (a-c), low-velocity impact (d-g), blast loading (h-j) and quasi-static water pressure (k) test series. The equality score, K, is presented in the upper right corner for each test series.
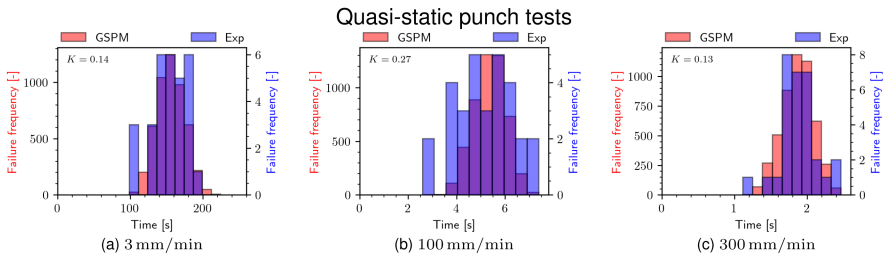
Figure 3.11: Results of the GSPM calibration for the glass plates from supplier 2. The resulting GSPM predictions (in red) compared to the experimental strength results (in blue) are presented for the quasi-static punch (a-c) test series. The equality score, K, is presented in the upper left corner for each test series.

3.3.3 Parameter sensitivity

We performed an extensive full factorial design sensitivity study for the calibrated input parameters, running GSPM strength predictions for 864 input parameter combinations per test series. Figures 3.12 to 3.14 present the resulting interaction plots from the full factorial design sensitivity study for the quasi-static four-point bending test series with the large specimen, the low-velocity impact test series at an impact velocity of 4.2 m/s and the quasi-static water pressure test series. The interaction plots clearly show that the flaw depth-to-half-length ratio, a/c, affects the glass strength, where the parameter value is positively correlated to the predicted time at failure for all the presented interaction plots. The effect of the minimum flaw depth, a_{min}, seems to be negligible, but the maximum flaw depth, a_{max}, has a real impact. The maximum flaw depth is negatively correlated to the predicted time at failure, in contrast to the flaw depth-to-half-length ratio, a/c. When we study the effect of the flaw density, ρ_{flaw}, it is evident that it has the greatest effect on the low-velocity impact loading case, while it has a lower effect on the quasi-static four-point bending. We find no effect on the quasi-static water pressure tests when we vary the flaw density. The SCG parameters, namely the terminal crack growth speed, v_0, and the SCG exponent, n, only seem to affect the quasi-static four-point bending and water pressure test cases, where the terminal crack growth speed is slightly negatively correlated, while the SCG exponent is slightly positively correlated. The stress intensity threshold for SCG, K_{th}, does not seem to exhibit any effect on the strength predictions for the studied cases.
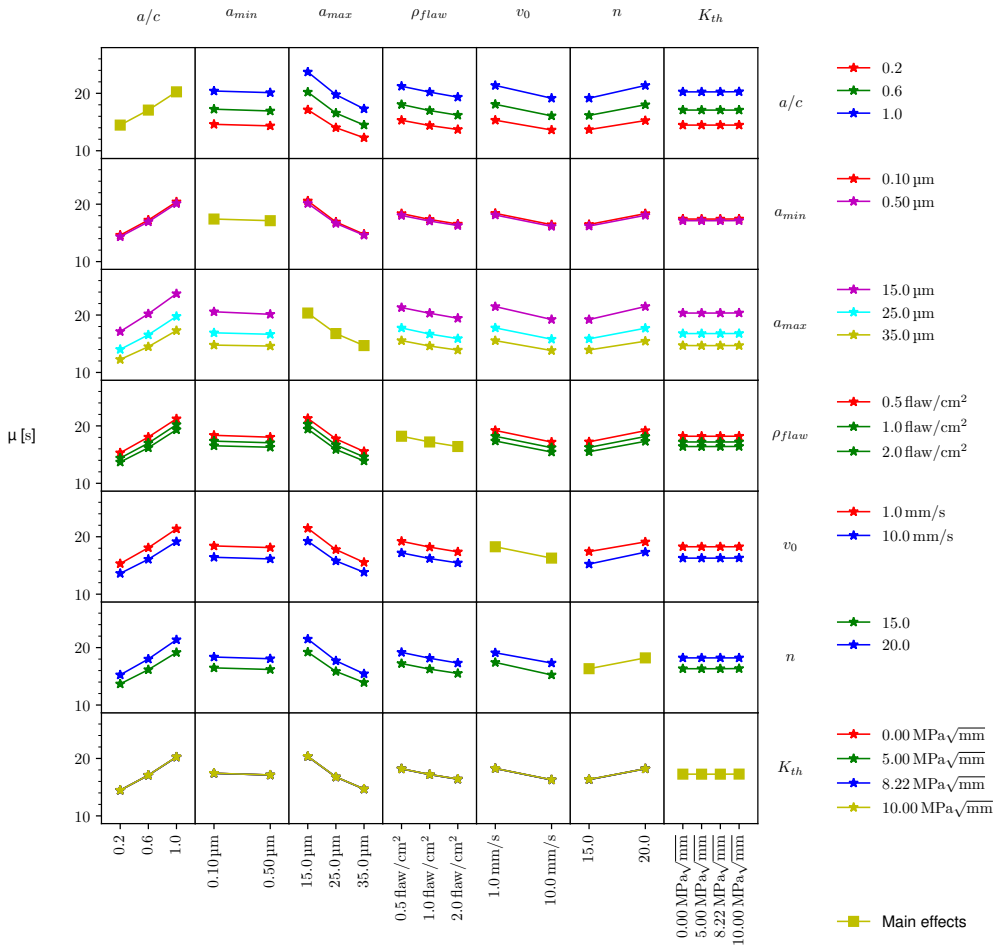
Figure 3.12: Sensitivity analysis in form of a full factorial design interaction plot of the GSPM input parameters for the quasi-static four-point bending test series with the large specimens. The comparison index, μ, is the time at failure.
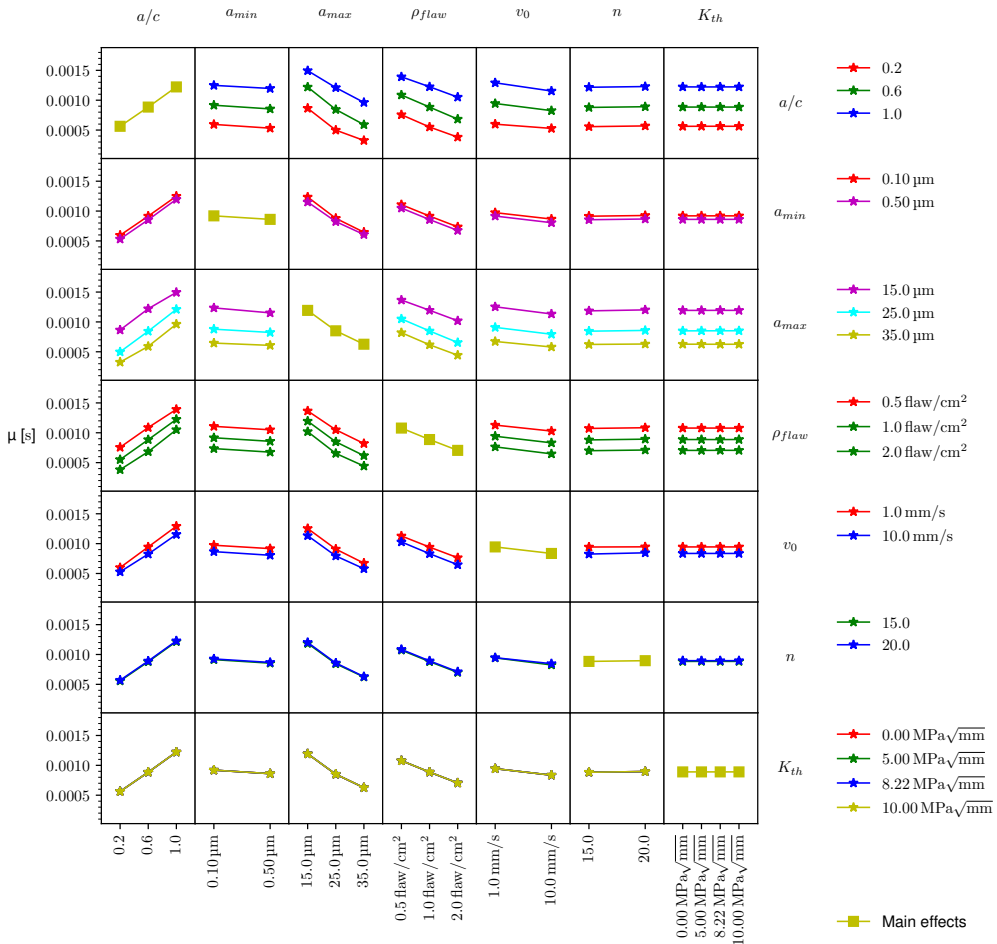
Figure 3.13: Sensitivity analysis in form of a full factorial design interaction plot of the GSPM input parameters for the low-velocity impact test series with an impact velocity of 4.2 m/s. The comparison index, µ, is the time at failure.
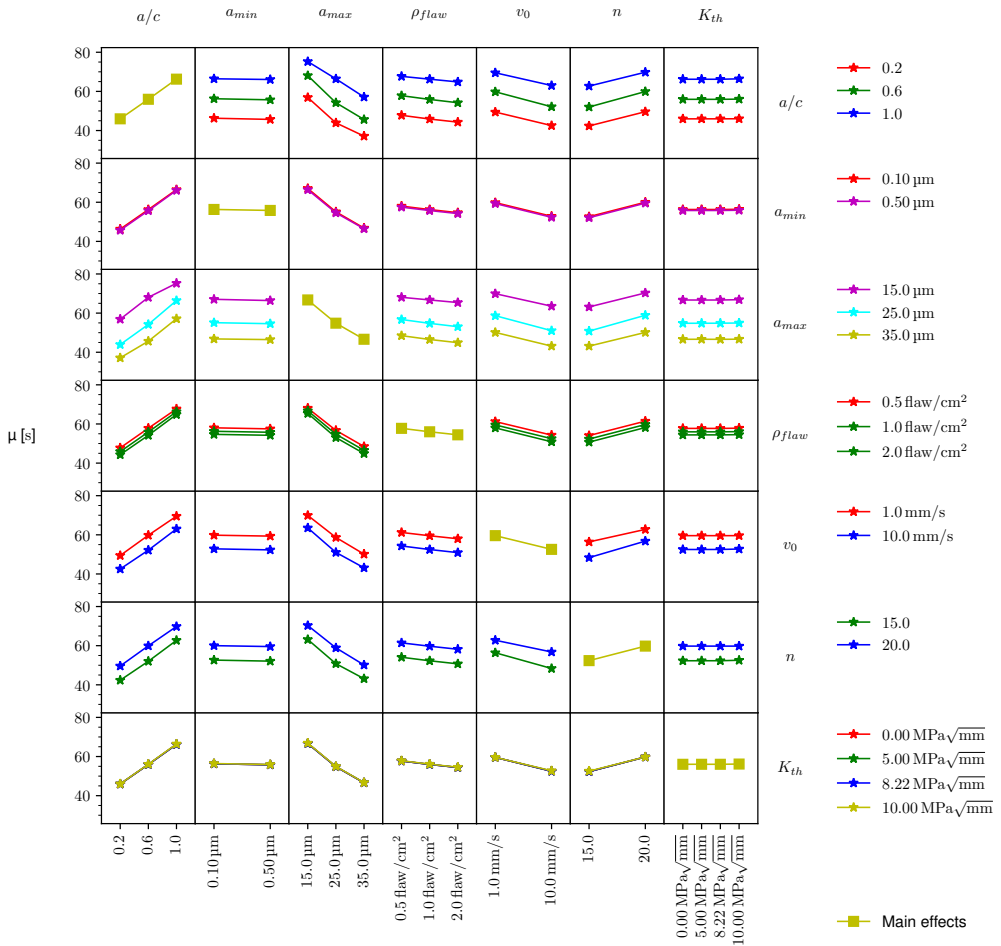
Figure 3.14: Sensitivity analysis in form of a full factorial design interaction plot of the GSPM input parameters for the quasi-static water pressure test series. The comparison index, μ, is the time at failure.

3.4 Application

We conducted a new calibration similar to the presented procedure in Section 3.3 for three quasi-static windshield test series performed by Rudshaug et al. [133], summarized in Table 3.6. In the test series, a wooden impactor with a diameter of 200 mm impacts the windshield, which is supported by a customized wooden frame, at a speed of 13 mm/min in the center of the windshield. The test series was divided into two groups based on the windshield production, each with its own set of GSPM input parameters. The first group consists of windshields produced in the concept stage, while the second group consists of windshields of cars in the production stage. Variations in flaw size distribution on the windshield surfaces, as reported by Brookmann [33], are

ignored in the calibrations. In addition, we do not include possible initial residual stresses. These phenomena are typically important close to the windshield boundaries, but since the majority of the fracture initiations are located in the center area of the windshield for the current test setup, we consider it safe to not take them into account. Predictions of the fracture initiation locations using the calibrated input parameters are shown in Figure 3.15. We find that the fracture initiation locations of the experiments fall within the areas predicted by the GSPM. The GSPM outputs information about the fracture initiation surfaces, which are distinguished in Figure 3.15 (d-f). For both the coupe car and the SUV windshield test series, the first fracture occurs in the center of the windshield, while a greater scatter is seen for the SUV concept windshield.

To demonstrate the application of the material model version of the GSPM, we performed two simulations for the SUV concept test series using the GSPM coupled to an available glass material model in LS-DYNA named MAT_280 (or MAT_GLASS) [134]. In the coupling, the GSPM predicts the tensile strength, the initiation location and the initiation time for the first crack. By setting the failure percentile parameter P_f to 0.05 and 0.95, we aim to map the expected scatter in the behavior for the windshield test series. We assigned the same strength, i.e., the same P_f, for both of the windshield glass layers. The tensile fracture strength after the first crack was set to 30 MPa and 75 MPa respectively. Figure 3.16 presents the force-displacement curves of the two simulations run with the GSPM material model version coupled to MAT_280 in LS-DYNA plotted against the experimental force-displacement curves. The experimental curves are all within the 0.05 and 0.95 percentile simulations for the first fracture. Note that the simulation curves display a single force drop at failure, unlike some of the experimental curves, where the force drops when one glass layer fails, and the remaining intact glass layer keeps carrying the load until total failure. This is probably linked to our choice of assigning the same fracture strength for both of the windshield glass layers. If we instead had selected different fracture strengths for the two glass layers, we would most likely see two force drops. Figure 3.17 shows the resulting crack patterns from the performed simulations. The crack patterns clearly differ. The weak windshield ($P_f = 0.05$) has many radial cracks and a small radius for the circular cracks, while the strong windshield ($P_f = 0.95$) has fewer radial cracks, but larger elliptically shaped cracks closer to the boundaries. The difference in crack pattern is most likely linked to the stress field at fracture, which is more evolved for the strong windshield compared to the weak windshield.

Table 3.6: The quasi-static impact test series on windshields performed by Rudshaug et al. [133].

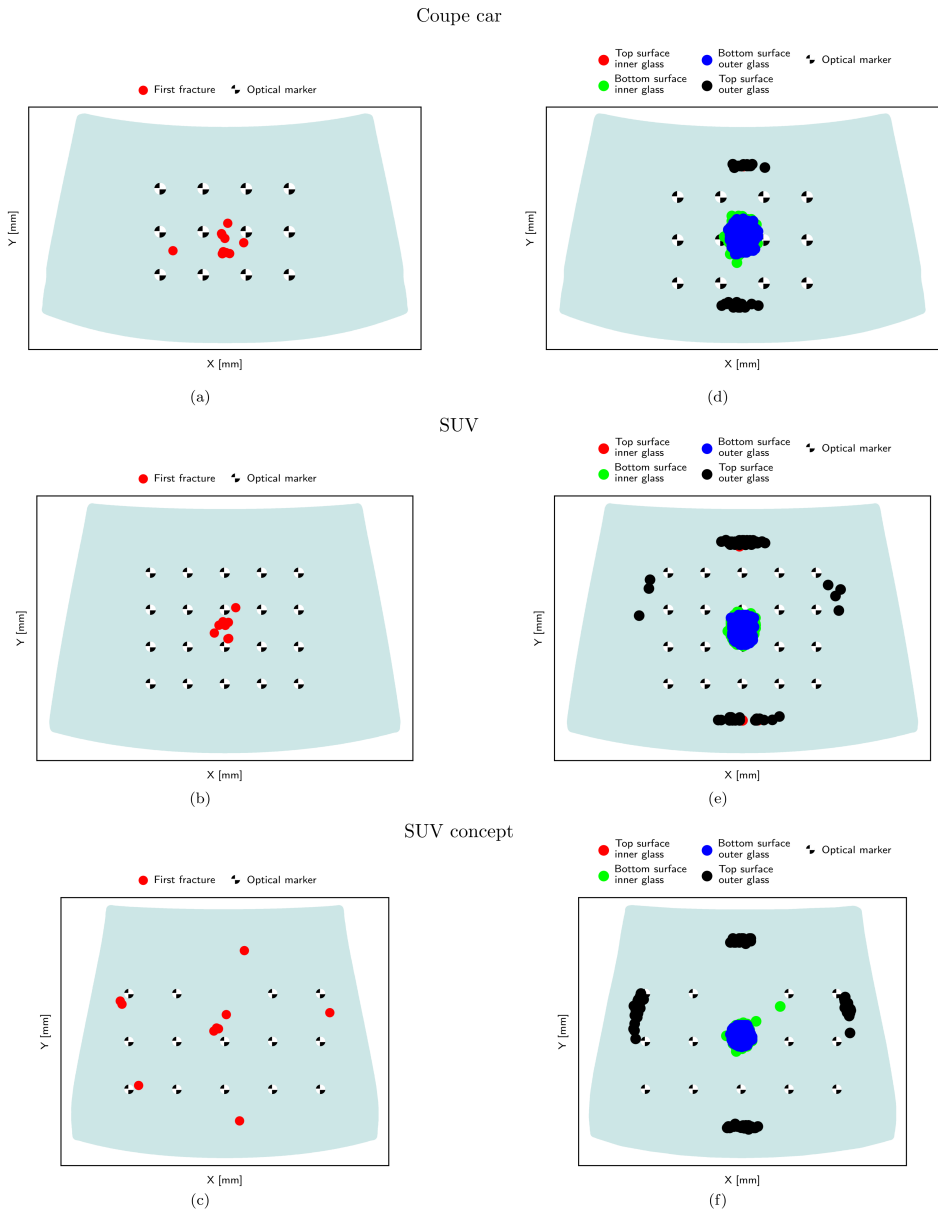| Test series	Number of tests
Coupe car	10
SUV	10
SUV concept	11

Figure 3.15: Predictions of the fracture initiation locations for the first fracture using the calibrated input parameters for the windshield test series performed by Rudshaug et al. [133]. The fracture initiation locations for the first fracture in the experiments are displayed on the left for the coupe car (a), the SUV (b) and the SUV concept car (c). The corresponding predicted fracture initiation locations for the first fracture are displayed on the right for the coupe car (d), the SUV (e) and the SUV concept car (f). The predicted fracture initiation locations are colored based on fracture initiation surface.
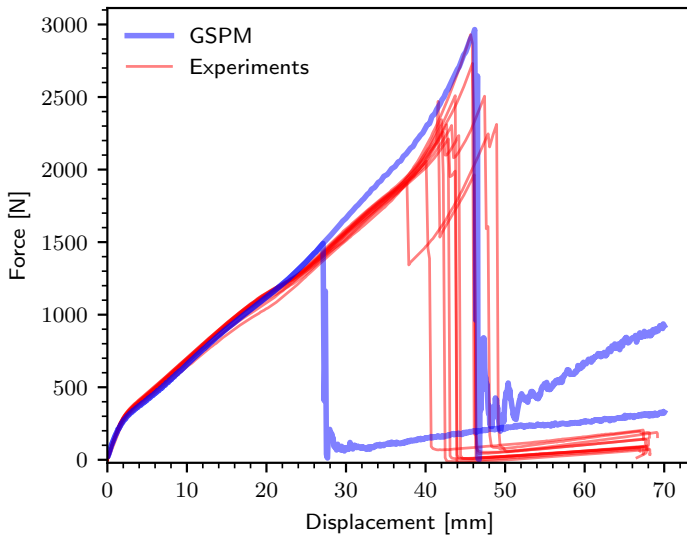
Figure 3.16: Force-displacement curves from the material model version of GSPM coupled with MAT_280 in LS-DYNA compared to experimental data from the SUV concept test series. The 0.05 and 0.95 percentile force-displacement curves (in blue) are plotted with the experimental results (in red).
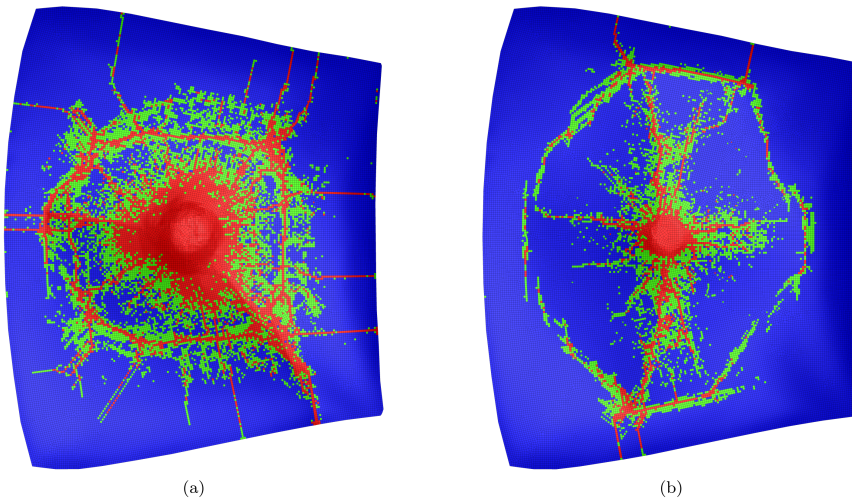

(a)   (b)

Figure 3.17: Resulting crack patterns from the simulations in Figure 3.16 using the material model version of GSPM coupled with MAT_280 in LS-DYNA for P_f values of 0.05 (a) and 0.95 (b).

59

3.5 Discussion

The proposed strength prediction model for glass named GSPM shows great promise. Based on the input parameter calibration presented in Section 3.3 and the application presented in Section 3.4, the model displays the ability to accurately predict the strength of glass plates of various geometries exposed to many different load cases. In total, the GSPM recreated the fracture behavior of 17 experimental test series, where 14 of them were on annealed monolithic glass plates, and three of them were on doubly curved laminated windshields.

There is a clear size effect where the component strength is correlated with the specimen size in the experimental test series for both the quasi-static four-point bending load case and the quasi-static impact load case on windshields. The model seems to accurately capture this effect, which stems from the flaw distribution treatment of the model. Based on the presented predictions on the low-velocity impact and blast load test series (Figure 3.10) and the quasi-static punch test series (Figure 3.11), it is clear that the GSPM introduces rate effects in glass in a reasonable manner. The presence of SCG in combination with the assumed flaw distribution seems to work satisfactory. Moreover, the GSPM appears to predict the areas of fracture initiation on complex plate geometries, see Figure 3.15.

The sensitivity study conducted in Section 3.3 provided some interesting observations. We observed that the value of the flaw depth-to-half-length ratio, a/c, is positively correlated to the predicted time at failure. The flaw depth-to-half-length ratio decreases the value of the geometric factor, Y, increasing the critical stress normal to the flaw if the depth is kept constant, see Equation (3.2). In contrast, the maximum flaw depth, $a_{\max}$, is negatively correlated for all the presented cases. The minimum flaw depth, $a_{\min}$, did not affect the predicted time at failure for the selected values. However, the studied values of $a_{\min}$ were relatively small, and it is expected that larger values will alter the predictions.

The sensitivity study also confirms that the effect of the model input parameters vary depending on the load case and geometry. For instance, the flaw density, ρ_{flaw}, did not affect the quasi-static water pressure predictions in Figure 3.14, but displayed an effect on the quasi-static four-point bending test series in Figure 3.12, and an even larger effect for the low-velocity impact test series in Figure 3.13. This implies that the effect of the flaw density is increasingly important for increasingly localized load cases, which is logical since the stress field is more concentrated, reducing the probability for a flaw to become critical. The input parameters affecting the SCG behavior, the terminal crack growth speed, v_0, the SCG exponent, n, and the stress intensity threshold for SCG, K_{th}, do not exhibit a significant effect on the predicted time at failure for the low-velocity impact test series. For both the quasi-static four-point bending and water pressure test series we observe a small negative correlation for the terminal crack growth speed and a small positive correlation for the SCG exponent with the predicted time at failure.

The material model version of the GSPM, which allows for coupling to existing damage models for glass in FE codes, extends the area of application to cases including multiple glass plates with inter-dependent failure behavior, as illustrated in Section 3.4. This feature is particularly

interesting for the automotive industry, where many parts of the vehicle consist of glass and the whole fracture process is of interest. In the example presented in Section 3.4, we demonstrated an application for the material model version of the GSPM relevant for the automotive industry. When the input parameters regarding the flaw distribution and SCG are calibrated, the user can select a representative case of a glass plate fracture strength simply by altering the failure percentile parameter, P_f. In our example, we selected percentile values of 0.05 and 0.95, ignoring the rarest cases in both tails of the strength distribution. This feature allows the user to run numerical simulation on glass plates with a design criterion.

It is important to remember the underlying assumptions of the model regarding the flaw distribution and shape. We assume that the surface flaws are uniformly distributed and non-interacting. Based on the prediction results, these assumptions seem to be sufficient. In addition, we assume that the flaws are semi-elliptically shaped, meaning that the flaws have zero width. With this assumption, we are likely to overestimate the stress concentrations around the flaw. Only mode I loading is considered in the GSPM. Including mode II and III could be of interest in further work. We assume that the tin- and air-side of the glass plates have equal flaw distribution. It would be interesting to see how the predictions are affected by treating the sides separately. In order to critically assess the model assumptions and possibly reduce the number of parameters, more validation cases are necessary.

3.6   Conclusions

In this study, we presented a new Glass Strength Prediction Model (GSPM) with a modified representation of the surface flaw distribution and sub-critical crack growth (SCG) features. In addition, we introduced a material model version, which allows for coupling with damage models in finite element (FE) codes. The GSPM was extensively tested against a total of 17 experimental test series on glass plates of various geometries exposed to load cases spanning from four-point bending to blast pressure. The presented calibration procedure proved to be robust and able to handle large sets of experimental test series. Based on the presented comparisons to experimental data we conclude that the new GSPM shows great promise, and may serve as an applicable tool in modern design processes of glass structures.

From the study, we draw the following main conclusions:

- The GSPM is able to predict the rate- and size-dependent nature of glass.

- The GSPM accurately predicts the locations of fracture initiation on complex plate geometries.

- Of the input parameters, the maximum surface flaw depth and the depth-to-half-length ratio have the greatest influence on the strength predictions.

- The two model versions (post-processor and material model) provide a flexible package for calibration and application of the GSPM.

4   Experiments on L-shaped specimens

This chapter is based on Paper III, "Effect of load level on cracking of L-shaped soda-lime glass specimens", The chapter presents the generation of a database of 20 experiments on quasi-statically loaded L-shaped glass specimens using a proposed reliable experimental setup. The proposed setup allows for detailed extraction of the crack propagation path and speed for varying critical load levels.

4.1   Introduction

Fracture is considered to be one of the most difficult problems in mechanics [135]. In the worst case, unstable crack propagation can lead to catastrophic failure of structures with the potential of inhabitant injuries and casualties. Brittle fracture is particularly difficult because of the limited deformations before failure and the rapid and sudden crack propagation. For brittle materials, like glass, fracture typically initiates in microscopical cracks, often referred to as flaws. Griffith [15] was the first to propose a connection between fracture stress and flaw size back in 1921. Griffith formulated a fracture theory stating that for a flaw to become unstable, and fracture to initiate, the reduction in potential energy that results from an increment of crack growth has to overcome the surface energy of the material.

Irwin [16] introduced the concept of energy release rate, and showed that the stresses and displacements near the crack-tip could be described by a single constant that was related to the energy release rate, i.e., the stress intensity factor. The expressions for the stress intensity factor vary based on the loading mode experienced by the crack. There are three types of loading that a crack can experience, referred to as mode I, II and III [18]. Mode I loading is the case where the principal load is applied normal to the crack plane. This mode tends to open the crack and is usually called the opening mode. Mode II corresponds to in-plane shear loading and tends to slide the crack faces with respect to each other. Mode III loading is an out-of-plane shear loading. A cracked body can experience any of these modes, or a combination of them, and is typically referred to as mixed-mode loading.

When the potential energy reduction overcomes the surface energy of the material, fracture initiates according to Griffith [15]. At this point, the stress intensity factor is above its critical value and we have unstable crack growth. This unstable crack growth is particularly violent for brittle materials, such as soda-lime glass, exhibiting a dynamic fracture process involving fast propagating cracks. There are several important challenges regarding dynamic fracture characterization of soda-lime glass [36, 37]. First, the opening displacement at the crack tip is small, typically less

than 100 nm [36]. Second, the crack growth process is highly transient, with crack speeds reaching up to ~1500–1600 m/s after a few microseconds [36, 38]. Third, the crack propagation typically involves branching. The propagation path and speed are important measures related to crack propagation. These measures provide key information about the material behavior and loading conditions, and are important for the development and evaluation of numerical fracture models. The crack propagation properties are affected by many aspects, including loading conditions, temperature, humidity, chemical composition, production method, and the presence of surface defects or impurities.

Many studies have been performed on amorphous brittle materials subjected to constant stress. Early theories suggested that the crack would accelerate until reaching the limiting crack speed assumed to be the Rayleigh wave speed of the material. Sharon and Fineberg [136, 137] and Fineberg et al. [138] proved that the crack speed does not reach those levels. Fineberg and Marder [139] addressed the status of the field of brittle dynamic fracture and presented three common methods for measuring the crack speed in experiments: optical methods, resistive measurements, and ultrasonics measurements. Optical methods are most straightforward, where high-speed cameras combined with post-processing methods are used to capture the crack propagation. Resistive measurements of the crack speed are done by use of a grid of thin electrically conductive strips that is adhered to the sample surface. In ultrasonic measurements, the running crack is perturbed by an ultrasonic wave generated from a sample boundary to map the crack position. The accuracy of all the mentioned methods is dependent on a combination of temporal and spatial resolution. One issue that arises is linked to how the crack speed measures are averaged between the sampling points both in the spatial and temporal domain [140]. The sampling point averaging may damp out possible peak crack propagation speeds, leading to loss of information.

Besides soda-lime glass, Homalite-100 and Polymethyl methacrylate (PMMA) are other amorphous brittle materials typically investigated with emphasis on fracture. Bradley and Kobayashi [141], Kobayashi et al. [142] and Dally [135] used photoelasticity to monitor crack propagation in Homalite-100 and extracted the stress intensity factor along the crack path. Ramulu and Kobayashi [143] investigated crack branching in Homalite-100 using photoelasticity and proposed a necessary condition based on a critical dynamic stress intensity factor and a sufficient condition of minimum characteristic distance for crack curving. Berezovski [144] proposed a mathematical description of the crack propagation speed of a straight brittle crack for Homalite-100. However, such an analytical model is not valid for curved, arbitrary crack propagation paths where the stress fields become complex.

Periasamy and Tippur [145] introduced a full-field optical method called Digital Gradient Sensing (DGS). With DGS, they measured small angular deflections of light rays proportional to in-plane stress gradients in transparent solids. They further used the method in both static and dynamic investigations [146]. Sundaram and Tippur [147–149] studied dynamic crack-interface interactions in PMMA bilayers after extending DGS. Recently, Sundaram and Tippur [150, 151] have used DGS coupled with ultrahigh-speed photography to characterize static and dynamic fracture of laminated glass. They were able to quantify fracture parameters including crack speed, stress intensity factors, and energy release rate from their optical measurements at crack initiation and

crack branching. Dondeti and Tippur [36, 152] compared three full-field optical methods to study dynamic crack evolution. They compared photoelasticity, 2D DIC and DGS with the conclusion that DGS is most suited, and used DGS to investigate mixed-mode fracture in soda-lime glass. Nielsen et al. [153] initiated fracture in square tempered glass plates using a diamond drill. They investigated the fragmentation pattern and measured the crack propagation speed using high-speed cameras. Xu et al. [72] developed a drop-weight experimental setup with high-speed cameras and a 4×4 multi-spark box to capture dynamic crack propagation in monolithic and laminated glass exposed to dynamic impact loading. Chen et al. [73, 154] used the same setup to measure the radial and circular crack propagation of PVB laminated glass subjected to dynamic out-of-plane impact loading. They reported increasing crack propagation speeds for increasing impact velocities. In the mentioned studies that involve glass specimens, the crack speed is not necessarily constant, but highly dependent on the specimen geometry and the boundary and loading conditions. However, the studies do not investigate how varying static load affects the crack propagation speed of soda-lime glass specimens.

As mentioned, the fracture initiation behavior of brittle materials, like glass, is governed by flaws. The flaws are randomly distributed on the outer glass surfaces, with varying shapes, orientations and sizes. For this reason, fracture initiation in soda-lime glass is stochastic in nature. Depending on the flaw distribution, the critical stress at fracture initiation will vary from specimen to specimen. The varying critical stress leads to varying critical load levels at fracture, which results in varying potential energy at fracture initiation. Following Griffith [15], the amount of available potential energy at fracture initiation is directly linked to the amount of fracture surfaces opened during the fracture process. For a single, non-branching crack, this potential energy must govern the speed of crack propagation.

To investigate how different static loads affect the crack propagation properties of soda-lime glass, we need to fix the fracture initiation point. The brittleness of soda-lime glass can make manufacturing of test specimens challenging. Float glass plates are typically cut using a score and break technique [155]. To obtain more complex geometries, three methods can be used: hot airjet cutting, laser cutting and waterjet cutting. Hot airjet cutting is a two-stage process where the glass edge is scratched first, before the hot airjet is used to propagate the crack. A limitation with hot airjet cutting is that it produces a heat affected zone near the cut edge, generating residual stresses. Laser cutting techniques involve using a laser beam to melt and vaporize the glass, creating a clean cut. Laser cutting is highly precise and can be used to cut intricate shapes and patterns. To manufacture the L-shaped specimens tested in this study, we used the waterjet technique. Waterjet cutting is a cutting technique where a high pressure water beam, which can contain an abrasive material, is used to cut the glass plate. A benefit of waterjet cutting is that it does not introduce thermal stresses near the cutting edge. A drawback with the method is that the resulting edges become somewhat coarse. However, a coarse edge may increase the scatter in flaw size, resulting in the desired varying critical stresses at fracture initiation.

In this study we aim to design an experimental setup suitable for investigation of the crack propagation in statically loaded L-shaped soda-lime glass specimens with varying load levels at fracture. By introducing an inner corner, we fix the fracture initiation point making tracking of

the crack propagation possible. To investigate how both the crack propagation path and speed are affected by the load level at fracture, we perform 20 experimental repetitions. The L-shaped specimens are loaded to trigger a non-trivial, curved crack path. We aim to provide a consistent experimental database from the 20 tested glass specimens that can facilitate the development of numerical models.

4.2 Experimental setup

This study aims to investigate how varying load levels at fracture affect the crack propagation of soda-lime glass in a controlled environment. To fix the fracture initiation location, we introduce a geometrical singularity in the form of a sharp inner corner in the glass specimen. In this way, we make sure that the stress intensity is critical at the same point for each experiment. This allows us to focus our high-speed cameras on a small region so that we can increase the filming frequency. With this setup, we are able to gather data on the crack propagation and force level at fracture.

4.2.1 Test setup

The experimental setup is presented in Figure 4.1. The setup consists of an L-shaped glass specimen, a tie-down strap, a threaded steel rod, a universal testing machine, a LED lighting source and two synchronized high-speed cameras. A total of 20 glass specimens with a thickness of 1.8 mm were cut using a waterjet to the L-shaped geometry seen in Figure 4.1 (c). Waterjet cutting was used to make the inner corner as sharp as possible. One drawback with the waterjet cutting is that the resulting edge finish is somewhat rough, see Figure 4.2. The resulting inner corner is not perfectly sharp, but slightly rounded. However, the rough inner corner introduces a scatter in flaw size, which facilitates varying critical stresses. The glass specimens were clamped on the top using a clamping device with a rubber surface and restrained by a polymer tie-strap on the right-hand-side. Some basic mechanical properties for soda-lime glass are presented in Table 4.1.

Table 4.1: Basic properties of soda-lime glass [9].

Density ρ [kg/m^3]	Young's modulus E [MPa]	Poisson ratio ν [-]
2500	70 000	0.23

We loaded the specimens with an Instron 2 kN 5944L2034 testing machine, shown in Figure 4.1 (b), in two loading dependent stages. At the start of the experiment, until the load level reached 50 N, we applied a loading rate of 10 mm/min. After the load level reached 50 N we reduced the rate to 1 mm/min. We chose this loading procedure to reduce the execution time for each experiment. The LED source is placed behind the specimen to provide sufficient lighting conditions for the crack to be visible in the high-speed camera footage. Two Phantom v2511 high-speed cameras [100] were used to capture the crack propagation in the L-shaped glass specimen. The cameras were placed at an angle to the glass surface in order to enhance the visibility of the propagating crack. The field of view was reduced to 49.8 mm × 27.0 mm using a camera resolution of 384 pixels × 208 pixels to obtain a filming rate of 200 000 fps, resulting in a spatial resolution of 7.7 pixels/mm and a

sampling rate of 5 µs. Figure 4.1 (a) shows an illustration of the high-speed camera placement with the view from Camera 1 and Camera 2, respectively.
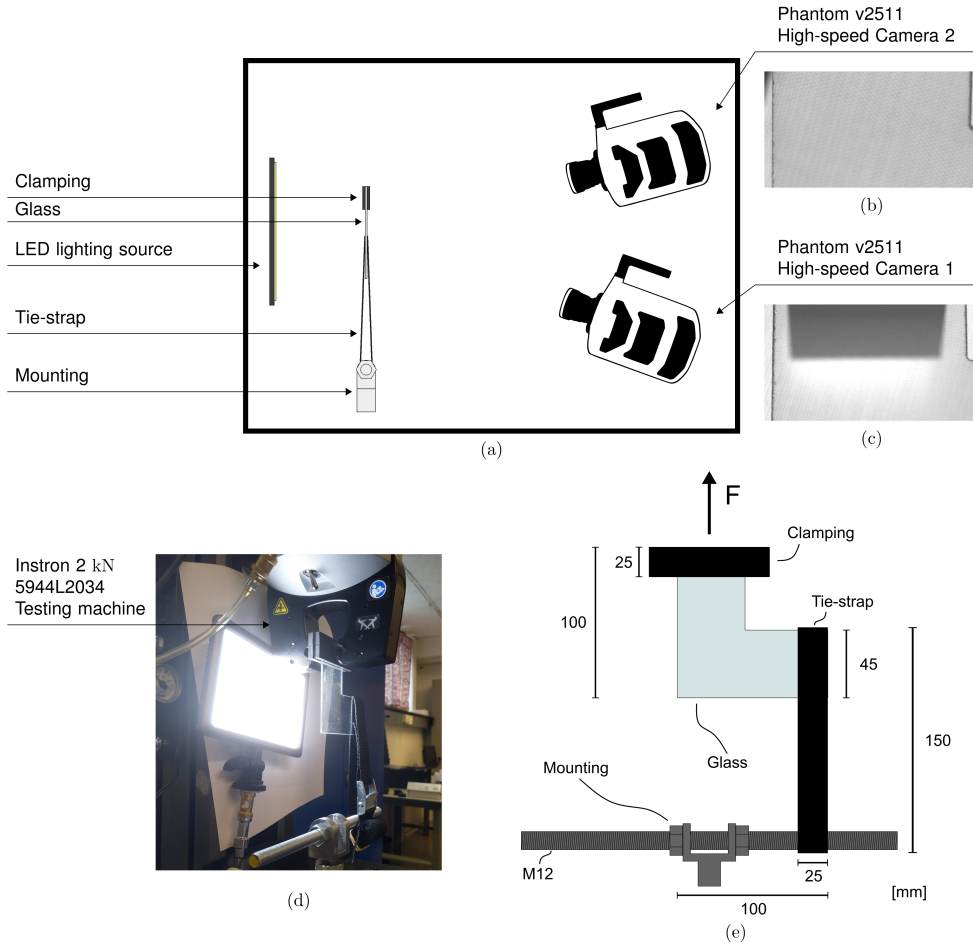

Figure 4.1: Side-view of the experimental setup and high-speed camera placement (a), the view of Camera 2 (b) and Camera 1 (c), the testing machine (d), and sketch of the experimental setup with dimensions in mm (e).
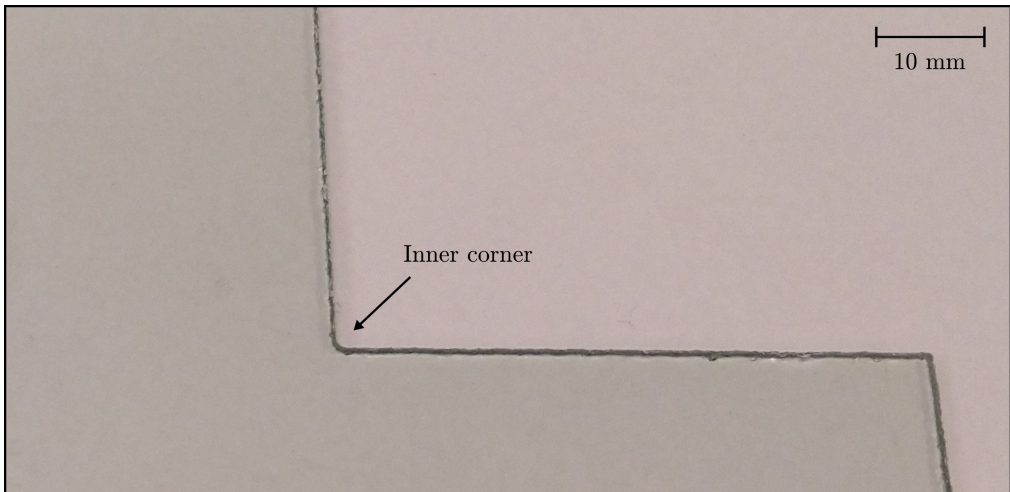
Figure 4.2: Edge finish of the waterjet-cut L-shaped specimen.

4.2.2 Tie-down strap

We used a tie-down strap to restrain the upward displacement of the right-hand-side of the glass specimen. The tie-down strap is a flexible polyester webbing which is strong in tension and typically used to mount objects during transportation. The flexible nature of the strap is beneficial in the present loading situation because it allows the strap to wrap around the glass specimen, ensuring in-plane loading. The mechanical behavior of the tie-down strap in the force range of the experiments was obtained by performing a simple tension test with the setup shown in Figure 4.3a. The resulting force-displacement curve is presented in Figure 4.3b. As expected, the tie-down strap exhibits a non-linear behavior.
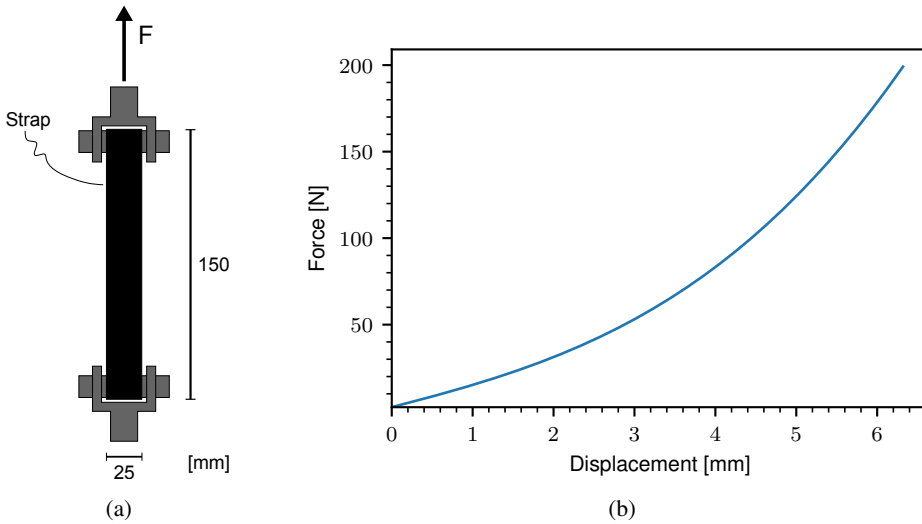
Figure 4.3: Experimental setup for the tie-down strap test (a) and the resulting force-displacement curve (b).

4.2.3 Testing procedure

The experiments were conducted using an Instron 2 kN 5944L2034 testing machine at SIMLab, NTNU. We performed all the experiments indoors at a room temperature of 23 °C. To ensure reproducible results we followed a strict testing routine described in Box 4.1.

1. **Prepare glass specimen**
   - Inspect specimen for damage and imperfections
   - Clean the specimen
2. **Prepare test setup**
   - Place the specimen in the clamp
   - Ensure that the specimen is aligned
   - Place the strap on the right-hand-side corner of the specimen
3. **Testing**
   - Apply an upward displacement following a two-step loading procedure, where a loading speed of 10 mm/min is applied until the load level reaches 50 N, then reduced to 1 mm/min
4. **Track data**
   - Track force from the load cell and displacement from the movement of the cross head of the testing machine
   - Trigger the Phantom high-speed cameras manually at fracture initiation using a frame rate of 200000 fps
5. **After testing**
   - Clean and vacuum the setup for glass fragments

Box 4.1: Testing procedure.

4.2.4 Crack propagation

We retrieved the crack propagation data from the resulting time lapses gathered by the high-speed cameras. Due to the discrete nature of the high-speed footage, we are restricted to consider the average incremental crack velocity, approximating the crack propagation velocity, $\mathbf{v}(t)$, by

$$\mathbf{v}(t) \approx \bar{\mathbf{v}}(t_i) = \frac{\Delta \mathbf{X}_i}{\Delta t_i} \tag{4.1}$$

where $\bar{\mathbf{v}}(t_i)$ is the average incremental crack velocity between image frames at time t_{i-1} and t_i, $\Delta \mathbf{X}_i = \mathbf{P}_i - \mathbf{P}_{i-1}$ is the vector representing the incremental crack growth, connecting the crack tip positions $\mathbf{P}_{i-1}$ and $\mathbf{P}_i$ from time t_{i-1} to t_i, respectively, and $\Delta t_i = t_i - t_{i-1}$ is the time increment. To obtain global coordinates from the image coordinates we utilize the known specimen geometry to generate a transformation matrix, $\mathbf{T}$, given by

$$\mathbf{T} = \begin{pmatrix} p_x & 0 \\ 0 & p_y \end{pmatrix} \tag{4.2}$$

where p_x and p_y are the spatial pixel resolutions in the local image x and y directions. By assuming a uniform spatial pixel resolution, $p = p_x = p_y$, we use the transformation matrix to compute the global coordinates $\mathbf{X} = (X, Y)$ from the local image coordinates $\mathbf{x} = (x, y)$ through

the transformation

$$\mathbf{X} = \mathbf{Tx}. \tag{4.3}$$

By careful manual tracking of the crack tip, we estimated for all specimens the crack tip positions $\mathcal{P} = \{\mathbf{P}_i \,|\, i \in \mathbb{N}, 0 \leq i \leq n\}$, where n is the number of increments with visible crack growth. Figure 4.4 presents the procedure for obtaining the crack tip positions. First, in Figure 4.4 (a), the position of the crack tip is selected through visual inspection at time t_{i-1}. In Figure 4.4 (b), at time t_i, the crack propagates beyond point $\mathbf{P}_{i-1}$. Then, in Figure 4.4 (c), the position of the crack tip at time t_i, $\mathbf{P}_i$, is manually selected. Finally, the incremental crack growth $\Delta \mathbf{X}_i$ is approximated as the vector connecting $\mathbf{P}_{i-1}$ and $\mathbf{P}_i$.

(a) (b) (c)
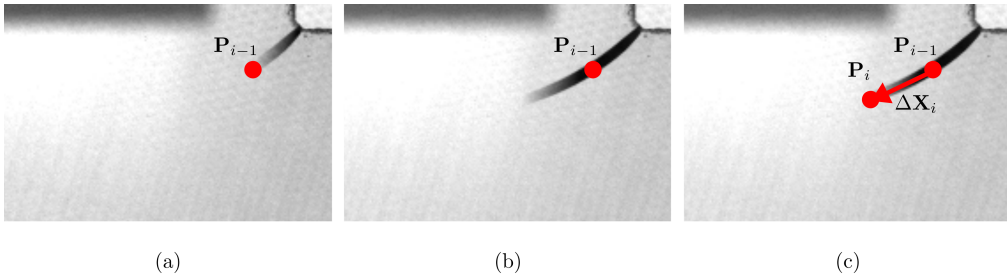
Figure 4.4: Illustration of the manual crack propagation measurement procedure. (a) The position of the crack tip is selected through visual inspection at time t_{i-1}. (b) At time t_i, the crack propagates beyond point $\mathbf{P}_{i-1}$. (c) The position of the crack tip at time t_i, $\mathbf{P}_i$, is manually selected. The incremental crack growth $\Delta \mathbf{X}_i$ is approximated as the distance between $\mathbf{P}_{i-1}$ and $\mathbf{P}_i$.

The presented procedure is performed in an in-house Python program with a graphical user interface to facilitate repeatability. It is worth mentioning that we only use the high-speed footage from Camera 1 for the crack propagation measurements. The angle between Camera 2 and the propagating cracks was found to be too small to properly detect the crack tip at some locations along the crack path, making the crack paths nearly invisible during parts of the crack propagation. The difference is shown in Figure 4.5.
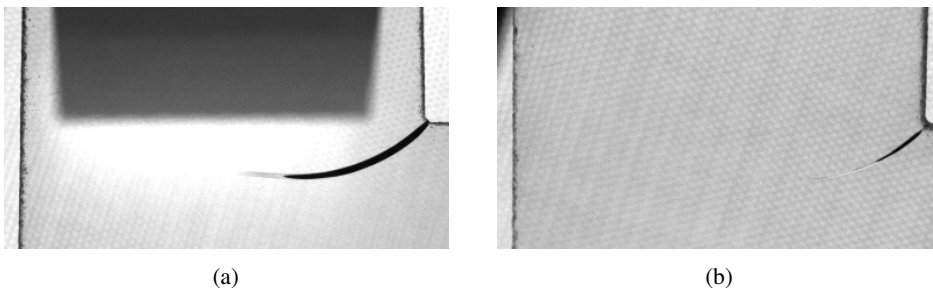

(a) (b)

Figure 4.5: An example of an image frame from (a) Camera 1 and (b) Camera 2 showing the difference in crack tip visibility.

4.3 Experimental results

The post failure state of the L-shaped glass specimens is presented in Figure 4.6. We note small variations in the crack propagation paths, which all initiate in the sharp inner corner and follow the four stages presented in Figure 4.7. In stage 1, the crack initiates in the sharp inner corner and starts propagating inclined slightly downwards. In stage 2, the crack path straightens up midway through the specimen. When the crack has propagated closer to the outer edge, it enters stage 3, where the crack propagation path inclines sharply upwards. Finally, in stage 4, the crack path straightens up again right before reaching the outer edge. A typical time-lapse of the crack propagation is presented in Figure 4.8. For the displayed specimen, the crack propagation process is in stage 1 for the first 20 µs, in stage 2 for the period 20–40 µs, in stage 3 from 40–95 µs, and in stage 4 for the final 40 µs.

(a)   (b)
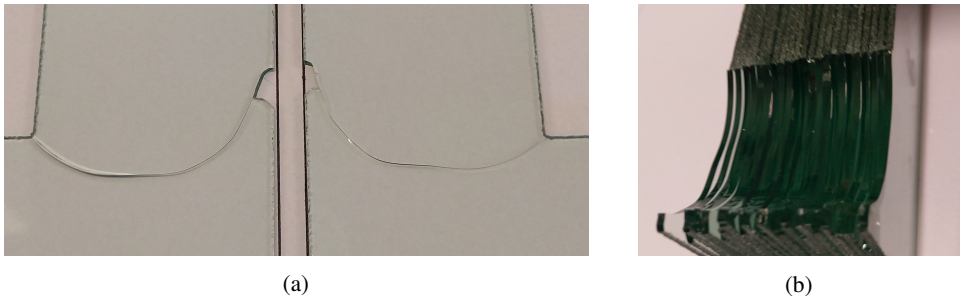
Figure 4.6: Specimens after testing displaying a consistent crack propagation path. Two specimens assembled post failure (a) and the bottom half of many specimens gathered to compare the crack propagation path (b).
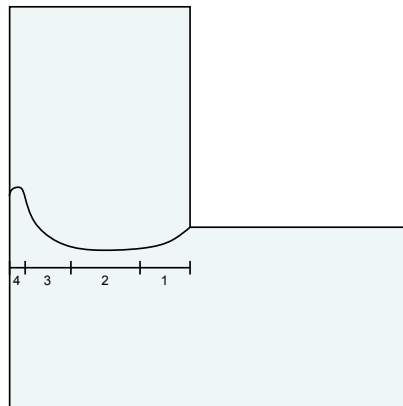

Figure 4.7: The four crack propagation path stages.

Figure 4.8: Time-lapse of crack propagation for one of the experiments. The upper dark gray field is the shadow of the testing machine.

On average, the number of crack propagation sampling points for each experiment is 25, with a crack propagation time of ~125 µs and a path length of ~50 mm. This results in an average crack propagation speed of ~400 m/s for the entire crack path. Figure 4.9 presents the temporal evolution of the crack propagation speed and length colored by the load level at fracture. We see that the

crack propagation speed decays in an exponential manner and that the measured maximum speeds exhibit a large spread, varying from ~750 m/s to ~1600 m/s. From Figure 4.9 (b) we note that the initial crack length is up to 8 mm for some of the experiments. This is an artifact of the discrete sampling procedure, where fracture initiates in-between two discrete sampling point. In this case, we do not have any information about the fracture initiation time. For that reason, we have chosen to start the speed measurements at the first full crack growth increment, ensuring that we measure a true average between sampling points. The choice of starting the speed measurements at the first full crack growth increment is also the reason why we do not see any initial crack speed ramp up. The line coloring, related to the load level at fracture, indicates that the fastest propagating cracks occur in the specimens that fail at the highest load levels. Figure 4.10 presents the initial crack propagation speed versus the related load level at fracture, and confirms that the load level at fracture affects the initial crack propagation speed. We note that the correlation seems to be rather linear.
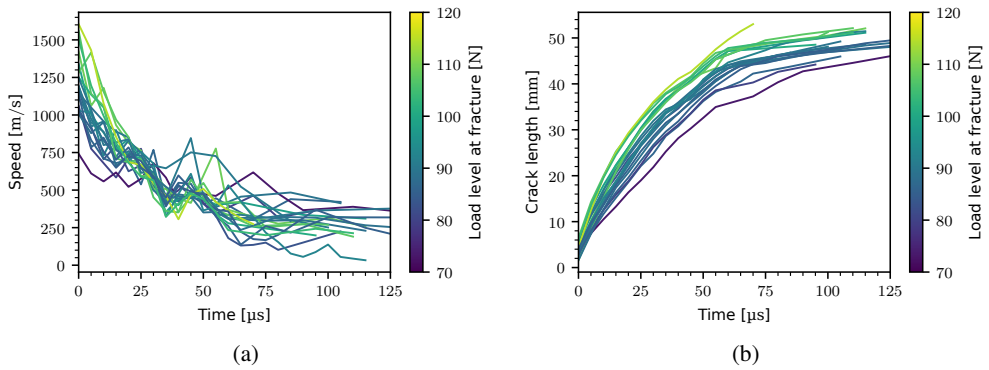

(a)   (b)

Figure 4.9: The temporal crack propagation speed (a) and length (b) curves for all the experiments colored by load level at fracture.
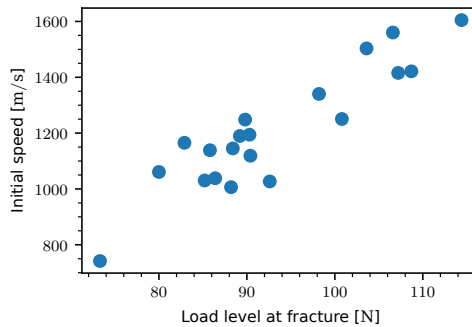

Figure 4.10: The initial crack propagation speed versus the load level at fracture.

The measured crack tip positions, P_i, from all the experiments colored with the related measured

crack propagation speed are shown in Figure 4.11a. There is a low spatial spread in the sampling points, indicating consistent boundary conditions and specimen preparation. We note the earlier discussed decay in crack propagation speed from the inner corner towards the outer edge, which is clearly visible in the plot. The zero-velocity crack tip positions closest to the inner corner are the starting points for the corresponding speed measurement of the specimen. Figure 4.11b presents the measured crack propagation paths colored with the related critical load level at fracture initiation. We find a correlation between the critical load level and the crack path, where the crack paths shift upwards with increasing critical load level.
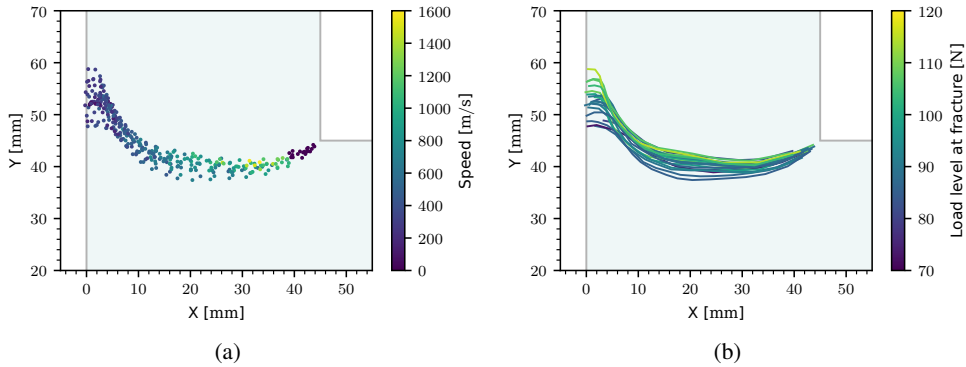

Figure 4.11: The measured crack tip positions P_i colored by crack propagation speed (a) and the resulting crack paths colored by critical load level at fracture initiation (b).

Finally, the force-displacement curves from all the experiments colored with the related initial crack speed at fracture are shown in Figure 4.12 (a). The distribution of the load level at fracture is presented in a box plot in Figure 4.12 (b). The load level at fracture is spread from ~75 N to ~115 N, and is dependent on the conditions at the inner corner. By inner corner conditions, we refer to the combination of the inner corner radius, influencing the nearby stress field, and the size of the flaws present at the inner corner. In combination, these features determine the critical load level. The specimens with the most detrimental combination (large flaws and small radius) at the inner corner are likely to fail earlier than the specimens with less detrimental conditions (small flaws and large radius). The variations stem from the specimen preparation, where we used a waterjet to cut out the geometries. The two-step loading is clearly visible in the force-displacement curves because of the small force drop at a load level of 50 N. The drop occurs as a part of the switch in loading speed. The force-displacement curves exhibit a significant spread in the stiffness up to the 50 N mark. The stiffness variation is presumably linked to the mounting of the specimen and tie-strap, more precisely the third bullet point in item 2 in the testing procedure, see Box 4.1, and how tight the tie-strap is mounted to the specimen. As the load level increases, the spread in stiffness decreases.
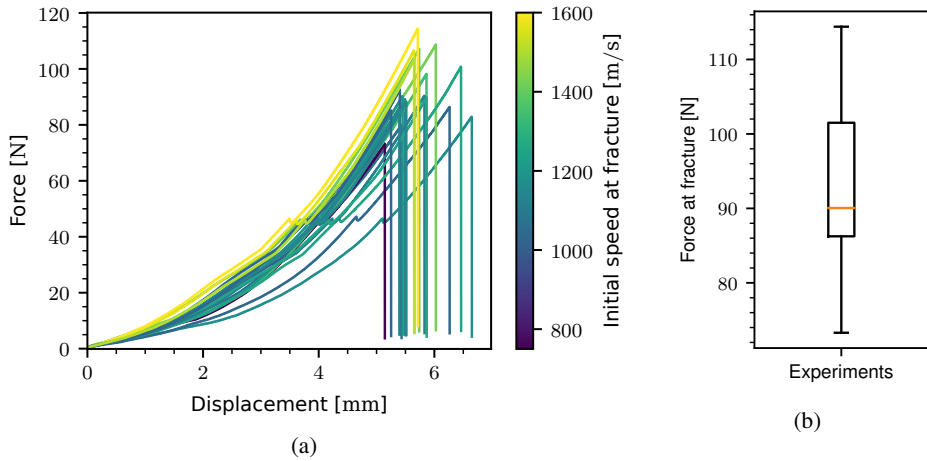
Figure 4.12: Force-displacement curves colored by initial crack propagation speed at fracture (a) and a box plot of the load level at fracture (b).

4.4 Discussion

The gathered crack paths and crack speeds imply that the experimental setup provides consistent data. We can conclude that the proposed experimental testing procedure described in Box 4.1 produced an experimental database that captures how the load level at fracture affects the crack propagation of L-shaped soda-lime glass specimens. However, we note that the temporal and spatial resolution of the setup affects the crack propagation speed measurements. The coarseness of the temporal crack propagation curves in Figure 4.9 (a) clearly illustrates that some information, like the initial crack propagation speed ramp up, is not captured. This issue could be resolved by using high-speed cameras with better temporal and spatial resolution with improved lighting conditions.

We also note that the cracks consistently follow a path similar to that presented in Figure 4.7. The curved crack path may indicate a mixed-mode crack propagation, combining opening (mode I) and in-plane shear (mode II) modes, as reported by Dondeti and Tippur [152]. Figure 4.13 illustrates the proposed combinations of the fracture modes for the three first stages. The convex shape of the curved path seen in stage 1 and 3 may stem from the mixed mode I and mode II loading at the propagating crack tip, where the lower part of the crack tip is both opened and loaded in-plane. In stage 2, a small or non-existing mode II loading may be why the crack path is close to flat. The potential in-plane shear loading in stage 1 and 3 leads to frictional energy dissipation, which may affect the crack propagation speed and contribute to the exponential decay that we observed in the measurements. To study this further, it would be interesting to use DGS to obtain in-plane stress and stress intensity fields.
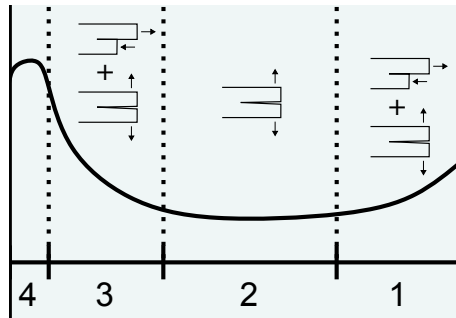
Figure 4.13: Proposed fracture mode combinations during crack propagation.

If we consider the measured initial crack propagation speeds, it is clear that the specimens which reached the highest critical load levels obtained the highest initial crack propagation speeds, see Figure 4.10. This behavior implies that there is a positive correlation between the potential energy level and the crack propagation speed, which seems reasonable considering the larger amount of available energy for creation of new surfaces. Depending on the flaw distribution of the inner corner, the load level at fracture, and thus also the potential energy at fracture, varies. As for the initial crack propagation speed, we find that the varying critical load level at fracture influences the crack propagation path, shifting the path upwards for increasing critical load level. The upward shift of the crack propagation path seen for the stronger specimens might be linked to the increased specimen deformation at fracture initiation, which slightly alters the stress field and thus also the crack propagation path.

The timing of the discrete temporal sampling points with respect to the crack initiation makes it necessary to start the crack speed measurements at the first full visible crack growth increment. The sampling interval of 5 µs is also probably too coarse to capture the initial crack speed ramp up, which can be as rapid as 2–3 µs [36]. Because of this we were not able to obtain speed data for the initial crack speed ramp up. As mentioned earlier, this could be improved with better temporal sampling resolution. However, we were able to capture the post ramp up behavior accurately. The evolution of the crack speed is interesting. The measured initial speed varies from ~750 m/s and up to ~1600 m/s, which is within the maximum speed of ~1500–1600 m/s reported in the literature [36], and there is an exponential decay during the remaining crack evolution. The reason for this behavior is that the level of available potential energy to drive the crack decreases during the crack propagation.

The stochastic nature of glass fracture is clearly visible in the presented box plot of the load level at fracture, see Figure 4.12b. The measured strength varies from ~75 N to ~115 N, meaning that the strongest specimen is ~53 % stronger than the weakest specimen. This large spread has a two-fold explanation. Fracture initiates when the stress intensity factor exceeds the critical stress intensity factor of soda-lime glass. The stress intensity factor depends on both the stress state and the orientation and shape of the present flaws. Depending on the radius of the inner corner, the stress state will vary, with higher values if the radius is sharp and lower values if the radius is

large. Both the radius of the inner corner and the orientation and shape of the present flaws will vary from specimen to specimen, explaining the observed spread in strength.

In the experimental setup, we used a polymer tie-down strap to restrain the right-hand-side of the specimen. As this strap is much softer than the glass specimen, the total experimental displacement is governed by the tie-down strap. This makes it hard to generate a repeatable stiffness response for the entire experiment even though we followed a strict testing procedure, see Box 4.1, as the tie-down strap is loosely placed over the glass specimen in the beginning of the experiment. However, as the load level increased, the spread in the stiffness in-between the experiments decreased, resulting in similar stiffness level at fracture.

4.5 Conclusion

We established an experimental database for L-shaped soda-lime glass specimens with curved crack paths which reveals how the load level affects the crack propagation speed. The study on L-shaped specimens provided consistent and repeatable crack propagation data. The measured crack propagation speed exhibits a exponentially decaying evolution, starting at speeds ranging from ~750 m/s to ~1600 m/s. We found a clear positive correlation between the initial crack propagation speeds and the corresponding load level at fracture. In addition, the load level at fracture also affected the measured crack propagation path. The crack propagation path can be divided into four distinct stages of different curvature, propagating with varying fracture modes.

From the study, we draw the following main conclusions:

- The proposed experimental setup has proved to be reliable and allows for extraction of important data such as crack path, crack propagation speed and load level at fracture initiation, for validation of numerical models.

- The initial crack propagation speed correlated positively with the load level at fracture.

- The crack propagation speed decreased exponentially with the crack length.

- The crack propagation path was affected by the load level at fracture.

5   Phase-field approach to fracture

This chapter is based on Paper IV, "Modeling brittle crack propagation for varying critical load levels: A dynamic phase-field approach", The chapter presents the implementation and validation of fracture phase-field models for shell and solid elements in LS-DYNA with three tension-compression splits and a new crack driving force allowing the user to control the fracture initiation. Among the validations are known numerical experiments and the experiments on L-shaped specimens performed in Chapter 4.

5.1   Introduction

Modeling brittle fracture in an finite element (FE) framework has proven to be a challenging task. In particular, the problem of how to represent the sharp crack discontinuity in an FE continuum has caught the attention of many researchers. Techniques such as element erosion and node-splitting to drive cracking based on a local criterion are commonly used. These techniques are typically prone to pathological mesh dependence, as the FE discretization determines the crack path resulting in the minimum potential energy. To mitigate the pathological mesh dependence, several non-local fracture formulations such as eigenfracture and fracture phase-field have been suggested.

Eigenfracture was proposed by Schmidt et al. [46] and is based on the concept of eigendeformation. In mechanics, eigendeformations are typically used to describe deformation modes of zero local energy cost. The eigenfracture formulation depends on two fields, a displacement field and an eigendeformation field. Combined, the two fields describe the fractures that occur in a body. The method has been the subject of multiple studies [47–50]. Qinami et al. [50] discussed how the FE discretization, including the number of elements and element orientation, affected the admissible fracture geometry and fracture patterns using eigenfracture, and proposed remedies using r- and h-adaptivity schemes.

The phase-field approach to fracture stems from the variational formulation of brittle fracture by Francfort and Marigo [51]. Their variational formulation relates the quasi-static process of crack initiation, propagation and branching to the minimization of the energy functional

$$E\left(\mathbf{u}, \Gamma\right) = \int_{\Omega} \psi_e\left(\varepsilon\left(\mathbf{u}\right)\right) \mathrm{d}\mathbf{x} + G_c \int_{\Gamma} \mathrm{d}\Gamma \tag{5.1}$$

where ψ_e is the elastic energy density function, $\mathbf{u}$ is the displacement field, ε is the strain field, G_c is the fracture toughness, Ω is the domain representing the elastic body and Γ is the crack set. Bourdin et al. [52] regularized the formulation of the crack set Γ to enable numerical treatment

with the energy functional

$$E_l\left(\mathbf{u}, \phi\right) = \int_\Omega \left((1-\phi)^2 + k\right)\psi_e\left(\varepsilon\left(\mathbf{u}\right)\right)\mathrm{d}\mathbf{x} + G_c \int_\Omega \left(\frac{1}{4l}\phi^2 + l|\nabla\phi|^2\right)\mathrm{d}\mathbf{x} \qquad (5.2)$$

where ϕ is the phase-field variable indicating fracture, $l > 0$ is the length scale controlling the width of the fracture phase-field and k is a small dimensionless parameter modeling an artificial residual stiffness when the material is completely fractured to prevent numerical difficulties. Figure 5.1 illustrates the introduction of the diffuse fracture phase-field to represent the sharp crack topology, Γ. The value of ϕ varies smoothly from 0 (undamaged material) to 1 (completely fractured) and degrades the elastic strain energy. The resulting phase-field differential equation is [54]

$$\frac{G_c}{l}\left[\phi - l^2\Delta\phi\right] = 2\left(1-\phi\right)\psi_e. \qquad (5.3)$$

with the Neumann-type boundary conditions given by

$$\nabla\phi \cdot \mathbf{n} = \mathbf{0}. \qquad (5.4)$$

Here, $\nabla\phi$ is the spatial gradient of the phase-field and $\mathbf{n}$ is the outward normal on $\partial\Omega$.
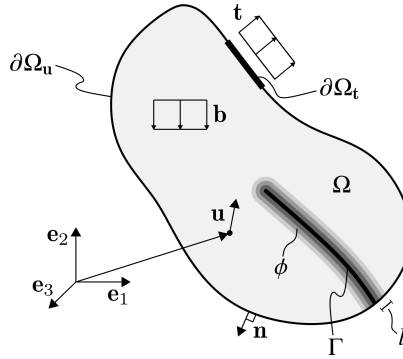

Figure 5.1: Representation of the phase-field approach to fracture. The displacement field $\mathbf{u}$ and the fracture phase-field ϕ are both defined on the body Ω, where ϕ is the regularized version of the sharp crack topology Γ with half-width controlled by the length scale l. The displacement field is constrained by the Dirichlet-type and Neumann-type boundary conditions $\mathbf{u} = \bar{\mathbf{u}}$ on $\partial\Omega_\mathbf{u}$ and $\boldsymbol{\sigma} \cdot \mathbf{n} = \bar{\mathbf{t}}$ on $\partial\Omega_\mathbf{t}$ with $\partial\Omega = \partial\Omega_\mathbf{u} \cup \partial\Omega_\mathbf{t}$. The fracture phase-field is constrained by the Neumann-type condition $\nabla\phi \cdot \mathbf{n} = \mathbf{0}$ on the full surface $\partial\Omega$.

The phase-field approach introduces an extra degree of freedom, ϕ, to the system of equations. There are two common solution methods for the coupled phase-field problem, referred to as monolithic and staggered. In the monolithic solution approach, the entire system of equations is solved directly, resulting in a complete coupling. However, the monolithic approach is computationally expensive and prone to convergence issues [53]. For this reason, the staggered solution approach

where the displacement field and phase-field are solved separately is often preferred. The staggered approach has proven to be robust and increase computational efficiency [54], and will therefore be used in this work.

Crack propagation is typically dependent on the dynamic nature of the loading [156, 157]. Crack paths display an increasing tendency to branch with increasingly dynamic loading. Early studies [55–58] on the phase-field approach investigated static fracture, while some more recent studies [59–63] consider dynamic fracture. Dynamic crack propagation is more violent than the static case, which may lead to numerical instabilities. Miehe et al. [54] introduced a viscous regularization through a viscous extended dissipation functional to stabilize the numerical phase-field solution. The viscous regularization extends the phase-field evolution equation to

$$\frac{G_c}{l}\left[\phi - l^2\Delta\phi\right] + \eta\dot{\phi} = 2\left(1 - \phi\right)\psi_e \tag{5.5}$$

where η is the viscosity parameter.

With focus on brittle cracking, we assume small deformations where $\|\nabla\mathbf{u}\|$ is small, resulting in the linearized strain tensor

$$\varepsilon = \frac{1}{2}\left[\nabla\mathbf{u} + \nabla^T\mathbf{u}\right]. \tag{5.6}$$

A physically meaningful fracture model should distinguish between tension and compression loads in such a way that cracking only arises from tension load states. Basic formulations [52, 55–57] without this type of tension-compression split, often referred to as isotropic models, are only valid in a limited number of load cases. Amor et al. [58] proposed a split based on separation of the strain tensor into a volumetric and deviatoric part, where the volumetric part of the strain tensor only contributes to damage evolution if it is positive and the deviatoric part always contributes. The split will later be referred to as the Amor split, and is defined as

$$\psi_e = \psi_e^+ + \psi_e^-, \quad \psi_e^+ = K\frac{\langle \operatorname{tr}\left(\varepsilon\right)\rangle_+^2}{2} + G\varepsilon^{dev}:\varepsilon^{dev}, \quad \psi_e^- = K\frac{\langle \operatorname{tr}\left(\varepsilon\right)\rangle_-^2}{2} \tag{5.7}$$

where $K > 0$ is the bulk modulus, $G > 0$ is the shear modulus, $\varepsilon_D = \varepsilon - \operatorname{tr}\left(\varepsilon\right)\mathbf{I}$ is the deviatoric strain tensor, $\operatorname{tr}\left(\cdot\right)$ is the trace of a tensor, the Macaulay brackets $\langle\cdot\rangle_{\pm}$ represent the ramp function $\langle x\rangle_{\pm} = \left(x \pm |x|\right)/2$. Miehe et al. [53, 54] proposed an anisotropic formulation using the spectral decomposition of the strain tensor to separate the positive and negative components, given by

$$\varepsilon = \varepsilon_+ + \varepsilon_-, \quad \varepsilon_+ = \sum_{i=1}^{3}\langle \varepsilon^i\rangle_+\mathbf{n}^i\otimes\mathbf{n}^i, \quad \varepsilon_- = \sum_{i=1}^{3}\langle \varepsilon^i\rangle_-\mathbf{n}^i\otimes\mathbf{n}^i \tag{5.8}$$

where ε^i is the ith eigenvalue, and $\mathbf{n}^i$ is the corresponding unit eigenvector of the strain tensor. The positive and negative strain tensors are used to construct the two parts of the elastic strain energies

$$\psi_e = \psi_e^+ + \psi_e^-, \quad \psi_e^+ = \lambda\frac{\langle \operatorname{tr}\left(\varepsilon\right)\rangle_+^2}{2} + \mu\operatorname{tr}\left[\varepsilon_+^2\right], \quad \psi_e^- = \lambda\frac{\langle \operatorname{tr}\left(\varepsilon\right)\rangle_-^2}{2} + \mu\operatorname{tr}\left[\varepsilon_-^2\right] \tag{5.9}$$

where $\lambda > 0$ and $\mu > 0$ are Lamè constants. The split will later be referred to as the Miehe split. For both the Amor and Miehe split, the stress tensor is defined by

$$\boldsymbol{\sigma}\left(\varepsilon, \phi_n\right) = \left[(1 - \phi_n)^2 + k\right] \boldsymbol{\sigma}^+(\varepsilon) + \boldsymbol{\sigma}^-(\varepsilon) \tag{5.10}$$

where $\boldsymbol{\sigma}^+ = \frac{\partial \psi_e^+(\varepsilon)}{\partial \varepsilon}$ and $\boldsymbol{\sigma}^- = \frac{\partial \psi_e^-(\varepsilon)}{\partial \varepsilon}$ are the positive and negative parts of the stress tensor. Ambati et al. [158] proposed a hybrid formulation containing features from both isotropic and anisotropic models where the elastic strain energy is split similarly to the splits presented above, but the stress tensor is kept isotropic to increase the computational efficiency. The split will later be referred to as the hybrid split. In this work, the elastic strain energy of the hybrid split follows Equation (5.9). For the hybrid split, the stress tensor is defined by

$$\boldsymbol{\sigma}\left(\varepsilon, \phi_n\right) = \left[(1 - \phi_n)^2 + k\right] \frac{\partial \psi_e(\varepsilon)}{\partial \varepsilon}. \tag{5.11}$$

Cracking is considered to be a fully dissipative process, meaning that the crack surface, Γ, must either stay constant or increase with time to be thermodynamically consistent. To ensure this consistency, Miehe et al. [53] proposed the following constraints on the fracture phase-field

$$\frac{1}{l}\left[\phi - l^2 \Delta \phi\right] \geq 0 \quad \text{and} \quad \dot{\phi} \geq 0. \tag{5.12}$$

where the first constraint relates the functional derivative to a positive field driving force, while the latter ensures irreversible crack evolution. By introducing a history variable for the field driving force, $\mathcal{H}$, referred to as the maximum positive reference energy, given by

$$\mathcal{H}(\mathbf{x}, t) := \max_{\tau \in [0,t]} \psi_e^+(\varepsilon(\mathbf{x}, \tau)), \tag{5.13}$$

Miehe et al. [54] presented an elegant way of incorporating the irreversibility of the crack evolution, with the evolution equation

$$\frac{G_c}{l}\left[\phi - l^2 \Delta \phi\right] + \eta \dot{\phi} = 2(1 - \phi)\,\mathcal{H}. \tag{5.14}$$

In the current formulation, the fracture phase-field evolution is based on an energy dependent crack driving force. With this type of crack driving force, it is difficult to control crack initiation. Miehe et al. [159] proposed a purely stress-based crack driving force for the fracture phase-field evolution, given by

$$\mathcal{H}(\mathbf{x}, t) := \max_{\tau \in [0,t]} \tilde{D} = \max_{\tau \in [0,t]} \zeta \left\langle \sum_{a=1}^{3} \left(\frac{\langle \tilde{\sigma}^i(\mathbf{x}, \tau)\rangle}{\sigma_c}\right)^2 - 1 \right\rangle_+ \tag{5.15}$$

where $\tilde{\sigma}^i = \sigma^i/(1 - \phi)^2$ is the effective principal stress i, σ_c is a critical stress and the dimensionless parameter $\zeta > 0$ controls the slope of the failure surface in stress space. Further, we introduce a

conditional energy based crack driving force, given by

$$\mathcal{H}(\mathbf{x}, t) := \max_{\tau \in [0,t]} H(\sigma_{\mathcal{B}} - \sigma_c) \psi_e^+ \tag{5.16}$$

where $\sigma_{\mathcal{B}} = \max\{\sigma_1 : \mathbf{x} \in \Omega,\ \tau \in [0,t]\}$ is the maximum major principal stress ($\sigma_1 \geq \sigma_2 \geq \sigma_3$) experienced in the body during the loading history and $H(x)$ is the Heaviside step function taking the value 1 if $x > 0$ and 0 otherwise. This formulation of the crack driving force allows for a surplus of elastic strain energy at fracture initiation.

Using the proposed crack driving force in Equation (5.16), we aim to investigate the prediction capabilities of a dynamic fracture phase-field formulation implemented in the commercial FE solver LS-DYNA [160] on quasi-statically loaded L-shaped soda-lime glass specimens [161] with varying critical load levels using the three implemented tension-compression splits. In particular, we focus on the crack propagation path and speed for the lowest and highest critical load levels using the new crack driving force. First, we present the implementation details and perform validation studies of the fracture formulation using standard numerical examples. Then, we perform numerical experiments on the quasi-statically loaded L-shaped soda-lime glass specimens. The three tension-compression splits, namely the Amor, Miehe and hybrid splits, are used and compared for the numerical experiments. To evaluate the numerical predictions in relation to the experiments, we compare the crack propagation path and speed for two specimen strengths.

5.2 Implementation

The dynamic fracture phase-field model is implemented in the user interface of version R12 of the general-purpose FE solver LS-DYNA. To enable scalability and reduce computational time, we parallelized the implementation using MPI. The implementation includes the Amor [58], Miehe [53, 54] and hybrid [158] tension-compression splits. To ensure control over the fracture initiation, we implemented the proposed crack driving force in Equation (5.16) that allows the user to initiate the phase-field solver based on a critical major principal stress.

To model the dynamic fracture phase-field we follow the dynamic formulation and robust staggered solution scheme proposed by Hofacker and Miehe [61]. The additional degree of freedom obtained by introducing the fracture phase-field is included in a modular fashion in the user element framework of LS-DYNA for both shells (usrshl) and solids (usrsld). The shell user element is based on the Belytschko-Tsay shell element [162, 163], while the solid element is fully integrated and employs the B-bar method to prevent locking [164]. We solve the displacement field and phase-field separately in a staggered fashion, where the system of equations related to the displacement field is assembled and solved internally in LS-DYNA in an explicit fashion. The phase-field system of equations is assembled and solved implicitly using the external Portable, Extensible Toolkit for Scientific Computation (PETSc) [165].

To implement the phase-field evolution in Equation (5.14) into an FE framework, we use the weak

form given by

$$\int_{\Omega} \left[-2\left(1-\phi\right)\mathcal{H}\cdot\delta\phi + \frac{G_c}{l}\phi\cdot\delta\phi + G_c l\nabla\phi\cdot\nabla\delta\phi + \eta\dot{\phi}\cdot\delta\phi \right] \mathrm{dV} = 0 \tag{5.17}$$

where $\delta\phi$ is the virtual infinitesimal variation of the fracture phase-field. The displacement field and fracture phase-field, along with their respective differential quantities, are discretized as

$$\mathbf{u} = \sum_{i=1}^{m} \mathbf{N}_i^{\mathbf{u}}\mathbf{u}_i = \mathbf{N}^{\mathbf{u}}\mathbf{r}^{\mathbf{u}} \quad \text{and} \quad \phi = \sum_{i=1}^{m} N_i^{\phi}\phi_i = \mathbf{N}^{\phi}\mathbf{r}^{\phi} \tag{5.18}$$

$$\varepsilon = \sum_{i=1}^{m} \mathbf{B}_i^{\mathbf{u}}\mathbf{u}_i = \mathbf{B}^{\mathbf{u}}\mathbf{r}^{\mathbf{u}} \quad \text{and} \quad \nabla\phi = \sum_{i=1}^{m} \mathbf{B}_i^{\phi}\phi_i = \mathbf{B}^{\phi}\mathbf{r}^{\phi} \tag{5.19}$$

where m is the number of nodes per element, $\mathbf{u}_i$ and ϕ_i are the displacement and phase-field values at node i, $\mathbf{N}_i^{\mathbf{u}}$ and N_i^{ϕ} are the shape function matrix and shape function associated with node i for the displacements and phase-field, respectively, and $\mathbf{B}_i^{\mathbf{u}}$ and $\mathbf{B}_i^{\phi}$ are the matrices of their respective spatial derivatives. $\mathbf{N}^{\mathbf{u}}$, $\mathbf{N}^{\phi}$, $\mathbf{B}^{\mathbf{u}}$ and $\mathbf{B}^{\phi}$ are the corresponding matrices for all the nodes and $\mathbf{r}^{\mathbf{u}}$ and $\mathbf{r}^{\phi}$ are the vectors containing the displacement and phase-field degrees of freedom. The virtual quantities ($\delta\mathbf{u}$, $\delta\phi$, $\delta\varepsilon$ and $\delta\nabla\phi$) are discretized in the same fashion. We define the rate of the fracture phase-field $\dot{\phi} = \left(\phi_{n+1} - \phi_n\right)/\Delta t$ where $\Delta t = t_{n+1} - t_n$ is the time increment. Inserting the interpolations into Equation (5.17) and eliminating the arbitrary virtual quantities yields the nonlinear fracture phase-field system of equations

$$\mathbf{R}^{\phi}\left(\mathbf{r}^{\phi}\right) = \int_{\Omega} -2\left(1 - \mathbf{N}^{\phi}\mathbf{r}^{\phi}\right)\mathcal{H}\left(\mathbf{N}^{\phi}\right)^T + \frac{G_c}{l}\left(\mathbf{N}^{\phi}\right)^T\mathbf{N}^{\phi}\mathbf{r}^{\phi}$$

$$+ \frac{\eta}{\Delta t}\left(\mathbf{N}^{\phi}\right)^T\mathbf{N}^{\phi}\Delta\mathbf{r}^{\phi} + G_c l\left(\mathbf{B}^{\phi}\right)^T\mathbf{B}^{\phi}\mathbf{r}^{\phi}\,\mathrm{dV} = \mathbf{0} \tag{5.20}$$

where $\mathbf{R}^{\phi}\left(\mathbf{r}^{\phi}\right)$ is the global fracture phase-field force vector and $\Delta\mathbf{r}^{\phi} = \mathbf{r}_{n+1}^{\phi} - \mathbf{r}_n^{\phi}$ is the increment of the phase-field degrees of freedom at time t_{n+1}. By linearizing the nonlinear system of equations through a first order Taylor expansion, we find a linear system of equations for the fracture phase-field increment

$$\mathbf{R}^{\phi}\left(\mathbf{r}^{\phi}\right) = \mathbf{R}^{\phi}\left(\mathbf{r}_n^{\phi}\right) + \frac{\partial\mathbf{R}^{\phi}}{\partial\mathbf{r}^{\phi}}\left(\mathbf{r}_n^{\phi}\right)\Delta\mathbf{r}^{\phi} + H.O.T.$$

$$= \mathbf{R}^{\phi}\left(\mathbf{r}_n^{\phi}\right) + \mathbf{K}^{\phi}\left(\mathbf{r}_n^{\phi}\right)\Delta\mathbf{r}^{\phi} + H.O.T.$$

$$\approx \mathbf{R}^{\phi}\left(\mathbf{r}_n^{\phi}\right) + \mathbf{K}^{\phi}\left(\mathbf{r}_n^{\phi}\right)\Delta\mathbf{r}^{\phi} = \mathbf{0} \tag{5.21}$$

where $\mathbf{K}^{\phi}\left(\mathbf{r}_n^{\phi}\right)$ is the phase-field stiffness at time t_n given by

$$
\begin{aligned}
\mathbf{K}^{\phi}\left(\mathbf{r}_n^{\phi}\right) &= \frac{\partial \mathbf{R}^{\phi}}{\partial \mathbf{r}^{\phi}}\left(\mathbf{r}_n^{\phi}\right) \\
&= \int_{\Omega}\left[2\mathcal{H} + \frac{G_c}{l} + \frac{\eta}{\Delta t}\right]\left(\mathbf{N}^{\phi}\right)^T \mathbf{N}^{\phi} + G_c l\left(\mathbf{B}^{\phi}\right)^T \mathbf{B}^{\phi} \, \mathrm{dV}.
\end{aligned}
\tag{5.22}
$$

Box 5.1 presents the applied staggered scheme for solving the fracture phase-field evolution, which differs slightly from the scheme presented by Hofacker and Miehe [61]. In our implementation, we solve the displacement field explicitly and use the fracture phase-field from the previous increment, ϕ_n, to degrade the stress used to construct the stress divergence vector, $\mathbf{F}_n\left(\phi_n\right)$. The choice of degrading the stress using the fracture phase-field from the previous increment is mainly due to the user interface of LS-DYNA, where the phase-field for the new increment is solved for in a user control routine (uctrl) which is called after the calls to the element and material routines. The scheme is as follows. For every increment, we know the displacement and crack driving force field from the previous time step and fracture phase-field from the previous two time steps. In addition, the velocity field at time $t_{n-1/2}$ is known. To drive the solution forward, we first use the known quantities to compute the stress field, $\boldsymbol{\sigma}\left(\boldsymbol{\varepsilon}, \phi_n\right)$ at the integration points. For the Amor and Miehe tension-compression splits, the stress field is first split into a positive and negative part, and then the positive part is degraded using the fracture phase-field at the integration point from the previous increment. The stress field is not split for the hybrid split. Next, we compute the integration point crack driving force obtained in the solution history, $\mathcal{H}$, from the expression in Equation (5.16). Together with the global fracture phase-field degrees of freedom from the two previous time step, $\mathbf{r}_n^{\phi}$ and $\mathbf{r}_{n-1}^{\phi}$, the crack driving force is used to solve the linear incremental system of equations for the fracture phase-field in Equation (5.21)

$$
\Delta \mathbf{r}^{\phi} = -\left(\mathbf{K}^{\phi}\left(\mathbf{r}_n^{\phi}\right)\right)^{-1} \cdot \mathbf{R}^{\phi}\left(\mathbf{r}_n^{\phi}\right)
\tag{5.23}
$$

Next, the displacement field of the new increment, represented by its degrees of freedom, is computed based on the current body force and external loads, $\mathbf{P}_n$, hourglass resistance, $\mathbf{H}_n$, and stress divergence vector, $\mathbf{F}_n\left(\phi_n\right)$. The stress divergence vector is integrated based on the stresses degraded by the fracture phase-field from the previous increment. Finally, the history fields are stored for the new increment.

Box 5.1: Staggered scheme for dynamic phase field fracture in $[t_n, t_{n+1}]$, adapted from Hofacker and Miehe [61].

1. *Initialization.* The displacement field $\mathbf{u}_n$ and the crack driving force $\mathcal{H}_n$ at time t_n, the previous two fracture phase-fields ϕ_n and ϕ_{n-1} at time t_n and t_{n-1}, and the velocity field $\dot{\mathbf{u}}_{n-1/2}$ at time $t_{n-1/2}$ are known. Update the prescribed loads $\mathbf{b}$ and $\bar{\mathbf{t}}$ at current time t_{n+1}.

2. *Compute stress field.* Determine the stress field at the integration points, split into positive and negative parts and degrade the positive part if Amor or Miehe split is used

$$\boldsymbol{\sigma}\left(\varepsilon, \phi_n\right) = \left[\left(1 - \phi_n\right)^2 + k\right]\boldsymbol{\sigma}^+\left(\varepsilon\right) + \boldsymbol{\sigma}^-\left(\varepsilon\right).$$

3. *Compute crack driving force.* Determine the crack driving force at the integration points

$$\mathcal{H} = \begin{cases} \max_{\tau \in [0,t]} H\left(\sigma_\mathcal{B} - \sigma_c\right)\psi_0^+\left(\varepsilon\right) & \text{for } \psi_e^+\left(\varepsilon\right) > \mathcal{H}_n \\ \mathcal{H}_n & \text{otherwise.} \end{cases}$$

4. *Compute fracture phase-field.* Determine the current global fracture phase-field degrees of freedom $\mathbf{r}^\phi$

$$\mathbf{r}^\phi = \mathbf{r}_n^\phi + \Delta\mathbf{r}^\phi$$

$$\Delta\mathbf{r}^\phi = -\left(\mathbf{K}^\phi\right)^{-1}\mathbf{R}^\phi$$

5. *Compute displacement field.* Determine the current displacement $\mathbf{u}$ with a frozen fracture phase-field ϕ_n from the *semi-discrete equations of motion at time n*. The current displacement degrees of freedom $\mathbf{r}^\mathbf{u}$ at time t_{n+1} is found using central difference time integration

$$\ddot{\mathbf{r}}_n^\mathbf{u} = \mathbf{M}^{-1}\left(\mathbf{P}_n - \mathbf{F}_n\left(\phi_n\right) + \mathbf{H}_n\right)$$

$$\dot{\mathbf{r}}_{n+1/2}^\mathbf{u} = \dot{\mathbf{r}}_{n-1/2}^\mathbf{u} + \ddot{\mathbf{r}}_n^\mathbf{u}\Delta t_n$$

$$\mathbf{r}^\mathbf{u} = \mathbf{r}_n^\mathbf{u} + \dot{\mathbf{r}}_{n+1/2}^\mathbf{u}\Delta t_{n+1/2}$$

where $\mathbf{P}_n$ represents the body force and external loads, $\mathbf{F}_n\left(\phi_n\right)$ represents the stress divergence vector, which depends on the fracture phase-field from the previous increment, and $\mathbf{H}_n$ represents the hourglass resistance. $\mathbf{M}$ is the diagonal mass matrix.

6. *Update history variables.* Store $\mathcal{H}$, ϕ, $\mathbf{u}$ and $\dot{\mathbf{u}}$ in the history database.

5.3   Validation

We adopted two of the representative numerical examples used by Miehe et al. [54], namely the single edge notch tension (SENT) test and the single edge notch shear (SENS) test, to validate the behavior of the fracture phase-field models for quasi-static mode I and mixed mode loading using the Amor, Miehe and hybrid splits. For validation of the performance in the case of dynamic fracture we model the experiments performed by Kalthoff and Winkler [156] and Kalthoff [157] in 2D and in a 3D extension case using the Miehe split. In this section the critical principal stress σ_c in Equation (5.16) is equal to 0 in order to compare the implementation to previous work.

5.3.1   Single edge notch tests

The single edge notch tests consist of a square plate with a horizontal notch at mid-height spanning from the left edge to the center point of the specimen. The geometry and boundary conditions are presented in Figure 5.2. The specimen is loaded either vertically or horizontally for tension or shear loading, respectively. The model parameters are: Lamé's first parameter $\lambda = 121.15$ GPa, shear modulus $\mu = 80.77$ GPa, critical energy release rate $G_c = 2.7 \times 10^{-3}$ J/m^2, length scale $l = 7.5 \times 10^{-3}$ mm, artificial residual stiffness $k = 0$, phase-field viscosity $\eta = 10^{-9}$ N s/mm^2, and we assume plane strain. An element size of 2.5×10^{-3} mm is used in both load cases with the proposed model, resulting in 160 000 elements.

Figure 5.3 presents the resulting crack patterns for the two load cases using the three splits. We see no notable difference in the predicted crack patterns from the SENT tests, which are straight for all three tension-compression splits. When comparing the crack path predictions from the SENS tests, we note slight differences between the respective tension-compression splits. However, they all resemble the crack patterns predicted by Miehe et al. [54] and Ambati et al. [158].
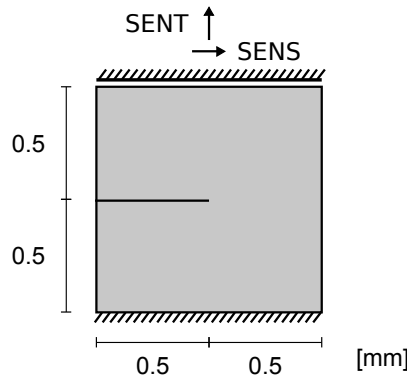
Figure 5.2: The single edge notch specimen with dimensions and boundary conditions for tension (SENT) and shear (SENS) loading.
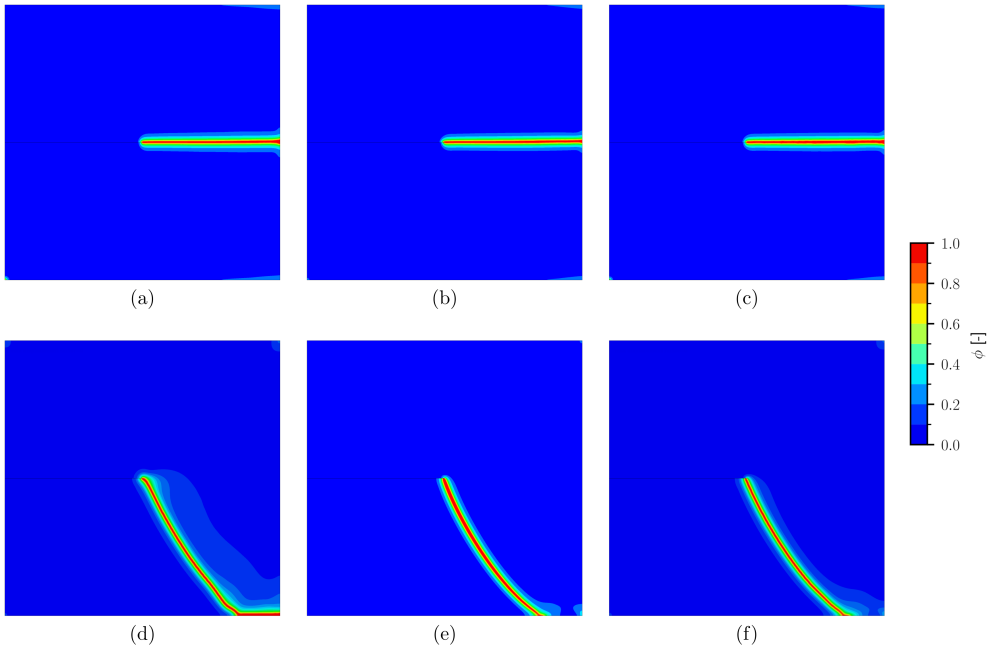
Figure 5.3: Crack patterns from numerical experiments of the SENT (a-c) and SENS (d-f) tests using the Amor (a,d), Miehe (b,e) and hybrid (c,f) splits.

5.3.2 Kalthoff-Winkler test

Kalthoff and Winkler [156] performed impact tests on a double pre-notched steel plate at different velocities, documenting the resulting crack path. Similar to Hofacker and Miehe [61], we will use the experimental results as a reference to verify the performance of our phase-field implementation with the Miehe split. The specimen geometry and boundary conditions are presented in Figure 5.4 (a). We use constant loading velocities, v_0, of 5 m/s, 16.5 m/s and 50 m/s. To avoid numerical instabilities, we ramp up the velocity from 0 to v_0 for a duration $t_0 = 0.5$ µs. The velocity profile is presented in Figure 5.4 (b). The model parameters are: density $\rho = 8000$ kg/m^3, Young's modulus $E = 190$ GPa, Poisson ratio $\nu = 0.3$, critical energy release rate $G_c = 2.213 \times 10^4$ J/m^2, length scale $l = 0.3$ mm, artificial residual stiffness $k = 0$, phase-field viscosity $\eta = 10^{-9}$ N s/mm^2, and we assume plane strain. The plate is discretized into ~155 000 elements, with a refined mesh in areas where the crack is expected to propagate. The element size is half the value of l in the refined area. To reduce computational cost, we exploit the symmetry line A in Figure 5.4 (a) and model only the upper part of the specimen.

Figure 5.5 presents the crack patterns from the numerical experiments for the three impact velocities. The average angle between the initial crack tip plane and the propagated crack is ~70°, which is in good agreement with the experimental results and the predictions by Hofacker and

Miehe [61]. We observe increasing crack branching with increasing impact velocity, from no branching for an impact velocity of 5 m/s to extensive branching when the impact velocity is 50 m/s. A notable trend is that the crack branching occurs earlier for the highest impact velocity, and that a second crack propagates from the lower right corner. The results are similar to those reported by Hofacker and Miehe [61].
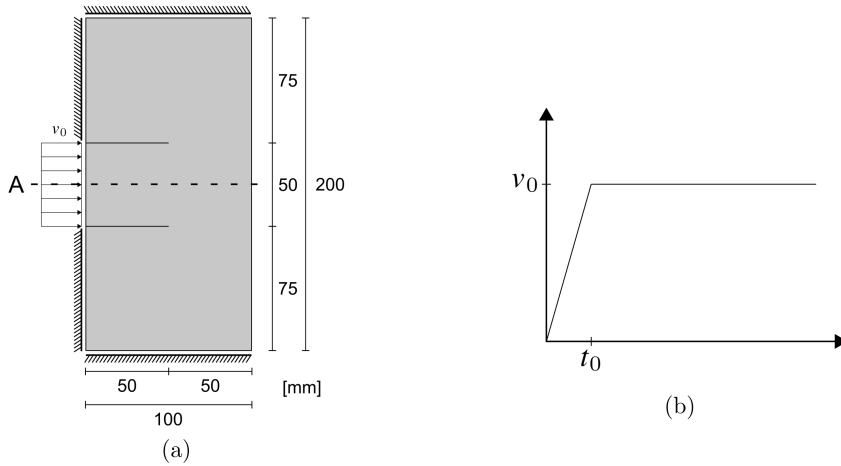
Figure 5.4: The Kalthoff-Winkler specimen with (a) dimensions and boundary conditions and (b) applied loading history.
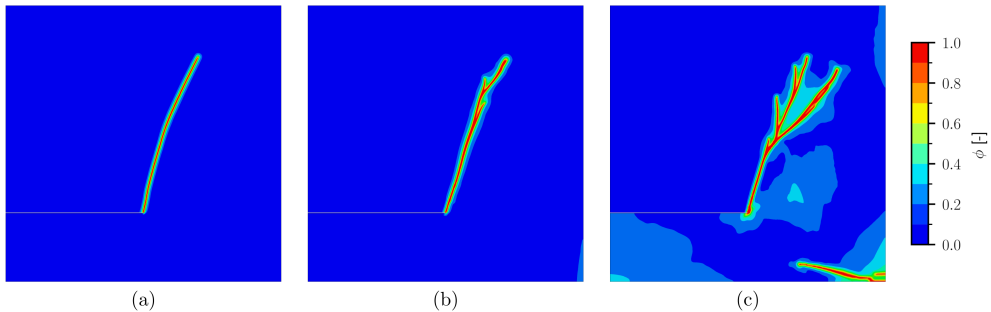
Figure 5.5: Crack patterns from numerical experiments of the Kalthoff-Winkler test with impact velocities of (a) 5 m/s, (b) 16.5 m/s and (c) 50 m/s.

5.3.3   Kalthoff-Winkler test, 3D extension

We make the same 3D extension of the Kalthoff-Winkler test as Hofacker and Miehe [61], where we assume a circular cross section for the projectile. Again, we perform numerical experiments for loading velocities of 5 m/s, 16.5 m/s and 50 m/s, and we use the Miehe split. The model

parameters are identical to the parameters used for the 2D case, except for the length scale which is set to $l = 1.0$ mm due to a coarser discretization. The specimen geometry and boundary conditions are presented in Figure 5.6 (a). All the outer boundaries are fixed except for the circular impact area and the boundary opposite to the loading plane. The geometry is discretized into ~9.8 million elements with a size of ~0.5 mm × 0.5 mm × 0.5 mm. To reduce computational time, we exploit the symmetry planes A and B in Figure 5.6 (a), and only model the upper left part of the specimen.

The resulting crack pattern evolution in symmetry plane B is presented in Figure 5.7 for the three impact velocities. Similar to the 2D case, we get increasing crack branching for increasing impact velocity. However, for the 3D case, the crack branching occurs for the cracks initiating on the side opposite to the loading side. Here, we do not see crack branching in the curved cracks propagating directly from the circular notch. Figure 5.8 presents the crack patterns at the sections illustrated in Figure 5.6 (b), where the distance is measured from the loading plane. The crack patterns stem from the same time instances as the lowest row in Figure 5.7 for each respective impact velocity. Again, we find a similar trend, with increased crack branching for increasing impact velocity. In their work, Hofacker and Miehe [61] performed the same numerical experiment with en element size of ~1.0 mm × 1.0 mm × 1.0 mm with $l = 2.0$ mm using a loading velocity of 5 m/s. With those conditions, they did not predict crack initiation from the back side of the specimen. However, the curved crack path propagating from the notch is similar to what is observed in our work for the same loading velocity. This deviation is most likely related to the difference in element size and length scale.
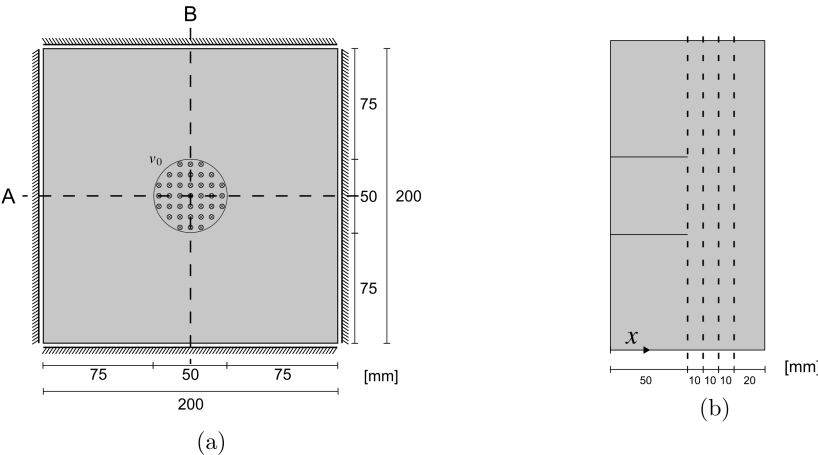
Figure 5.6: (a) The 3D extension of the Kalthoff-Winkler specimen seen from the front with dimensions and boundary conditions. (b) The side-view of symmetry plane B with the section planes used in visualization of the crack pattern.
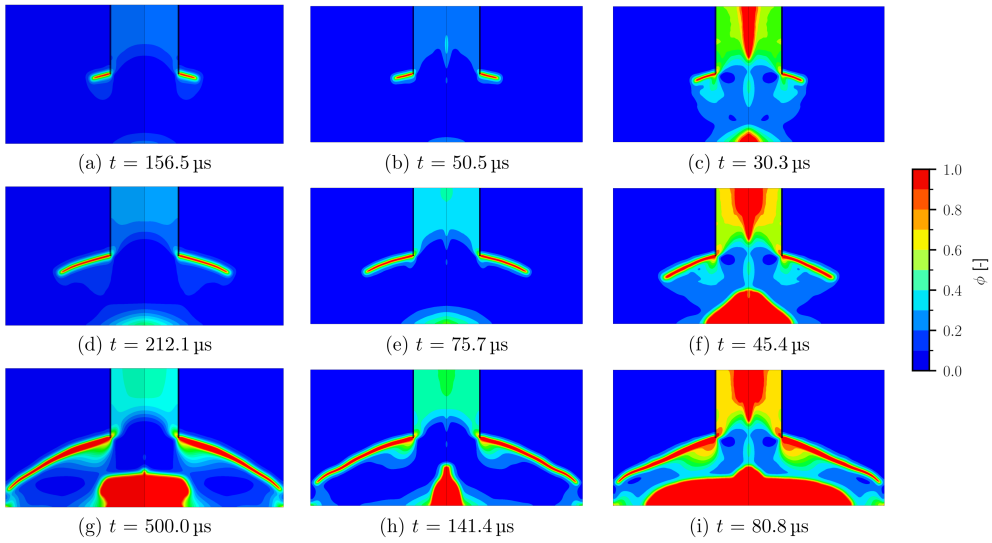
Figure 5.7: Crack pattern evolution seen from the side-view of symmetry plane B, see Figure 5.6 (a), for numerical experiments of the Kalthoff-Winkler test with impact velocities of 5 m/s (a,d,g), 16.5 m/s (b,e,h) and 50 m/s (c,f,i).
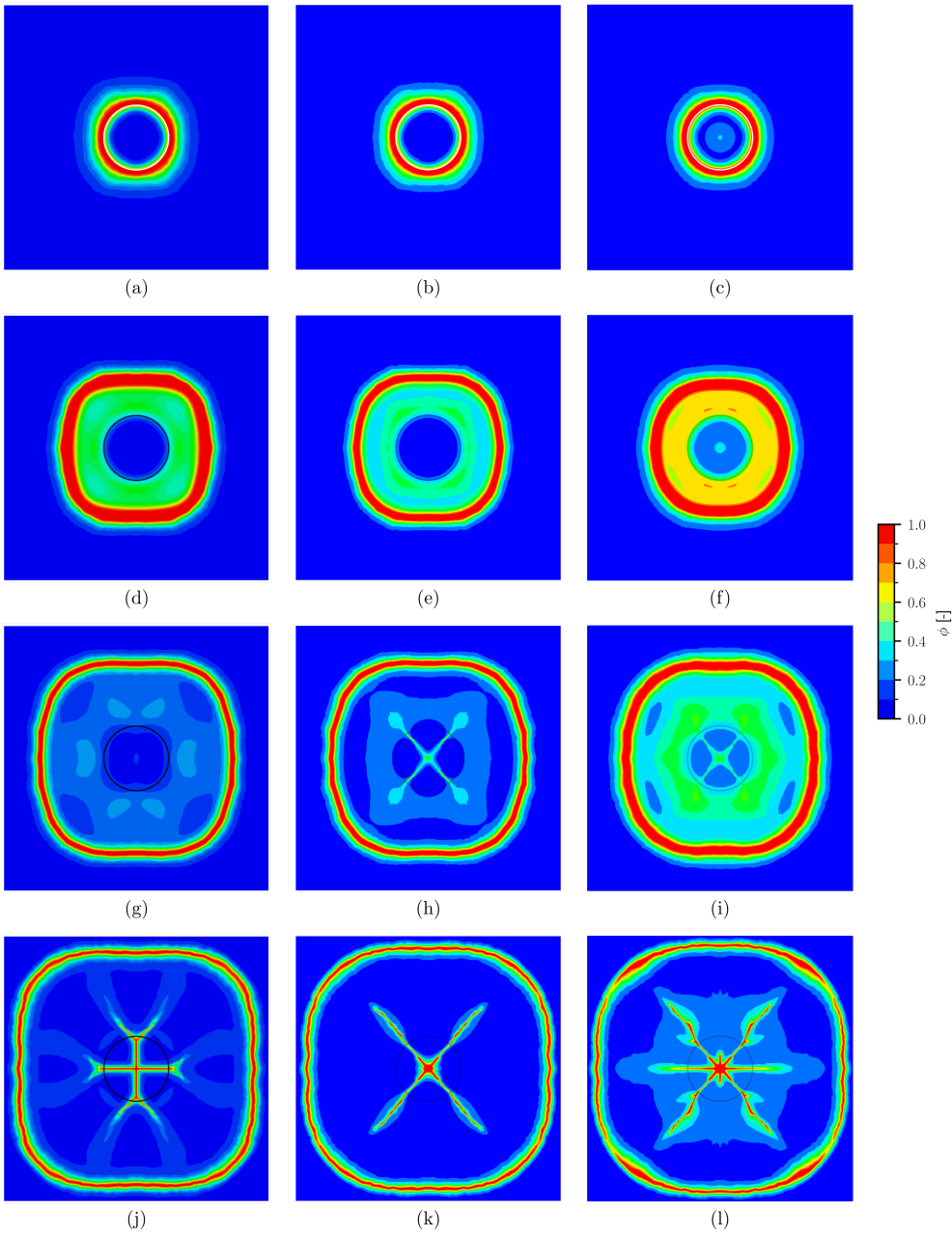
Figure 5.8: The section views presented in Figure 5.6 (b) of the nearly fully evolved crack pattern for numerical experiment of the 3D extension of the Kalthoff-Winkler test with an impact velocity of 5 m/s (a,d,g,j), 16.5 m/s (b,e,h,k) and 50 m/s (c,f,i,l) at $x = 50$ mm (a-c), $x = 60$ mm (d-f), $x = 70$ mm (g-i) and $x = 80$ mm (j-l).

5.4 L-shape tests

Rudshaug et al. [161] performed 20 experiments on L-shaped soda-lime glass specimens subjected to quasi-static loading. For each experiment, the crack propagation was captured using high-speed cameras. Figure 5.9 (a) presents the experimental setup, where the top of the specimen is clamped and pulled upwards, while the right-hand-side is restrained using a tie-strap. Figure 5.12 (f) presents the resulting crack paths colored by crack propagation speed and Figure 5.12 (c) presents the evolution of the crack propagation speed. The crack propagation paths were consistent and the force level at fracture initiation varied from ~75 N to ~115 N. The experimental study revealed a positive correlation between the force level at fracture initiation and the initial crack propagation speed. We aim to investigate if we are able to capture the trends seen in the experimental study performed by Rudshaug et al. [161] using our dynamic fracture phase-field implementation in LS-DYNA. To consider the different force levels at fracture initiation, we select two critical principal stress values at which we trigger the fracture phase-field evolution and investigate how this influences the predicted crack propagation both in terms of crack propagation speed and path.
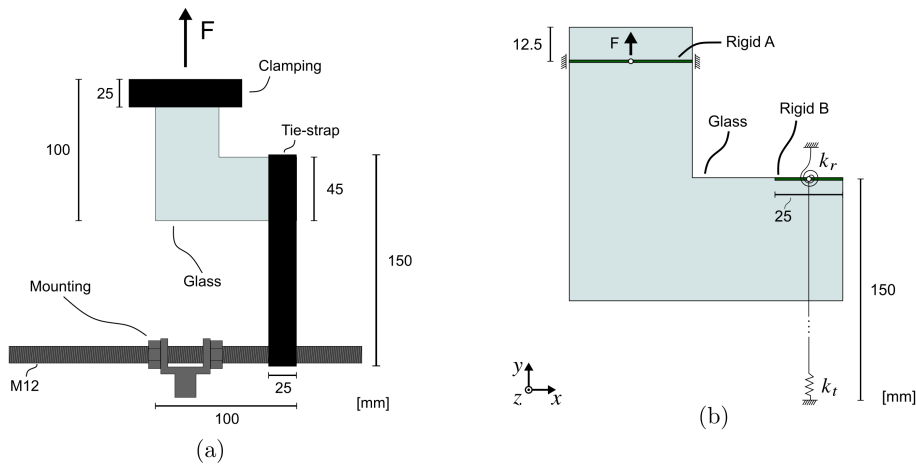
Figure 5.9: The experimental setup (a) and the boundary conditions used in the numerical experiment (b) on the L-shaped glass specimen. Two rigid parts (A and B) are used to model the boundary conditions of the experiment. A translational spring with stiffness k_t and a rotational spring with stiffness k_r are used to reduce the translational and rotational movement of rigid part B.

The applied boundary conditions are presented in Figure 5.9 (b). Two rigid parts (A and B) are used to model the boundary conditions of the experiment. Both the rigid parts are attached to the glass elements through coincident nodes. Rigid part A is restrained in the x- and z-directions, not allowed to rotate about any axis, and prescribed a displacement in the positive y-direction. Rigid part B is restrained in the z-direction and not allowed to rotate about the x and y axis. Rigid part B is connected to a translational spring with stiffness k_t reducing displacement in the x- and

y-directions and a rotational spring with stiffness k_r reducing rotation about the z axis. Both springs are connected to the mass center of rigid part B and are used to replicate the behavior of the tie-strap. The spring stiffness values are $k_t = 38.0\,\text{N/mm}$ and $k_r = 4750.0\,\text{N mm}$, based on the reported spring stiffness from Rudshaug et al. [161].

The model parameters are: density $\rho = 2500\,\text{kg/m}^3$, Young's modulus $E = 70\,\text{GPa}$, Poisson ratio $\nu = 0.23$, critical energy release rate $G_c = 8\,\text{J/m}^2$, length scale $l = 0.4\,\text{mm}$, artificial residual stiffness $k = 0$ and phase-field viscosity $\eta = 10^{-9}\,\text{N s/mm}^2$. We discretized the L-shaped specimen in two ways, presented in Table 5.1.

Table 5.1: Discretizations of the L-shaped glass specimen.

Element type	Number of elements	Element dimensions
Shell elements (plane stress)	174 375	$0.2\,\text{mm} \times 0.2\,\text{mm}$
Solid elements	1 569 375	$0.2\,\text{mm} \times 0.2\,\text{mm} \times 0.2\,\text{mm}$

To determine the critical principal stress values, σ_c, at the minimum and maximum load level at fracture initiation, we performed a failure-free linear elastic version of the numerical experiment for each discretization and noted the maximum values of the major principal stress at the respective critical force levels seen in the experiments. We note that these values differ depending on the discretization.

Figures 5.10 and 5.11 present the predicted crack paths using shell and solid elements, respectively. We note that the predicted crack paths are nearly identical. The initial crack propagation angle resembles what was found in the experiments. However, for both the weak and strong specimens we note that the inclination of the crack propagation path towards the left-hand-side of specimen deviates from the experimental paths, see Figure 5.12 (f). We also note that the crack paths from the numerical experiments using the Miehe split are less curved than those based on the Amor and hybrid splits.
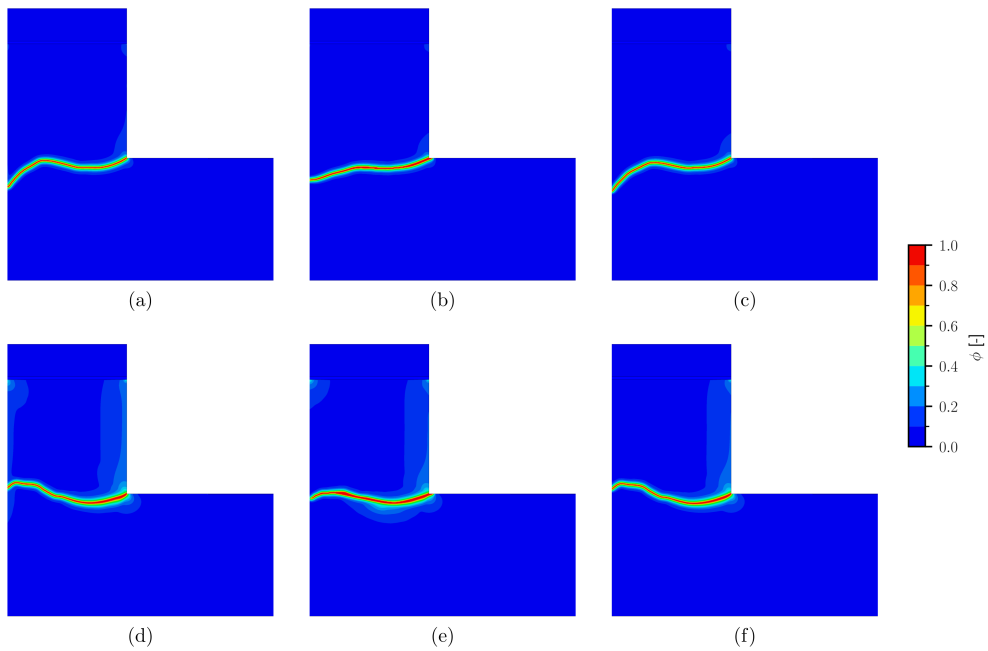
Figure 5.10: Crack patterns for numerical experiments with shell elements of the weakest (a-c) and strongest (d-f) L-shaped glass specimen using the Amor (a,d), Miehe (b,e) and hybrid (c,f) splits.
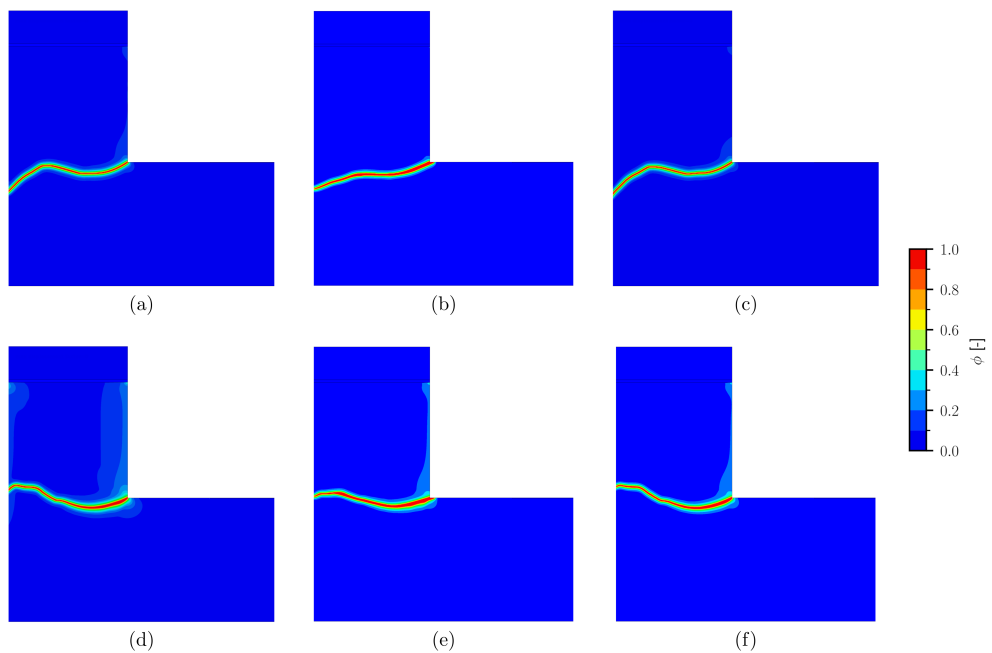
Figure 5.11: Crack patterns for numerical experiments with solid elements of the weakest (a-c) and strongest (d-f) L-shaped glass specimen using the Amor (a,d), Miehe (b,e) and hybrid (c,f) splits.

The evolution of the crack propagation speed and path for the shell element simulations are presented in Figure 5.12 (a-b) and (d-e), comparing the three tension-compression splits for the weak (a,d) and strong (b,e) specimen. The propagation speeds are similar for all splits, except from ~60 µs and later for the strong specimen with the Miehe split. We note that the initial crack propagation speeds for both the weak (~800–1000 m/s) and strong (~1500 m/s) specimen are close to the experimental values. However, in both cases the crack propagation speed drops too quickly compared to what was seen in the experiments. Similar to what we noted from Figures 5.10 and 5.11, Figure 5.12 (d-e) confirms that the Miehe split results in less curved crack paths. The evolutions were identical for the solid element simulations, however, the computational time increased drastically.
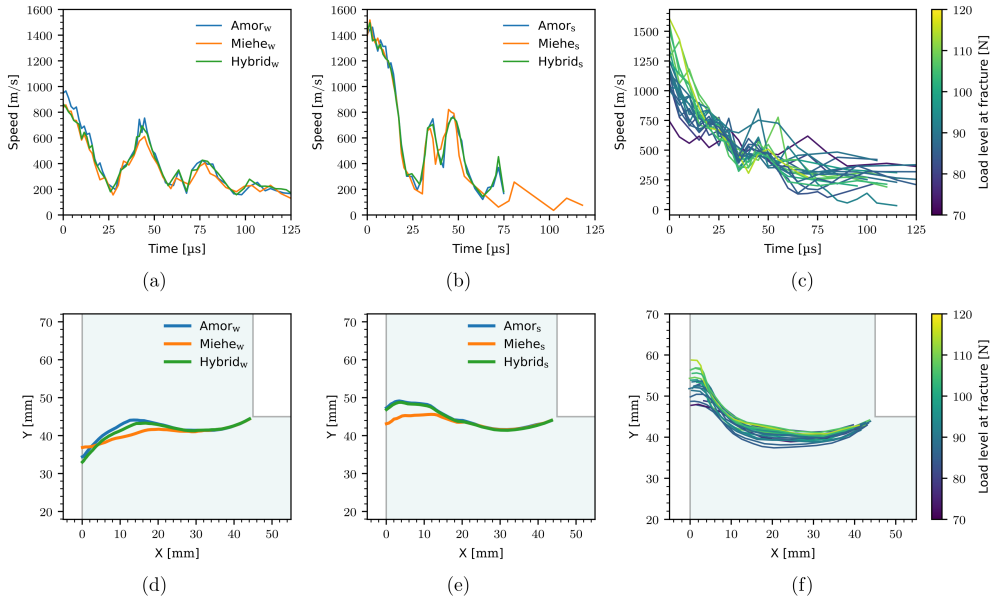
Figure 5.12: Crack propagation speed (a-c) and path (d-f) for numerical experiments with shell elements of the weakest (a,d) and strongest (b,e) L-shaped glass specimen and the experiments (c,f).

5.5 Discussion

Our implementation of the fracture phase-field approach was validated for static and dynamic problems. All the specimens used in the validations were discretized using regular hexahedral solid elements. The numerical experiments of the SENT, SENS and Kalthoff-Winkler tests all resulted in smooth curved crack propagation paths, indicating that there is no pathological mesh dependence. Both the SENT and SENS tests resulted in crack paths resembling what was found by Miehe et al. [54] and Ambati et al. [158], indicating a successful implementation. Furthermore, the dynamic version of the implementation was validated against different versions of the Kalthoff-Winkler tests. When comparing the resulting crack patterns to what was found by Hofacker and Miehe [61], it is clear that the implementations is able to handle dynamic cracking phenomena like crack branching.

The dynamic fracture phase-field was implemented in the commercial FE solver LS-DYNA, solving the displacement field and fracture phase-field separately in a staggered fashion. The displacement field is updated explicitly, while the fracture phase-field increment is solved implicitly. The lack of a temporal dependency (except for the stabilizing viscosity parameter η) in the fracture phase-field evolution equation, see Equation (5.14), implies that the field is fully evolved at every increment. Instead of applying an iteration scheme, we approximate the incremental change in the phase-field by a linear system of equations. As discussed in [158], the staggered solution scheme

requires sufficiently small increments to achieve convergence. In this explicit FE framework, this requirement is normally met, but care must be taken if time scaling is used, as this effectively increases the increment size and affects the viscous term $\eta\dot{\phi}$ in Equation (5.14).

The length scale parameter, l, may be referred to as the width of the regularized crack. To properly represent the diffuse approximation of the sharp crack topology, we need a sufficiently fine discretization that is able to adequately resolve the length scale parameter. In the case of brittle fracture, the length scale tends to zero. This implies that a very fine discretization is necessary to properly predict brittle crack propagation. However, a length scale close to zero is not practically feasible. For this reason, the length scale is typically way bigger than the physical crack width. A consequence of a large length scale is that the degradation of the potential energy is overestimated, decreasing the crack propagation speed.

With the new proposed crack driving force in Equation (5.16), we introduced a global fracture initiation criterion based on the maximum major principal stress $\sigma_{\mathcal{B}}$. To ensure fracture initiation at the correct load levels in the numerical experiments on the L-shaped specimens, we had to determine the appropriate critical principal stress values σ_c through initial damage-free simulations. Depending on the specimen discretization, the stress representation near the inner corner will vary. Because of the location of the integration points, we do not sample directly at the inner corner, but at a distance. For this reason, the critical principal stress values change for both different discretizations and distributions of integration points. However, when we ensure fracture initiation at the same critical load level, we find that this does not affect the crack propagation path and speed. This is confirmed when comparing the shell to the solid element simulations.

For the quasi-static SENT and SENS tests and the L-shaped glass tests we conducted the simulations using the three implemented tension-compression splits, namely the Amor, Miehe and hybrid splits. The splits all produced the same crack pattern for the SENT test, which was expected. However, for the SENS test and the L-shaped glass specimen test we see some variations. The crack path of the SENS test with the Amor split exhibits a gradual ramp down from the initial crack, while the two other splits result in a crack path that propagates directly downwards. In addition, a small crack starts growing from the lower right corner in the SENS test with the Amor split. If we consider the L-shaped glass tests, we note that the predicted crack paths of the Amor and hybrid splits are similar, while the crack path of the Miehe split is less curved. These examples illustrate that the tension-compression splits impact the crack propagation paths, and that their corresponding predictions might coincide from some problems and deviate for others.

When we consider the crack propagation speed in the simulations of both the weak and strong L-shaped specimens (Figure 5.12 (a-b)), we note that the initial crack propagation speed is similar to what was reported in the experiments (Figure 5.12 (c)). This indicates that the initial crack propagation speed is correlated to the critical load level, and thus the amount of potential energy at fracture. In addition, it implies that the new proposed crack driving force in Equation (5.16) is suited for handling crack propagation at various critical load levels. Unlike what was observed in the experiments, the crack paths for the weak specimen propagates downwards close to the left edge. This downward propagation might be linked to the applied boundary conditions. However,

it might also deviate due to the early drop in crack propagation speed. When the crack propagation speed is too low, it affects the resulting concurrent stress fields, which may result in different optimal crack paths.

By implementing the fracture phase-field into a commercial FE code we get access to a well established and full featured FE framework. This makes it easy to use the dynamic phase-field formulation in complex simulations involving advanced contact formulations, fluid structure interaction and ballistics, which are not common features in in-house codes. With these additional options, including the new proposed crack driving force, we facilitate further validation and investigation of the potential of the phase-field approach to fracture.

5.6   Conclusion

In this work we implemented a dynamic fracture phase-field formulation into the commercial FE code LS-DYNA through both solid and shell user elements. The fracture phase-field evolution was solved with a staggered explicit update of the displacement field and implicit update of the fracture phase-field. The implementation proved capable of simulating complex, dynamic crack topologies through static and dynamic numerical experiments using known numerical examples. We introduced a new crack driving force including a fracture initiation criterion based on the critical major principal stress, that allows for crack predictions for specimens of varying strength. The prediction capacity of the model was tested on quasi-statically loaded L-shaped soda-lime glass specimens of two different specimen strengths. We compared the predicted crack propagations of the numerical simulations to the experiments in terms of path and speed, and found that the predicted initial crack propagation speed is close to the experimental values, but that the speed drops too quickly. The predicted crack paths initially resemble the experimental crack paths, but start to deviate with time as the crack propagates towards the left-hand side. Similar to what was observed in the experiments, the strongest specimen experienced a greater initial crack propagation speed than the weaker one.

6   Conclusions and Further Work

6.1   Conclusions

The objective of the thesis work was to answer the following research question:

How to predict fracture initiation and crack propagation in soda-lime glass?

To answer the twofold research question, the thesis was divided into two main parts, one focusing on fracture initiation, where the aim was to improve the Glass Strength Prediction Model (GSPM) (Paper I and Paper II), and one focusing on crack propagation (Paper III and Paper IV), where the aim was to establish a numerical method that can capture the violent crack propagation behavior of glass. The two parts consist of an experimental and numerical study, where the experimental results were used to validate the numerical models. The main conclusions of the thesis are:

- The experimental setup for quasi-static testing on windshields proved to be both reliable and to allow for detailed extraction of important data for numerical validation, such as loading and deformation histories and crack propagation data. The setup was used to generate a detailed database on three experimental test series based on windshields of varying geometries and production methods.

- The improved version of the GSPM including sub-critical crack growth (SCG) proved capable of handling rate- and size-effects through extensive validation. The new material model version of the GSPM implemented in the LS-DYNA finite element solver was successfully used to replicate the behavior of a weak and strong windshield from the experiments.

- The experimental setup for L-shaped glass specimens resulted in reliable crack propagation data for the crack path and speed for varying critical load levels. The setup generated a database based on 20 experiments of L-shaped specimen of varying strength, and revealed a positive correlation between the initial crack propagation speed and the critical load level. A correlation between the crack propagation path and the critical load level was also found.

- The implemented fracture phase-field models with three tension-compression splits and a new crack driving force proved capable of capturing the initial crack propagation speed for the lowest and highest critical load levels seen in the experiments. However, the crack propagation speed dropped too quickly compared to the experiments, potentially leading to deviations from the experiments in the final part of the predicted crack path.

Overall, this work has pushed the field of glass modeling one step further by providing new insights through two experimental studies and development of numerical models. The introduction of a solver integrated version of the GSPM, which can trigger other existing fracture models, lowers the bar for incorporating the stochastic behavior of glass fracture in modern design processes where FE simulations are involved. Furthermore, the introduction of a new crack driving force for the phase-field approach to fracture proved it possible to predict the initial crack propagation speeds for varying critical load levels. This work has taken us one step closer to finding a good answer to the research question. Hopefully, it will inspire new and extended research in the field of glass modeling.

6.2 Further work

The work presented in this thesis has provided important insights and new numerical tools related to modeling of glass fracture. However, there are many potential topics and studies that can further improve both the understanding of glass fracture and the presented numerical tools. Some of them are listed here sorted in categories related to the thesis chapters:

6.2.1 Experiments on windshields

- New experimental studies with varying loading rate would be interesting. Higher loading rates will result in a stiffer polyvinyl butyral (PVB) behavior and stronger glass layers.

- Characterization of the mechanical behavior of PVB was not a focus of this thesis; however, effort should be put into investigating how the PVB is affected by the autoclave process in the windshield production.

- In the experimental study in Chapter 2 (Paper I), it was observed that the camera placement as well as the temporal resolution of the high-speed footage had a great influence on which cracks that were visible and the detail level of the crack propagation data. In future studies it would be interesting to use more high-speed cameras with better temporal resolution. To improve the accuracy of the pose estimation used in the tracking of the crack propagation it is recommended to add more optical targets.

6.2.2 Glass Strength Prediction Model

- In the current version of the GSPM, both surfaces of the glass plate are provided artificial flaws based on the same parameters. However, it has been found that the tin side of the plate is weaker than the air side. In addition, for curved plates, like windshields, the difference in flaw distribution may increase further. For this reason, an extension of the GSPM that enables different flaw distributions for the different surfaces would be interesting.

- The quality of the GSPM calibration and validation is highly dependent on large high quality experimental databases that sufficiently map the stochastic behavior of the glass specimen. To increase the credibility of the model predictions, we encourage new experimental studies.

- The flaw statistics generated from the Fourier ptychographic microscopy (FPM) setup for flaw characterization in [64] indicate that some of the assumptions in the GSPM are questionable, such as the assumed uniform spatial flaw distribution and non-interacting flaws. Effort should be put into investigating the impact this has on the model predictions.

6.2.3   Experiments on L-shaped specimens

- A polymer tie-down strap was used to restrain the right-hand-side of the L-shaped specimen in the experiments presented in Chapter 4 (Paper III). Since the strap is much softer than the glass specimen, it governs the total displacement measured in the experiment. In addition, the strap requires careful positioning for each test repetition. In future similar studies with L-shaped glass specimen, we recommend manufacturing a rigid steel component to restrain the right-hand-side. In this way, the measured displacement is governed by the glass specimen and it is easier to ensure repeatability.

- The high-speed cameras used in the experimental study enabled a frame rate of 200 000 fps, resulting in ~25 sampling points per test. For future studies, it would be interesting to increase the temporal resolution such that more sampling points are gathered. This will result in more detailed crack propagation data.

- It would be interesting to apply the Digital Gradient Sensing (DGS) method to also quantify the stress intensity factors and energy release rate during the crack propagation.

6.2.4   Phase-field approach to fracture

- A study on the effect of the length scale on the crack propagation speed would be very interesting. Such a study can both quantify the influence of the length scale and provide guidelines for an upper threshold for the element size in order to predict a realistic crack propagation.

- The implementation of the fracture phase-field model in a general purpose finite element (FE) solver provides many possible new applications for the fracture model. Effort should be put into verifying the phase-field approach in advanced contact problems such as ballistics. Studies including the phase-field approach in fluid-structure interaction simulations would also be interesting.

- Future studies should investigate how alternative fracture models, such as Eigenfracture and the Extended Finite Element Method (XFEM), perform in terms of mesh dependency and crack propagation speed compared to the presented phase-field approach to fracture.

References

[1] Geneva: World Health Organization. *Global status report on road safety 2018: Summary*. 2018. URL: https://www.who.int/publications/i/item/WHO-NMH-NVI-18.20.

[2] *Road traffic injuries*. URL: https://www.who.int/news-room/fact-sheets/detail/road-traffic-injuries.

[3] J R Crandall. "Designing road vehicles for pedestrian protection". In: *BMJ* 324.7346 (May 11, 2002), pp. 1145–1148. ISSN: 09598138, 14685833. DOI: 10.1136/bmj.324.7346.1145. (Visited on 07/18/2022).

[4] Dietmar Otte, Michael Jänsch, and Carl Haasper. "Injury protection and accident causation parameters for vulnerable road users based on German In-Depth Accident Study GIDAS". In: *Accident Analysis & Prevention* 44.1 (2012). Safety and Mobility of Vulnerable Road Users: Pedestrians, Bicyclists, and Motorcyclists, pp. 149–153. ISSN: 0001-4575. DOI: 10.1016/j.aap.2010.12.006.

[5] John B. Wachtman, W. Roger Cannon, and M. John Matthewson. *Mechanical Properties of Ceramics*. Vol. 9. 11. 2009. ISBN: 978-0-470-45151-9. DOI: 10.1002/9780470451519.

[6] Luigi Biolzi, Sara Cattaneo, Maurizio Orlando, Lorenzo Ruggero Piscitelli, and Paolo Spinelli. "Post-failure behavior of laminated glass beams using different interlayers". In: *Composite Structures* 202 (2018), pp. 578–589. ISSN: 02638223. DOI: 10.1016/j.compstruct.2018.03.009.

[7] Martin Larcher and George Solomos. *Laminated glass loaded by air blast waves Experiments and numerical simulations*. Tech. rep. PUBSY JRC 57559. 2010. URL: https://www.researchgate.net/profile/Martin-Larcher/publication/264511670_Laminated_glass_loaded_by_air_blast_waves_-_Experiments_and_numerical_simulations/links/53f597750cf22be01c3f8950/Laminated-glass-loaded-by-air-blast-waves-Experiments-and-numerical-simulations.pdf.

[8] Martin Larcher, George Solomos, Folco Casadei, and Norbert Gebbeken. "Experimental and numerical investigations of laminated glass subjected to blast loading". In: *International Journal of Impact Engineering* 39.1 (2012), pp. 42–50. ISSN: 0734743X. DOI: 10.1016/j.ijimpeng.2011.09.006.

[9] Matthias Haldimann. "Fracture strength of structural glass elements: analytical and numerical modelling, testing and design". PhD thesis. Jan. 1, 2006. DOI: 10.5075/epfl-thesis-3671.

[10] *Automotive Processes*. URL: https://www.pilkington.com/en-gb/uk/automotive/original-equipment/automotive-glazing/automotive-processes.

[11] S. T. Gulati et al. "Measurement of Biaxial Strength of New vs. Used Windshields". In: *International Body Engineering Conference & Exposition*. SAE International, Oct. 2000. DOI: 10.4271/2000-01-2721.

[12] Marc Vandebroek, Christian Louter, Robby Caspeele, Frank Ensslen, and Jan Belis. "Size effect model for the edge strength of glass with cut and ground edge finishing". In: *Engineering structures* 79 (2014), pp. 96–105. DOI: 10.1016/j.engstruct.2014.08.004.

[13] Marc Vandebroek, Jan Belis, Christian Louter, and Robby Caspeele. "Influence of the load history on the edge strength of glass with arrised and ground edge finishing". In: *Engineering Fracture Mechanics* 104 (2013), pp. 29–40. ISSN: 00137944. DOI: 10.1016/j.engfracmech.2013.03.016.

[14] Karoline Osnes, Odd Sture Hopperstad, and Tore Børvik. "Rate dependent fracture of monolithic and laminated glass: Experiments and simulations". In: *Engineering Structures* 212 (2020), p. 110516. ISSN: 0141-0296. DOI: 10.1016/j.engstruct.2020.110516.

[15] Alan Arnold Griffith. "The phenomena of rupture and flow in solids". In: *Phil Trans Roy Sot Lon (Series A)* 221 (1921), pp. 163–198. URL: https://mbarkey.eng.ua.edu/courses/AEM644/Griffith1921fracture.pdf.

[16] G.R. Irwin. *ONSET OF FAST CRACK PROPAGATION IN HIGH STRENGTH STEEL AND ALUMINUM ALLOYS:* Fort Belvoir, VA: Defense Technical Information Center, 1956. DOI: 10.21236/AD0099305.

[17] G. R. Irwin. "Analysis of Stresses and Strains Near the End of a Crack Traversing a Plate". In: *Journal of Applied Mechanics* 24.3 (1957), pp. 361–364. ISSN: 0021-8936. DOI: 10.1115/1.4011547.

[18] T.L. Anderson. *Fracture Mechanics*. 3rd ed. 2005. ISBN: 978-1-4200-5821-5.

[19] Charles R. Kurkjian, Prabhat K. Gupta, and Richard K. Brow. "The Strength of Silicate Glasses: What Do We Know, What Do We Need to Know?" In: *International Journal of Applied Glass Science* 1.1 (2010), pp. 27–37. ISSN: 2041-1294. DOI: 10.1111/j.2041-1294.2010.00005.x.

[20] M. Overend and K. Zammit. "A computer algorithm for determining the tensile strength of float glass". In: *Engineering Structures* 45 (2012), pp. 68–77. ISSN: 01410296. DOI: 10.1016/j.engstruct.2012.05.039.

[21] J. E. Ritter Jr. and C. L. Sherburne. "Dynamic and Static Fatigue of Silicate Glasses". In: *Journal of the American Ceramic Society* 54.12 (1971), pp. 601–605. ISSN: 1551-2916. DOI: 10.1111/j.1151-2916.1971.tb16013.x.

[22] H. C. Chandan, R. C. Bradt, and G. E. Rindone. "Dynamic Fatigue of Float Glass". In: *Journal of the American Ceramic Society* 61.5 (1978), pp. 207–210. ISSN: 1551-2916. DOI: 10.1111/j.1151-2916.1978.tb09280.x.

[23] S. M. Wiederhorn. "Influence of Water Vapor on Crack Propagation in Soda-Lime Glass". In: *Journal of the American Ceramic Society* 50.8 (1967), pp. 407–414. ISSN: 1551-2916. DOI: 10.1111/j.1151-2916.1967.tb15145.x.

[24] E Orowan. "Fracture and strength of solids". In: *Reports on Progress in Physics* 12.1 (1949), pp. 185–232. ISSN: 00344885. DOI: 10.1088/0034-4885/12/1/309.

[25] J. E. Shelby. *Introduction to glass science and technology*. 2nd. Cambridge: Royal Society of Chemistry, 2005. 291 pp. ISBN: 978-0-85404-639-3. URL: https://belglas.files.wordpress.com/2021/01/shelbyj.e.introductiontoglassscienceandtechnology2nded.rsc20050854046399.pdf.

REFERENCES

[26]   R. J. Charles. "Static Fatigue of Glass. I". In: *Journal of Applied Physics* 29.11 (1958-11), pp. 1549–1553. ISSN: 0021-8979, 1089-7550. DOI: 10.1063/1.1722991.

[27]   R. J. Charles. "Static Fatigue of Glass. II". In: *Journal of Applied Physics* 29.11 (1958-11), pp. 1554–1560. ISSN: 0021-8979, 1089-7550. DOI: 10.1063/1.1722992.

[28]   R. J. Charles. "Dynamic Fatigue of Glass". In: *Journal of Applied Physics* 29.12 (1958), pp. 1657–1662. ISSN: 0021-8979, 1089-7550. DOI: 10.1063/1.1723019.

[29]   S. M. Wiederhorn and L. H. Bolz. "Stress Corrosion and Static Fatigue of Glass". In: *Journal of the American Ceramic Society* 53.10 (1970), pp. 543–548. ISSN: 1551-2916. DOI: 10.1111/j.1151-2916.1970.tb15962.x.

[30]   Matteo Ciccotti. "Stress-corrosion mechanisms in silicate glasses". In: *Journal of Physics D: Applied Physics* 42.21 (2009-10), p. 214006. ISSN: 0022-3727. DOI: 10.1088/0022-3727/42/21/214006.

[31]   Cenk Kocer and Richard E. Collins. "Measurement of Very Slow Crack Growth in Glass". In: *Journal of the American Ceramic Society* 84.11 (2001), pp. 2585–2593. ISSN: 1551-2916. DOI: 10.1111/j.1151-2916.2001.tb01058.x.

[32]   D. Maugis. "Subcritical crack growth, surface energy, fracture toughness, stick-slip and embrittlement". In: *Journal of Materials Science* 20.9 (1985), pp. 3041–3073. ISSN: 0022-2461, 1573-4803. DOI: 10.1007/BF00545170.

[33]   Christopher Brokmann. *A Model for the Stochastic Fracture Behavior of Glass and Its Application to the Head Impact on Automotive Windscreens*. Vol. 63. Mechanik, Werkstoffe und Konstruktion im Bauwesen. Wiesbaden: Springer Fachmedien Wiesbaden, 2022. ISBN: 978-3-658-36787-9 978-3-658-36788-6. DOI: 10.1007/978-3-658-36788-6.

[34]   J. H. Nielsen, J. F. Olesen, and H. Stang. "The Fracture Process of Tempered Soda-Lime-Silica Glass". In: *Experimental Mechanics* 49.6 (2009), pp. 855–870. ISSN: 0014-4851, 1741-2765. DOI: 10.1007/s11340-008-9200-y.

[35]   S Dondeti and HV Tippur. "A comparative study of dynamic fracture of soda-lime glass using photoelasticity, digital image correlation and digital gradient sensing techniques". In: *Experimental Mechanics* 60.2 (2020), pp. 217–233. DOI: 10.1007/s11340-019-00549-5.

[36]   S Dondeti and HV Tippur. "A comparative study of dynamic fracture of soda-lime glass using photoelasticity, digital image correlation and digital gradient sensing techniques". In: *Experimental Mechanics* 60.2 (2020), pp. 217–233. DOI: 10.1007/s11340-019-00549-5.

[37]   Hwun Park and Weinong W. Chen. "Experimental Investigation on Dynamic Crack Propagating Perpendicularly Through Interface in Glass". In: *Journal of Applied Mechanics* 78.5 (2011), p. 051013. ISSN: 0021-8936, 1528-9036. DOI: 10.1115/1.4004283.

[38]   H. Schardin. "Velocity Effects in Fracture". In: *Fracture: Proceeding of an International Conference on the Atomic Mechanism of Fracture Help in Swampscott, Massachusetts* (1959).

[39]   David Z. Yankelevsky. "Strength prediction of annealed glass plates – A new model". In: *Engineering Structures* 79 (2014), pp. 244–255. ISSN: 0141-0296. DOI: https://doi.org/10.1016/j.engstruct.2014.08.017.

[40] Mahil Pathirana, Nelson Lam, Shihara Perera, Lihai Zhang, Dong Ruan, and Emad Gad. "Risks of failure of annealed glass panels subject to point contact actions". In: *International Journal of Solids and Structures* 129 (2017), pp. 177–194. DOI: 10.1016/j.ijsolstr.2017.09.001.

[41] David T Kinsella and Kent Persson. "A numerical method for analysis of fracture statistics of glass and simulations of a double ring bending test". In: *Glass Structures & Engineering* 3 (2018), pp. 139–152. DOI: 10.1007/s40940-018-0063-z.

[42] David Kinsella and Erik Serrano. "Failure modelling of glass plates in biaxial loading: using flaw-size based weakest-link systems". In: *Glass Structures & Engineering* 6 (2021), pp. 397–424. DOI: 10.1007/s40940-021-00157-7.

[43] Karoline Osnes, Tore Børvik, and Odd Sture Hopperstad. "Shock Tube Testing and Modelling of Annealed Float Glass". In: *EPJ Web of Conferences*. Vol. 183. ISSN: 2100014X. EDP Sciences, 2018. ISBN: 978-2-7598-9053-8. DOI: 10.1051/epjconf/201818301035.

[44] *Global New Car Assessment Programme (NCAP)*. 2023. URL: https://www.globalncap.org/.

[45] Karoline Osnes, Jens Kristian Holmen, Odd Sture Hopperstad, and Tore Børvik. "Fracture and fragmentation of blast-loaded laminated glass: An experimental and numerical study". In: *International Journal of Impact Engineering* 132 (2019). Publisher: Elsevier Ltd. ISSN: 0734743X. DOI: 10.1016/j.ijimpeng.2019.103334.

[46] Bernd Schmidt, Fernando Fraternali, and Michael Ortiz. "Eigenfracture: An Eigendeformation Approach to Variational Fracture". In: *Multiscale Modeling & Simulation* 7.3 (2009), pp. 1237–1266. ISSN: 1540-3459, 1540-3467. DOI: 10.1137/080712568.

[47] A. Pandolfi and M. Ortiz. "An eigenerosion approach to brittle fracture". In: *International Journal for Numerical Methods in Engineering* 92.8 (2012), pp. 694–714. ISSN: 1097-0207. DOI: 10.1002/nme.4352.

[48] A. Pandolfi, K. Weinberg, and M. Ortiz. "A comparative accuracy and convergence study of eigenerosion and phase-field models of fracture". In: *Computer Methods in Applied Mechanics and Engineering* 386 (2021), p. 114078. ISSN: 00457825. DOI: 10.1016/j.cma.2021.114078.

[49] Flavio Stochino, Aurel Qinami, and Michael Kaliske. "Eigenerosion for static and dynamic brittle fracture". In: *Engineering Fracture Mechanics* 182 (2017), pp. 537–551. ISSN: 0013-7944. DOI: 10.1016/j.engfracmech.2017.05.025.

[50] Aurel Qinami, Eric Cushman Bryant, WaiChing Sun, and Michael Kaliske. "Circumventing mesh bias by r- and h-adaptive techniques for variational eigenfracture". In: *International Journal of Fracture* 220.2 (2019), pp. 129–142. ISSN: 1573-2673. DOI: 10.1007/s10704-019-00349-x.

[51] G. A. Francfort and J. J. Marigo. "Revisiting brittle fracture as an energy minimization problem". In: *Journal of the Mechanics and Physics of Solids* 46.8 (1998), pp. 1319–1342. ISSN: 00225096. DOI: 10.1016/S0022-5096(98)00034-9.

[52] B. Bourdin, G. A. Francfort, and J. J. Marigo. "Numerical experiments in revisited brittle fracture". In: *Journal of the Mechanics and Physics of Solids* 48.4 (2000), pp. 797–826. ISSN: 00225096. DOI: 10.1016/S0022-5096(99)00028-9.

REFERENCES

[53]   C. Miehe, F. Welschinger, and M. Hofacker. "Thermodynamically consistent phase-field models of fracture: Variational principles and multi-field FE implementations". In: *International Journal for Numerical Methods in Engineering* 83.10 (2010), pp. 1273–1311. ISSN: 00295981. DOI: 10.1002/nme.2861.

[54]   Christian Miehe, Martina Hofacker, and Fabian Welschinger. "A phase field model for rate-independent crack propagation: Robust algorithmic implementation based on operator splits". In: *Computer Methods in Applied Mechanics and Engineering* 199.45 (2010), pp. 2765–2778. ISSN: 00457825. DOI: 10.1016/j.cma.2010.04.011.

[55]   Blaise Bourdin, Gilles A. Francfort, and Jean-Jacques Marigo. "The variational approach to fracture". In: *Journal of Elasticity* 91 (2008). ISSN: 03743535. DOI: 10.1007/s10659-007-9107-3.

[56]   Charlotte Kuhn and Ralf Müller. "A continuum phase field model for fracture". In: *Engineering Fracture Mechanics* 77.18 (2010), pp. 3625–3634. ISSN: 00137944. DOI: 10.1016/j.engfracmech.2010.08.009.

[57]   C. Kuhn and R. Müller. "A phase field model for fracture". In: *PAMM* 8.1 (2008), pp. 10223–10224. ISSN: 1617-7061. DOI: 10.1002/pamm.200810223.

[58]   Hanen Amor, Jean-Jacques Marigo, and Corrado Maurini. "Regularized formulation of the variational brittle fracture with unilateral contact: Numerical experiments". In: *Journal of the Mechanics and Physics of Solids* 57.8 (2009-08-01), pp. 1209–1229. ISSN: 0022-5096. DOI: 10.1016/j.jmps.2009.04.011.

[59]   Michael J. Borden, Clemens V. Verhoosel, Michael A. Scott, Thomas J.R. Hughes, and Chad M. Landis. "A phase-field description of dynamic brittle fracture". In: *Computer Methods in Applied Mechanics and Engineering* 217-220 (2012), pp. 77–95. ISSN: 00457825. DOI: 10.1016/j.cma.2012.01.008.

[60]   Martina Hofacker and Christian Miehe. "Continuum phase field modeling of dynamic fracture: variational principles and staggered FE implementation". In: *International Journal of Fracture* 178.1 (2012), pp. 113–129. ISSN: 1573-2673. DOI: 10.1007/s10704-012-9753-8.

[61]   M. Hofacker and C. Miehe. "A phase field model of dynamic fracture: Robust field updates for the analysis of complex crack patterns". In: *International Journal for Numerical Methods in Engineering* 93.3 (2013), pp. 276–301. ISSN: 1097-0207. DOI: 10.1002/nme.4387.

[62]   Blaise Bourdin, Christopher J. Larsen, and Casey L. Richardson. "A time-discrete model for dynamic fracture based on crack regularization". In: *International Journal of Fracture* 168.2 (2011), pp. 133–143. ISSN: 03769429. DOI: 10.1007/s10704-010-9562-x.

[63]   H.L. Ren, X.Y. Zhuang, C. Anitescu, and T. Rabczuk. "An explicit phase field method for brittle dynamic fracture". In: *Computers & Structures* 217 (2019), pp. 45–56. ISSN: 00457949. DOI: 10.1016/j.compstruc.2019.03.005.

[64]   K. R. B. Tekseth, J. Rudshaug, M. G. Mayani, M. N. Akram, T. Børvik, and D. W. Breiby. "Mapping surface flaws on float glass through Fourier ptychographic quantitative phase imaging". In: (2023).

[65]   Shuangmei Zhao, Lokeswarappa R Dharani, Li Chai, and Saeed D Barbat. "Analysis of damage in laminated automotive glazing subjected to simulated head impact". In:

Engineering Failure Analysis 13.4 (2006), pp. 582–597. DOI: 10.1016/j.engfailanal.2004.12.038.

[66] C. Brokmann, C. Alter, and S. Kolling. "Experimental determination of failure strength in automotive windscreens using acoustic emission and fractography". In: *Glass Structures & Engineering* 4.2 (2019), pp. 229–241. ISSN: 2363-5142, 2363-5150. DOI: 10.1007/s40940-018-0090-9.

[67] Frederick C Winkelmann. "Modeling windows in EnergyPlus". In: Proceedings of the Seventh International IBPSA Conference. Building Simulation, Jan. 2001. URL: http://www.ibpsa.org/proceedings/bs2001/bs01_0457_464.pdf.

[68] Euro NCAP. *Head Impact*. 2023. URL: https://www.euroncap.com/en/vehicle-safety/the-ratings-explained/vulnerable-road-user-vru-protection/head-impact/.

[69] Gerd Manthei, Christian Alter, and Stefan Kolling. "Localization of initial cracks in laminated glass using acoustic emission analysis—Part I". In: Proceedings of the 31st European Working Group on Acoustic Emission, Dresden, Germany. NDT.net, 2014. URL: https://www.ndt.net/article/ewgae2014/papers/we2a3.pdf.

[70] Christian Alter, Gerd Manthei, Stefan Kolling, and Jens Schneider. "Lokalisierung des initialen Versagens bei Verbundsicherheitsglas unter stoßartiger Belastung". In: *Stahlbau* 84 (S1 2015), pp. 433–442. ISSN: 1437-1049. DOI: 10.1002/stab.201590099.

[71] George D. Quinn. *NIST Recommended Practice Guide: Fractography of Ceramics and Glasses (National Institute of Standards and Technology, Gaithersburg, MD)*. 3rd. NIST Special Publication (SP), 2020. DOI: 10.6028/NIST.SP.960-16e3.

[72] Jun Xu et al. "Experimental and macroscopic investigation of dynamic crack patterns in PVB laminated glass sheets subject to light-weight impact". In: *Engineering Failure Analysis* 18.6 (2011), pp. 1605–1612. ISSN: 13506307. DOI: 10.1016/j.engfailanal.2011.05.004.

[73] Jingjing Chen, Jun Xu, Xuefeng Yao, Xiaoqing Xu, Bohan Liu, and Yibing Li. "Different driving mechanisms of in-plane cracking on two brittle layers of laminated glass". In: *International Journal of Impact Engineering* 69 (2014), pp. 80–85. ISSN: 0734743X. DOI: 10.1016/j.ijimpeng.2014.02.014.

[74] K. Osnes, S. Dey, O. S. Hopperstad, and T. Børvik. "On the Dynamic Response of Laminated Glass Exposed to Impact Before Blast Loading". In: *Experimental Mechanics* 59.7 (2019), pp. 1033–1046. ISSN: 17412765. DOI: 10.1007/s11340-019-00496-1.

[75] Chiara Bedon et al. "Performance of structural glass facades under extreme loads – Design methods, existing research, current issues and trends". In: *Construction and Building Materials* 163 (2018). Publisher: Elsevier Ltd, pp. 921–937. ISSN: 09500618. DOI: 10.1016/j.conbuildmat.2017.12.153.

[76] Xihong Zhang, Hong Hao, and Zhongqi Wang. "Experimental study of laminated glass window responses under impulsive and blast loading". In: *International Journal of Impact Engineering* 78 (2015). Publisher: Elsevier Ltd, pp. 1–19. ISSN: 0734743X. DOI: 10.1016/j.ijimpeng.2014.11.020.

[77] J. Pelfrene, J. Kuntsche, S. Van Dam, W. Van Paepegem, and J. Schneider. "Critical assessment of the post-breakage performance of blast loaded laminated glazing: Experiments

and simulations". In: *International Journal of Impact Engineering* 88 (2016). Publisher: Elsevier Ltd, pp. 61–71. ISSN: 0734743X. DOI: 10.1016/j.ijimpeng.2015.09.008.

[78] Charles E. Anderson Jr., Carl E. Weiss, and Sidney Chocron. "Impact Experiments Into Borosilicate Glass at Three Scale Sizes". In: *Journal of Applied Mechanics* 78.5 (2011). ISSN: 0021-8936. DOI: 10.1115/1.4004281.

[79] Charles E. Anderson Jr., Rory P. Bigger, and Carl E. Weiss. "Crack and Damage Velocities in Ballistic Experiments". In: *International Journal of Applied Glass Science* 5.4 (2014), pp. 374–383. ISSN: 2041-1294. DOI: 10.1111/ijag.12091.

[80] Gyu-In Shim, Seong-Hwan Kim, Hyeng-Woo Eom, Deok-Lae Ahn, Jong-Kyoo Park, and Se-Young Choi. "Improvement in ballistic impact resistance of a transparent bulletproof material laminated with strengthened soda-lime silicate glass". In: *Composites Part B: Engineering* 77 (2015), pp. 169–178. ISSN: 1359-8368. DOI: 10.1016/j.compositesb.2015.03.035.

[81] Stephan Bless and Tiffany Chen. "Impact damage in layered glass". In: *International Journal of Fracture* 162.1 (2010), pp. 151–158. ISSN: 1573-2673. DOI: 10.1007/s10704-009-9379-7.

[82] Elmar Strassburger, Steffen Bauer, and Gregor Popko. "Damage visualization and deformation measurement in glass laminates during projectile penetration". In: *Defence Technology*. 28th International Symposium on Ballistics 10.2 (2014), pp. 226–238. ISSN: 2214-9147. DOI: 10.1016/j.dt.2014.05.008.

[83] Wenke Hu, Yenan Wang, Jian Yu, Chian-Fong Yen, and Florin Bobaru. "Impact damage on a thin glass plate with a thin polycarbonate backing". In: *International Journal of Impact Engineering* 62 (2013), pp. 152–165. ISSN: 0734-743X. DOI: 10.1016/j.ijimpeng.2013.07.001.

[84] Karoline Osnes, Jens Kristian Holmen, Tormod Grue, and Tore Børvik. "Perforation of laminated glass: An experimental and numerical study". In: *International Journal of Impact Engineering* 156 (2021), p. 103922. ISSN: 0734-743X. DOI: 10.1016/j.ijimpeng.2021.103922.

[85] Shuhua Zhu, Mingbo Tong, and Yuequan Wang. "Experiment and Numerical Simulation of a Full-Scale Aircraft Windshield Subjected to Bird Impact". In: 50th AIAA/ASME/ASCE/AHS/ASC Structures, Structural Dynamics, and Materials Conference. Palm Springs, California: American Institute of Aeronautics and Astronautics, 2009. ISBN: 978-1-60086-975-4. DOI: 10.2514/6.2009-2575.

[86] Yang Jialing, Cai Xujie, and Wu Cunhao. "Experimental and FEM study of windshield subjected to high speed bird impact". In: *Acta Mechanica Sinica* 19.6 (2003), pp. 543–550. ISSN: 0567-7718, 1614-3116. DOI: 10.1007/BF02484547.

[87] L. Rooij et al. "Pedestrian crash reconstruction using multi-body modeling with geometrically detailed, validated vehicle models and advanced pedestrian injury criteria". In: Proceedings of 18th International Technical Conference on the Enhanced Safety of Vehicles, Held Nagoya, Japan, 19-22 May 2003. National Highway Traffic Safety Administration, 2003. URL: https://trid.trb.org/view/750802.

[88] X Sun and M A Khaleel. "Effects of different design parameters on the stone-impact resistance of automotive windshields". In: *Proceedings of the Institution of Mechanical*

Engineers, Part D: Journal of Automobile Engineering 219.9 (2005), pp. 1059–1067. ISSN: 0954-4070, 2041-2991. DOI: `10.1243/095440705X34784`.

[89] M Timmel, S Kolling, Peter Osterrieder, and PA Du Bois. "A finite element model for impact simulation with laminated glass". In: *International Journal of Impact Engineering* 34.8 (2007), pp. 1465–1478. DOI: `10.1016/j.ijimpeng.2006.07.008`.

[90] T. Pyttel, H. Liebertz, and J. Cai. "Failure criterion for laminated glass under impact loading and its application in finite element simulation". In: *International Journal of Impact Engineering* 38.4 (2011), pp. 252–263. ISSN: 0734743X. DOI: `10.1016/j.ijimpeng.2010.10.035`.

[91] Byunghyun Kang, Sung-wook Moon, Jaeyoung Lim, and Byoung-Ho Choi. "Observation and simulations of an impact on the automotive windshield using the time-dependent dynamic failure criterion". In: *Proceedings of the Institution of Mechanical Engineers, Part D: Journal of Automobile Engineering* 229.7 (2015), pp. 866–874. ISSN: 0954-4070, 2041-2991. DOI: `10.1177/0954407014548738`.

[92] Ángel Segura Santillana, Carlos Arregui Dalmases, and Benito Javier Luzón Narro. "Pedestrian protection head impacts in glass correlation FEM-Test in the new SEAT León". In: *6th BETA CAE International Conference, procedings book*. 2015, pp. 1–12. URL: `https://www.beta-cae.com/events/c6pdf/4A_3_SEAT.pdf`.

[93] Bohan Liu, Tingni Xu, Xiaoqing Xu, Yan Wang, Yueting Sun, and Yibing Li. "Energy absorption mechanism of polyvinyl butyral laminated windshield subjected to head impact: Experiment and numerical simulations". In: *International Journal of Impact Engineering* 90 (2016), pp. 26–36. ISSN: 0734743X. DOI: `10.1016/j.ijimpeng.2015.11.010`.

[94] Na Yang, Jianfeng Wang, Guifan Zhao, Yuan Zhong, and Dafang Wang. "Experimental study of headform–PVB laminated windshield impact". In: *International Journal of Crashworthiness* 21.6 (2016), pp. 521–531. ISSN: 1358-8265, 1754-2111. DOI: `10.1080/13588265.2016.1192758`.

[95] Christian Alter, Stefan Kolling, and Jens Schneider. "An enhanced non–local failure criterion for laminated glass under low velocity impact". In: *International Journal of Impact Engineering* 109 (2017), pp. 342–353. ISSN: 0734743X. DOI: `10.1016/j.ijimpeng.2017.07.014`.

[96] Guizhen Yu et al. "Computation modeling of laminated crack glass windshields subjected to headform impact". In: *Computers & Structures* 193 (2017), pp. 139–154. ISSN: 00457949. DOI: `10.1016/j.compstruc.2017.08.011`.

[97] Ayhan Özçifçi and Fatih Yapici. "Effects of machining method and grain orientation on the bonding strength of some wood species". In: *Journal of Materials Processing Technology* 202.1 (2008), pp. 353–358. ISSN: 09240136. DOI: `10.1016/j.jmatprotec.2007.08.043`.

[98] P. A. Hooper, B. R. K. Blackman, and J. P. Dear. "The mechanical behaviour of poly(vinyl butyral) at different strain magnitudes and strain rates". In: *Journal of Materials Science* 47.8 (2012), pp. 3564–3576. ISSN: 0022-2461. DOI: `10.1007/s10853-011-6202-4`.

[99] 3D Scannertech. *Creaform HandySCAN 3D 700*. 2022. URL: `https://3dscannertech.com/creaform-3d-laser-scanners/creaform-handyscan-3d-700`.

[100] Adept. *Phantom v2511*. 2022. URL: https://www.adept.net.au/cameras/visionresearch/Phantomv2511.shtml.

[101] Photron. *FASTCAM SA1.1*. 2022. URL: https://www.techimaging.com/products/legacy/legacy-high-speed/product/photron-fastcam-sa1-1.

[102] Python. *Python programming language*. 2022. URL: https://www.python.org/.

[103] OpenCV. *Camera Calibration and 3D Reconstruction*. 2022. URL: https://docs.opencv.org/3.4/d9/d0c/group%5C_%5C_calib3d.html.

[104] Adam Paszke et al. "PyTorch: An Imperative Style, High-Performance Deep Learning Library". In: *Advances in Neural Information Processing Systems 32*. Curran Associates, Inc., 2019, pp. 8024–8035. URL: http://papers.neurips.cc/paper/9015-pytorch-an-imperative-style-high-performance-deep-learning-library.pdf.

[105] Eric Marchand, Hideaki Uchiyama, and Fabien Spindler. "Pose Estimation for Augmented Reality: A Hands-On Survey". In: *IEEE Transactions on Visualization and Computer Graphics* 22.12 (2016), p. 2633. DOI: 10.1109/TVCG.2015.2513408.

[106] OpenCV. *Perspective-n-Point (PnP) pose computation*. 2022. URL: https://docs.opencv.org/4.x/d5/d1f/calib3d_solvePnP.html.

[107] Paul J. Blatz and William L. Ko. "Application of Finite Elastic Theory to the Deformation of Rubbery Materials". In: *Transactions of the Society of Rheology* 6.1 (1962), pp. 223–252. ISSN: 0038-0032. DOI: 10.1122/1.548937.

[108] P.A Du Bois, S Kolling, and W Fassnacht. "Modelling of safety glass for crash simulation". In: *Computational Materials Science* 28.3 (2003), pp. 675–683. ISSN: 09270256. DOI: 10.1016/j.commatsci.2003.08.023.

[109] William C. Brown. *A practicable formulation for the strength of glass and its special application to large plates*. National Research Council of Canada. Institute for Research in Construction, 1970, 61 p. DOI: 10.4224/23002290.

[110] W. G. Brown. *A load duration theory for glass design*. National Research Council of Canada. Division of Building Research, 1972. DOI: 10.4224/20374822.

[111] William L Beason. "A failure prediction model for window glass". PhD thesis. Texas Tech University, 1980. URL: https://ttu-ir.tdl.org/handle/2346/10495.

[112] W. Lynn Beason and James R. Morgan. "Glass Failure Prediction Model". In: *Journal of Structural Engineering* 110.2 (1984), pp. 197–212. ISSN: 0733-9445. DOI: 10.1061/(ASCE)0733-9445(1984)110:2(197).

[113] W. Lynn Beason and H. Scott Norville. "Development of a new glass thickness selection procedure". In: *Journal of Wind Engineering and Industrial Aerodynamics* 36 (1990), pp. 1135–1144. ISSN: 0167-6105. DOI: 10.1016/0167-6105(90)90110-X.

[114] W. Lynn Beason, Terry L. Kohutek, and Joseph M. Bracci. "Basis for ASTM E 1300 Annealed Glass Thickness Selection Charts". In: *Journal of Structural Engineering* 124.2 (1998), pp. 215–221. ISSN: 0733-9445. DOI: 10.1061/(ASCE)0733-9445(1998)124:2(215).

[115] ASTM E ASTM. *1300-07 Standard Practice for Determining Load Resistance of Glass in Buildings*. 2007.

[116]   A. G. Evans and S. M. Wiederhorn. "Proof testing of ceramic materials—an analytical basis for failure prediction". In: *International Journal of Fracture* 10.3 (1974-09-01), pp. 379–392. ISSN: 1573-2673. DOI: 10.1007/BF00035499.

[117]   Anthony C. Fischer-Cripps and Richard E. Collins. "Architectural glazings: Design standards and failure models". In: *Building and Environment* 30.1 (1995), pp. 29–40. ISSN: 03601323. DOI: 10.1016/0360-1323(94)E0026-N.

[118]   M. Overend, G.A.R. Parke, and D. Buhagiar. "Predicting failure in glass-a general crack growth model". In: *Journal of Structural Engineering* 133.8 (2007), pp. 1146–1155. ISSN: 0733-9445. DOI: 10.1061/(ASCE)0733-9445(2007)133:8(1146).

[119]   Waloddi Weibull. "A statistical theory of strength of materials". In: *IVB-Handl.* (1939).

[120]   I. Nurhuda, N.T.K. Lam, E.F. Gad, and I. Calderone. "Estimation of strengths in large annealed glass panels". In: *International Journal of Solids and Structures* 47.18 (2010), pp. 2591–2599. ISSN: 00207683. DOI: 10.1016/j.ijsolstr.2010.05.015.

[121]   F. A. Veer, P. C. Louter, and F. P. Bos. "The strength of annealed, heat-strengthened and fully tempered float glass". In: *Fatigue & Fracture of Engineering Materials & Structures* 32.1 (2009), pp. 18–25. ISSN: 1460-2695. DOI: 10.1111/j.1460-2695.2008.01308.x.

[122]   David Z. Yankelevsky, Kevin Spiller, Jeffrey A. Packer, and Michael V. Seica. "Fracture characteristics of laboratory-tested soda lime glass specimens". In: *Canadian Journal of Civil Engineering* 44.3 (2017), pp. 151–160. ISSN: 0315-1468, 1208-6029. DOI: 10.1139/cjce-2016-0374.

[123]   David Z. Yankelevsky. "Size effect of the modulus of rupture in float glass plates". In: *Structures* 27 (2020), pp. 1637–1645. ISSN: 2352-0124. DOI: 10.1016/j.istruc.2020.08.006.

[124]   Andrew A. Wereszczak, Mattison K. Ferber, and Wayne Musselwhite. "Method for identifying and mapping flaw size distributions on glass surfaces for predicting mechanical response". In: *International Journal of Applied Glass Science* 5.1 (2014), pp. 16–21. ISSN: 20411286. DOI: 10.1111/ijag.12059.

[125]   Jon Bentley and Bob Floyd. "Programming pearls: a sample of brilliance". In: *Communications of the ACM* 30.9 (1987), pp. 754–757.

[126]   Norman Lloyd Johnson, Samuel Kotz, and N. Balakrishnan. *Continuous univariate distributions*. 2nd ed. Wiley series in probability and mathematical statistics. New York: Wiley, 1994. ISBN: 978-0-471-58495-7 978-0-471-58494-0.

[127]   J. C. Newman and I. S. Raju. "An empirical stress-intensity factor equation for the surface crack". In: *Engineering Fracture Mechanics* 15.1 (1981), pp. 185–192. ISSN: 0013-7944. DOI: 10.1016/0013-7944(81)90116-8.

[128]   Nickolay Smirnov. "Table for estimating the goodness of fit of empirical distributions". In: *The annals of mathematical statistics* 19.2 (1948), pp. 279–281.

[129]   Scipy. *Optimization and root finding (scipy.optimize)*. 2023. URL: https://docs.scipy.org/doc/scipy/reference/optimize.html.

[130]   Karoline Osnes, Tore Børvik, and Odd Sture Hopperstad. "Testing and modelling of annealed float glass under quasi-static and dynamic loading". In: *Engineering Fracture Mechanics* 201 (2018), pp. 107–129. ISSN: 00137944. DOI: 10.1016/j.engfracmech.2018.05.031.

REFERENCES

[131]   Jonas Rudshaug and Eyvind Hustvedt Evensen. "Modelling of windshields subjected to quasi-static loading". MA thesis. NTNU, 2019.

[132]   Steinar Liebe Harneshaug and Lars Otto Lofthus Ose. "Modelling of laminated glass". MA thesis. NTNU, 2020.

[133]   Jonas Rudshaug, Odd Sture Hopperstad, and Tore Børvik. "Capturing fracture initiation and crack propagation of car windshields [Accepted for publication in Engineering Fracture Mechanics]". In: (2023).

[134]   Livermore Software Technology (LST), An ANSYS Company. *LS-DYNA Manual Volume II R12*.

[135]   James W Dally. "Dynamic photoelastic studies of fracture". In: *Experimental Mechanics* 19.10 (1979), pp. 349–361. DOI: 10.1007/BF02324250.

[136]   Eran Sharon and Jay Fineberg. "Confirming the continuum theory of dynamic brittle fracture for fast cracks". In: *Nature* 397.6717 (1999), pp. 333–335. DOI: 10.1038/16891.

[137]   Eran Sharon and Jay Fineberg. "Microbranching instability and the dynamic fracture of brittle materials". In: *Physical Review B* 54.10 (1996), p. 7128. DOI: 10.1103/PhysRevB.54.7128.

[138]   Jay Fineberg, Steven P Gross, Michael Marder, and Harry L Swinney. "Instability in the propagation of fast cracks". In: *Physical Review B* 45.10 (1992), p. 5146. DOI: 10.1103/PhysRevB.45.5146.

[139]   Jay Fineberg and M Marder. "Instability in dynamic fracture". In: *Physics Reports* 313.1-2 (1999), pp. 1–108. DOI: 10.1016/S0370-1573(98)00085-4.

[140]   K. Ravi-Chandar. "Dynamic Fracture of Nominally Brittle Materials". In: *International Journal of Fracture* 90.1 (1998), pp. 83–102. ISSN: 1573-2673. DOI: 10.1023/A:1007432017290.

[141]   W. B. Bradley and A. S. Kobayashi. "An investigation of propagating cracks by dynamic photoelasticity". In: *Experimental Mechanics* 10.3 (1970), pp. 106–113. ISSN: 1741-2765. DOI: 10.1007/BF02325114.

[142]   A. S. Kobayashi, B. G. Wade, W. B. Bradley, and S. T. Chiu. "Crack branching in Homalite-100 sheets". In: *Engineering Fracture Mechanics* 6.1 (1974), pp. 81–92. ISSN: 0013-7944. DOI: 10.1016/0013-7944(74)90048-4.

[143]   M Ramulu and AS Kobayashi. "Mechanics of crack curving and branching—a dynamic fracture analysis". In: *International Journal of Fracture* 27 (1985), pp. 187–201. DOI: 10.1007/BF00017967.

[144]   Arkadi Berezovski and Gerard A Maugin. "On the propagation velocity of a straight brittle crack". In: *International journal of fracture* 143.2 (2007), pp. 135–142. DOI: 10.1007/s10704-007-9053-x.

[145]   Chandru Periasamy and Hareesh V. Tippur. "Full-field digital gradient sensing method for evaluating stress gradients in transparent solids". In: *Applied Optics* 51.12 (2012), pp. 2088–2097. ISSN: 2155-3165. DOI: 10.1364/AO.51.002088.

[146]   C. Periasamy and H. V. Tippur. "Measurement of Orthogonal Stress Gradients Due to Impact Load on a Transparent Sheet using Digital Gradient Sensing Method". In: *Experimental Mechanics* 53.1 (2013), pp. 97–111. ISSN: 1741-2765. DOI: 10.1007/s11340-012-9653-x.

[147] Balamurugan M. Sundaram and Hareesh V. Tippur. "Dynamics of crack penetration vs. branching at a weak interface: An experimental study". In: *Journal of the Mechanics and Physics of Solids* 96 (2016), pp. 312–332. ISSN: 0022-5096. DOI: 10.1016/j.jmps.2016.07.020.

[148] Balamurugan M Sundaram and Hareesh V Tippur. "Dynamic fracture of soda-lime glass: A full-field optical investigation of crack initiation, propagation and branching". In: *Journal of the Mechanics and Physics of Solids* 120 (2018), pp. 132–153. DOI: 10.1016/j.jmps.2018.04.010.

[149] Balamurugan M. Sundaram and Hareesh V. Tippur. "Dynamic Crack Branching in Soda-Lime Glass: An Optical Investigation Using Digital Gradient Sensing". In: *Dynamic Behavior of Materials, Volume 1*. Ed. by Jamie Kimberley, Leslie Elise Lamberson, and Steven Mates. Conference Proceedings of the Society for Experimental Mechanics Series. Cham: Springer International Publishing, 2019, pp. 51–56. ISBN: 978-3-319-95089-1. DOI: 10.1007/978-3-319-95089-1_6.

[150] Balamurugan M. Sundaram and Hareesh V. Tippur. "Full-field measurement of contact-point and crack-tip deformations in soda-lime glass. Part-I: Quasi-static Loading". In: *International Journal of Applied Glass Science* 9.1 (2018), pp. 114–122. ISSN: 2041-1294. DOI: 10.1111/ijag.12278.

[151] Balamurugan M. Sundaram and Hareesh V. Tippur. "Full-field measurement of contact-point and crack-tip deformations in soda-lime glass. Part-II: Stress wave loading". In: *International Journal of Applied Glass Science* 9.1 (2018), pp. 123–136. ISSN: 2041-1294. DOI: 10.1111/ijag.12289.

[152] S. Dondeti and H.V. Tippur. "Mixed-mode Dynamic Fracture Parameters for Soda-lime Glass". In: *Theoretical and Applied Fracture Mechanics* (2023), p. 103791. ISSN: 01678442. DOI: 10.1016/j.tafmec.2023.103791.

[153] Jens H Nielsen, John F Olesen, and Henrik Stang. "The fracture process of tempered soda-lime-silica glass". In: *Experimental mechanics* 49.6 (2009), pp. 855–870. DOI: 10.1007/s11340-008-9200-y.

[154] Jingjing Chen et al. "Experimental investigation on the radial and circular crack propagation of PVB laminated glass subject to dynamic out-of-plane loading". In: *Engineering Fracture Mechanics* 112 (2013), pp. 26–40. DOI: 10.1016/j.engfracmech.2013.09.010.

[155] Salman Nisar, Lin Li, and MA Sheikh. "Laser glass cutting techniques—A review". In: *Journal of Laser Applications* 25.4 (2013), p. 042010. DOI: 10.2351/1.4807895.

[156] JF Kalthoff and S Winkler. "Failure mode transition at high rates of shear loading". In: *DGM Informationsgesellschaft mbH, Impact Loading and Dynamic Behavior of Materials* 1 (1988), pp. 185–195.

[157] Joerg F Kalthoff. "Modes of dynamic shear failure in solids". In: *International Journal of fracture* 101.1-2 (2000), pp. 1–31.

[158] Marreddy Ambati, Tymofiy Gerasimov, and Laura De Lorenzis. "A review on phase-field models of brittle fracture and a new fast hybrid formulation". In: *Computational Mechanics* 55.2 (2014), pp. 383–405. ISSN: 01787675. DOI: 10.1007/s00466-014-1109-y.

[159] Christian Miehe, Lisa Marie Schänzel, and Heike Ulmer. "Phase field modeling of fracture in multi-physics problems. Part I. Balance of crack surface and failure criteria for brittle

crack propagation in thermo-elastic solids". In: *Computer Methods in Applied Mechanics and Engineering* 294 (2015), pp. 449–485. ISSN: 00457825. DOI: 10.1016/j.cma.2014.11.016.

[160] Livermore Software Technology (LST), An ANSYS Company. *LS-DYNA R12*. URL: https://www.ansys.com/products/structures/ansys-ls-dyna.

[161] Jonas Rudshaug, Odd Sture Hopperstad, and Tore Børvik. "Effect of load level on cracking of L-shaped soda-lime glass specimens [Manuscript submitted for possible publication]". In: (2023).

[162] Ted Belytschko and Chen-Shyh Tsay. "A stabilization procedure for the quadrilateral plate element with one-point quadrature". In: *International Journal for Numerical Methods in Engineering* 19.3 (1983), pp. 405–419. ISSN: 1097-0207. DOI: 10.1002/nme.1620190308.

[163] Ted Belytschko, Jerry I. Lin, and Tsay Chen-Shyh. "Explicit algorithms for the nonlinear dynamics of shells". In: *Computer Methods in Applied Mechanics and Engineering* 42.2 (1984), pp. 225–251. ISSN: 0045-7825. DOI: 10.1016/0045-7825(84)90026-4.

[164] J. C. Simo and T. J. R. Hughes. "On the Variational Foundations of Assumed Strain Methods". In: *Journal of Applied Mechanics* 53.1 (1986), pp. 51–54. ISSN: 0021-8936. DOI: 10.1115/1.3171737.

[165] Satish Balay et al. *PETSc Web page*. https://petsc.org/. 2023. URL: https://petsc.org/.

A   Appendix: Experimental Results

A.1   Estimated fracture initiation locations and major principal stress at first failure

Table A.1 presents the estimated fracture initiation location and the estimated major principal stress at first failure for the coupe car, while the same data is compiled in Table A.2 for the sports utility vehicle (SUV) and Table A.3 for the SUV concept.

Table A.1: Estimated fracture initiation locations and major principal stress at first failure for the coupe car test series.

	Fracture initiation point				Major principal stress at first fracture			
	First fracture		Last fracture		Layer 1		Layer 2	
	X	Y	X	Y	Side 1	Side 2	Side 3	Side 4
Test	[mm]	[mm]	[mm]	[mm]	[MPa]	[MPa]	[MPa]	[MPa]
01	-13.9	426.4	12.1	499.4	-67.0	69.7	-37.2	68.9
02	-11.9	422.0	—	—	-66.9	74.5	-33.7	76.0
03	12.0	468.6	343.9	234.4	-75.2	77.4	-36.2	81.1
04	-10.2	344.6	-25.3	341.4	-21.4	71.3	35.2	105.0
05	-0.0	407.2	—	—	-53.7	84.5	-4.5	102.0
06	76.4	389.7	25.7	497.3	-32.5	65.1	14.6	98.7
07	19.4	345.4	1.8	472.4	-31.4	58.4	2.4	71.6
08	5.2	349.0	-2.7	394.7	-29.5	83.6	31.2	118.2
09	-6.5	352.8	-122.3	355.5	-45.3	111.3	21.1	150.7
10	-210.8	357.1	12.6	495.0	-63.7	51.9	-37.2	61.4

Table A.2: Estimated fracture initiation locations and major principal stress at first failure for the SUV test series.

	Fracture initiation point				Major principal stress at first fracture			
	First fracture		Last fracture		Layer 1		Layer 2	
	X	Y	X	Y	Side 1	Side 2	Side 3	Side 4
Test	[mm]	[mm]	[mm]	[mm]	[MPa]	[MPa]	[MPa]	[MPa]
01	51.7	666.6	218.3	196.4	-23.6	24.8	-11.5	38.8
02	2.6	582.4	-403.5	488.2	-44.7	58.2	-30.7	78.7
03	-27.9	583.0	-622.5	593.7	-47.5	81.4	-20.6	107.5
04	-49.6	546.4	607.7	518.4	-43.5	56.8	-20.3	80.9
05	-9.0	599.7	-555.8	596.3	-61.5	99.6	-30.9	114.9
06	18.0	521.1	-589.0	561.7	-73.6	125.1	-33.3	143.1
07	-19.5	587.4	-625.9	531.2	-52.9	84.7	-26.0	106.5
08	14.3	518.9	509.0	444.1	-74.8	131.8	-37.3	146.8
09	16.5	597.1	595.9	524.7	-79.9	157.7	-36.4	178.6
10	-1.9	592.1	547.2	523.7	-48.8	74.0	-26.4	103.4

A Appendix: Experimental Results

Table A.3: Estimated fracture initiation locations and major principal stress at first failure for the SUV concept test series.

| | Fracture initiation point | | | | Major principal stress at first fracture | | | |
| | First fracture | | Last fracture | | Layer 1 | | Layer 2 | |
Test	X [mm]	Y [mm]	X [mm]	Y [mm]	Side 1 [MPa]	Side 2 [MPa]	Side 3 [MPa]	Side 4 [MPa]
01	-450.6	355.0	30.4	979.7	68.8	-6.0	34.4	1.2
02	-33.5	650.6	-30.2	668.3	-69.8	110.2	-6.9	125.9
03	-57.3	639.5	—	—	-21.7	58.8	20.4	85.6
04	-537.1	779.6	—	—	83.2	-1.3	49.3	8.4
05	7.7	725.0	—	—	-27.2	38.0	19.7	68.7
06	-546.0	796.4	-22.5	87.3	79.6	1.0	47.3	11.4
07	-43.4	655.2	-420.5	897.6	-44.3	70.2	2.1	97.5
08	—	—	—	—	—	—	—	—
09	547.9	734.8	—	—	91.3	-4.7	55.4	5.4
10	76.8	169.8	—	—	67.4	-0.2	43.6	9.2
11	101.4	1059.7	—	—	90.1	-11.1	54.8	-0.7

NTNU
Norwegian University of
Science and Technology